Vrije Universiteit Brussel

Two-Dimensional Transformation Optics: A Guided Tour to Nonmagnetic Flatland Metamaterials

Proefschrift ingediend met het oog op het behalen van de graad van

Master in de Fysica en Sterrenkunde

Sophie Viaene

Promotor: Prof. Dr. Jan Danckaert

Copromotor: Prof. Dr. Philippe Tassin

Begeleider: Dr. Vincent Ginis

Faculteit Wetenschappen
Vakgroep Fysica en Sterrenkunde

Juni 2014

Two-Dimensional Transformation Optics:
A Guided Tour to Nonmagnetic
Flatland Metamaterials

Sophie Viaene
Vrije Universiteit Brussel, Faculteit Wetenschappen

Proefschrift ingediend met het oog op het behalen van de graad van
Master in de Fysica en Sterrenkunde

Promotor: Prof. Dr. Jan Danckaert
Copromotor: Prof. Dr. Philippe Tassin
Begeleider: Dr. Vincent Ginis
Jury leden: Prof. Dr. J. Danckaert, Dr. V. Ginis, Prof. Dr. A. Sevrin , Prof. Dr. P. Tassin
and Prof. Dr. I. Veretennicoff

Acknowledgments

To my **three** supervisors:
Prof. Danckaert, Jan, for welcoming me to a wonderful research group and providing excellent boundary conditions to perform my master thesis investigation,
Prof. Tassin, Philippe, for being a solid source of inspiration in times of doubt and 'en liten djävul' in times of success,
Dr. Ginis, Vincent, for guiding me towards the fascinating field of transformation optics and showing me the beauty of scientific figures,

Thank you!

To my **two** readers
Prof. Irina Veretennicoff, for initiating research in the exciting fields of metamaterials and transformation optics at the Vrije Universiteit Brussel,
Prof. Alexandre Sevrin, who has taught me my first courses in physics and showed me the beauty of differential geometry in my bachelor thesis,

Thank you!

Of course, there is **one** initial condition to my life without which this master dissertation might have looked quite different...
To my father, papa, thank you for being my proof reader, editor, printer and motivator,
To my mother, mama, thank you for all the little things only a mother can do,
To my brothers, Xander, Joachim and Michael, for learning me about relativity outside of physics,

To my family, thank you so much!

Sophie Viaene
Brussels, Belgium
June 6, 2014

Summary

In recent years, a novel class of artificial nanostructured materials, better known as *metamaterials*, has proven to be very efficient in molding the flow of light. Metamaterials consist of nanostructured arrays, whose electromagnetic response depends on the shape and composition of artificial meta-atoms, e.g., small resonant electric circuits. The design involves many degrees of freedom, which allows them to implement several revolutionary optical devices.

The enormous freedom in metamaterial properties requires efficient design tools. *Transformation optics* is such a framework, which relates geometrical specifications of optical devices to metamaterial properties. To this aim, transformation optics uses a coordinate transformation to deform the space surrounding a familiar optical device such that light is bent along a desired trajectory.

Recently, several research groups have been trying to apply transformation optics to confined electromagnetic waves on a thin material slab. The energy of these waves is localized within a thin material sheet and does not extend far in the direction normal to the material. In this way, confined waves are forced to propagate in two dimensions, within the plane of the slab.

However, the traditional transformation-optical framework does not allow for the manipulation of two-dimensional confined waves in a consistent way. Indeed, to transform confined waves propagating along a thin nonmagnetic material slab waveguide, it applies a global coordinate transformation, acting on both the slab material and the vacuum above and below. As a consequence, the equivalence relations impose that the transformation-optical device contains nontrivial materials, not only in the slab, but also in the vacuum regions. This is highly impractical and conflicts with the two-dimensional picture of a confined wave.

Therefore, this dissertation establishes *a new mathematical framework, guided transformation optics*, which only affects the slab material of the waveguide by a two-dimensional coordinate transformation. We achieve this by defining new equivalence relations.

Our guided transformation-optical framework takes into account that only the characteristics of guided mode propagation need to be fundamentally conserved by the equivalence relations. Therefore, we only modify the electric material parameter inside the slab in such a way that the Helmholtz equation is identical to the one of the coordinate-designed space.

In addition, we introduce an analytical equivalence relation on the thickness of the waveguide. Technically, this thickness variation maps the phase velocity of the desired guided waves in the coordinate-designed space to that of guided waves within our two-dimensional transformation-optical device. Because of this reason, it is not necessary to impose material to the vacuum regions above and below the material slab to manipulate guided mode propagation.

Samenvatting

Recente ontwikkelingen in de nanotechnologie hebben het afgelopen decennium aanleiding gegeven tot een nieuwe klasse van artificiële nanogestructureerde materialen: *metamaterialen*. Deze materialen bestaan uit een verzameling nanostructuren, bijvoorbeeld kleine resonante elektrische circuits, die meestal aangeduid worden als "meta-atomen". De eigenschappen van metamaterialen kunnen zeer gevarieerd zijn, omdat de elektromagnetische respons van meta-atomen afhangt van hun geometrie en samenstelling. Door deze flexibiliteit kan men metamaterialen inzetten om revolutionaire optische componenten te implementeren.

Door de grote vrijheid bij het ontwerp is er echter ook nood aan een efficiënte ontwerptechniek, bijvoorbeeld *de transformatieoptica*. Dit formalisme brengt specificaties over het gedrag van licht binnen een optische component in verband met eigenschappen van metamaterialen. Om dit te verwezenlijken vervormt de transformatieoptica de omgeving van een welbekende optische component, bijvoorbeeld een vlakke golfgeleider, met behulp van een coördinatentransformatie.

De afgelopen jaren hebben verschillende onderzoeksgroepen geprobeerd om de transformatieoptica toe te passen op een specifiek soort lichtgolven, nl. oppervlaktegolven. Deze golven worden gedragen door een dun laagje materiaal — de golfgeleider — en concentreren hun energie binnenin de golfgeleider. Buiten dit laagje materiaal neemt de energie van de oppervlaktegolf sterk af. Daarom zijn oppervlaktegolven in essentie tweedimensionaal.

Voorlopig is het formalisme van de transformatieoptica er echter niet in geslaagd om tweedimensionale gelokaliseerde golven op een consistente manier te manipuleren. Dit komt omdat het traditionele formalisme een globale coördinatentransformatie toepast op de niet-magnetische golfgeleider. De equivalentierelaties van de transformatieoptica eisen dan dat de materiaaleigenschappen allesbehalve triviaal zijn, niet alleen binnenin het materiaal maar ook in de oorspronkelijke vacuümgebieden. Het gebruik van metamaterialen buiten de oorspronkelijke golfgeleider is niet alleen onpraktisch, maar druist ook in tegen het tweedimensionale karakter van een oppervlaktegolf.

Om deze inconsistentie op te lossen ontwikkelt dit afstudeerwerk een *nieuw wiskundig formalisme, nl. geleide transformatieoptica*, die een tweedimensionale coördinatentransformatie gebruikt om niet-triviale materiaaleigenschappen op te leggen die enkel in het materiaallaagje van de geleider moeten geïmplementeerd worden.

Om dit te verwezenlijken formuleren we nieuwe equivalentierelaties. Deze werden zo opgesteld dat ze enkel inwerken op de cruciale karakteristieke eigenschappen van de geleide oppervlaktegolven. Zo is het mogelijk om de Helmholtzvergelijking van de golfgeleider precies te laten overeenstemmen met die van de ontworpen, getransformeerde ruimte, waarbij enkel gebruik gemaakt wordt van een zuiver elektrische respons in de golfgeleider.

Daarnaast is het cruciaal om een bijkomende analytische equivalentierelatie in te voeren die een verband legt tussen de dikte van de golfgeleider en de coördinatentransformatie. Hierdoor is de fasesnelheid van de oppervlaktegolf in de getransformeerde ruimte identiek aan de fasesnelheid van de oppervlaktegolven die zich binnenin ons geleide tweedimensionale ontwerp voortbewegen.

Door de dikte van het metamateriaallaagje te variëren, zoals beschreven door de regels van de geleide transformatieoptica, kunnen we oppervlaktegolven efficiënt manipuleren met niet-magnetische metamaterialen zonder de vacuümgebieden boven en onder de golfgeleider te moeten veranderen.

Contents

"I call our world Flatland,
not because we call it so, but to make its nature clearer to you,
my happy readers, who are privileged to live in Space."

— Edwin A. Abott, Flatland:
A Romance of Many Dimensions

Chapter 1

Introduction

1.1 Context

In the past decade, many photonic devices have become an essential part of our everyday life, including mode-locked lasers for high-precision spectroscopy, solar cells for renewable energy, and optical fibers for broadband telecommunication technology. However, these applications still suffer from a fundamental limitation due to the rather limited electromagnetic response of naturally occurring materials. For instance, at optical frequencies, natural materials only manipulate the *electric* component of light and are blind to its *magnetic* component. Furthermore, natural materials exhibit only a very small anisotropic response.

Advances in condensed matter physics, nanotechnology, and material science are now revolutionizing our ability to control electromagnetic waves through the development of metamaterials. Metamaterials use nanostructured arrays of artificial meta-atoms—e.g., small resonant electric circuits with electric and magnetic response depending on specific geometrical and material parameters—to manipulate light to an unprecedented degree.

Since the response of each meta-atom may be tuned individually, metamaterials have position-dependent and directionally-dependent material parameters, which are able to mold the flow of light in unconventional ways. Their design involves many degrees of freedom, including large anisotropy, chirality, and nonlinearity, which allow for the implementation of several novel optical devices such as invisibility cloaks, subwavelength imaging systems, and optical isolators.

1.2 Motivation

To be able to exploit these many degrees of freedom of metamaterials in an efficient way, transformation optics provides a mathematical framework to determine how the electromagnetic material properties of metamaterials should be modified in an optical device in order to achieve novel functionalities. The framework identifies the material parameters based on a coordinate transformation of the background space. To this aim, transformation optics establishes equivalence relations between metric tensors and electromagnetic material tensors. These equivalence relations lie at the heart of the transformation-optical framework. The technique was first applied to the design of an invisibility cloak, where the coordinate transformation stretches straight light trajectories in free space into a desired trajectory such that they bend around the object to be hidden.

In recent years, there is a growing need to manipulate electromagnetic waves that are confined to a two-dimensional interface. Indeed, such material interfaces are becoming increasingly important in several photonic applications like biosensing, subwavelength imaging and spectroscopy. In addition, the potential of miniaturized high-speed computer chips provides a compelling motivation for developing flatland metamaterials capable of manipulating two-dimensional waves.

Nowadays, computer chips are mostly implemented using electronic devices. The performance of these systems is fundamentally limited by the bandwidth of metallic wires connecting various electronic components on the chip. Because light is a fast and broadband carrier of information, integration of electronic and photonic devices on a single chip may resolve current speed limits and performance in integrated systems. However, integrated photonic devices should be compatible with miniaturization of electronic components. Therefore, electromagnetic waves in integrated photonic devices should be highly confined to two-dimensional surfaces.

These are the arguments that motivate the research for an extension of the scope of transformation optics towards the manipulation of electromagnetic guided waves.

1.3 Guided Transformation Optics: a Novel Paradigm to Manipulate Two-Dimensional Surface Waves

In this dissertation, we investigate how coordinate transformations affect two-dimensional waves confined to a nonmagnetic material slab waveguide in a consistent way. In fact, the traditional framework of transformation optics acts on the slab waveguide in a global way, as it transforms both the guiding material and the vacuum above and below. In this way, the equivalence relations impose nontrivial electromagnetic parameters, both

in and out of the slab. Obviously, this is not compatible with practical realizations of two-dimensional transformation-optical waveguides.

Therefore, we propose a novel mathematical framework—*guided transformation optics*—in which only the slab material of the waveguide is affected by a two-dimensional coordinate transformation. Contrary to traditional transformation optics, our framework is capable of molding guided wave propagation *without magnetic response and without the need for changing the vacuum regions surrounding the waveguide.* This greatly simplifies the metamaterial design and reduces losses that are intrinsically present in magnetic metamaterials. To this aim, guided transformation optics introduces the thickness of the waveguide as a crucial parameter in the equivalence relations.

In this way, this dissertation establishes new equivalence relations relating the electric material parameter and the thickness of the slab to a two-dimensional coordinate transformation. Subsequently, we apply these analytical equivalence relations to the design of a nonmagnetic beam bender of 30 and 45 degrees, which may contribute to efficient guiding of confined waves in on-chip applications.

Chapter 2

The Geometry of Light

METAMATERIALS provide many degrees of freedom to manipulate the flow of light. As a consequence, efficient metamaterial optical devices require dedicated designing tools, e.g., transformation optics, that relate their functionality to specific metamaterial parameters. The mathematical framework of transformation optics relies on techniques which are also fundamental to the theory of general relativity. As a first objective, this chapter explains how three-dimensional transformation-optical media appear to electromagnetic waves as if they are a deformed geometry. Such geometries are generated by coordinate transformations, e.g., quasi-conformal coordinate transformations which are particularly useful for realistic metamaterial designs. As a second objective, we focus on several attempts in literature to develop a two-dimensional transformation-optical framework which molds the flow of surface waves on a metal-dielectric interface, e.g., surface plasmon polaritons. Also, graphene provides interesting opportunities as a one-atom thick platform to two-dimensional transformation optics.

2.1 Introduction

2.1.1 A Geometrical View on Wave Propagation

Throughout history, geometrical arguments have contributed to our fundamental understanding of light propagation in macroscopic media. Until recently, these arguments relied on the ray approximation [1], which is valid if the parameters of the electromagnetic medium change slowly with respect to the wavelength. In this approximation, the propagation of light can be effectively described by the behavior of light rays—narrow pencils of light aligned with the propagation direction.

The principle of Fermat is the corner stone of these geometrical arguments. It states that the physical trajectory of a light ray, going from a point A to a point B, extremizes the

optical path length *OPL*

$$OPL = \int_A^B n(\mathbf{r})\, dl, \tag{2.1}$$

determined by the refractive index $n(\mathbf{r})$ of an inhomogeneous medium.

When looking at these observations from a geometrical point of view, a fundamentally new interpretation arises which is closely related to how distances are measured in a curved space, i.e. a Riemannian geometry.* Loosely speaking, a Riemannian geometry can be described by an intrinsic measure of lengths, a metric g_{ij}, which determines the distance between two vectors dx^i and dx^j [2]

$$ds^2 = g_{ij}\, \mathrm{d}x^i \mathrm{d}x^j. \tag{2.2}$$

Since the principle of Fermat (2.1) also establishes an optical path length between the source A and the receiver B

$$ds^2 = n^2 \delta_{ij}\, \mathrm{d}x^i \mathrm{d}x^j,$$

the medium $n(\mathbf{r})$ acts on light in the same way as a geometry $g_{ij} = n^2\delta_{ij}$. Then, light extremizes the distance traveled with respect to this new measure of length which clearly differs from the Euclidean length observed by the experimenter. In particular, it is well known that light trajectories through inhomogeneous media bend towards regions with high refractive index.

This geometrical observation underpins the conceptual turnaround established by transformation optics [3] [4]. According to the extended version of Fermat's principle (2.2), there exist a special kind of media—transformation media—whose involved material parameters impose an effective optical length to light using an optical analogue of a Riemannian geometry g_{ij}. They use their inherent geometry g_{ij} to select physical trajectories $x^i(\lambda)$, geodesics parameterized by a scalar λ, which extremize the electromagnetic length s

$$s = \int_A^B d\lambda \sqrt{g_{ij}\, \frac{dx^i}{d\lambda} \frac{dx^j}{d\lambda}}. \tag{2.3}$$

This electromagnetic length is defined for any metric g_{ij} and therefore generalizes the optical path length introduced by the principle of Fermat. It defines geodesic trajectories of light in an identical way as the trajectories of test particles within a gravitational field in general relativity.

2.1.2 Intuitive Transformation Optics: How to Design an Invisibility Cloak

Before we develop the framework of transformation optics in a mathematical way, we provide an intuitive explanation of how transformation optics allows for the design of

*As explained in Appendix A, we continue with a differential-geometric notation which simplifies notations thanks to the Einstein summation convention. Readers who are unfamiliar with differential-geometrical techniques might have a look at Appendix B.

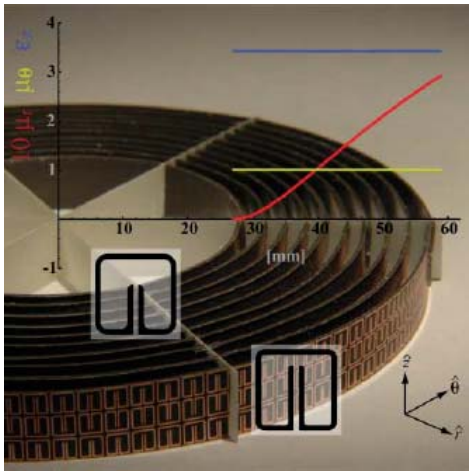

Figure 2.1: The first experimental realization of an invisibility cloak implemented by split-ring resonators with anisotropic permeabilities μ_r, μ_θ and permittivity ϵ_z. Figure reproduced with permission from Ref. [10].

devices with unexpected behavior, such as sharp, lossless beam bends [5], beam splitters [6], sub-diffraction-limited lensing systems [7] [8], and last but not least, revolutionary invisibility cloaks [3]-[9].

To illustrate the methodology of transformation optics, we consider how a cylindrical cloak hides an object, e.g., a copper cylinder, inside a cylindrical region surrounded by a transformation-optical medium. This medium bends light in such a way that it never reaches the central object (Fig. 2.1). Additionally, perfect invisibility is only achieved if all kinds of reflections and scattering during bending, which would reveal the cloaking device, are avoided.

As mentioned in the previous subsection, transformation-optical media use metamaterials to impose a Riemannian geometry which manipulates electromagnetic waves in a desired way. We call this geometry the 'physical space' associated to the optical device and provide it with coordinates x^μ.*

The framework of transformation optics consists of a *two-step procedure*. First, it uses differential-geometrical techniques to design an appropriate Riemannian geometry g_{ij} of physical space conform to the specifications of the invisibility cloak. Second, the framework provides equivalence relations, which relate the material parameters of the device, i.e. anisotropic and inhomogeneous permittivities ϵ^{ij} and permeabilities μ^{ij}, to the geometry of physical space. These parameters identify the Maxwell equations which describe propagation of light in physical space to the Maxwell equations of the device. Such a transformation-optical device imposes identical light propagation as physical space.

*Appendix A.2 discusses two approaches for defining auxiliary spaces in the transformation-optical framework. This dissertation makes uses of the convention by Ref. [4].

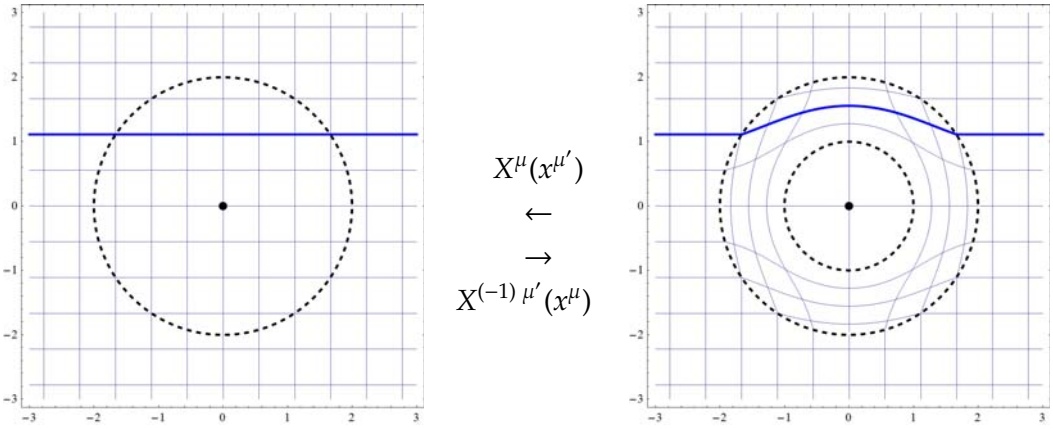

Figure 2.2: Determination of light propagation in physical space with coordinates x^{μ} (right) using a coordinate transformation $X^{\mu'}$ of a cylindrical invisibility cloak (Eq. 2.4 obtained from Ref. [10]) acting on an auxiliary electromagnetic space with coordinates $x^{\mu'}$ (left).

To design Riemannian geometry in physical space, we make use of another auxiliary 'electromagnetic space' with coordinates $x^{\mu'}$ (Fig. 2.2). The electromagnetic space determines the coordinates x^{μ} of physical space using an invertible, differentiable coordinate transformation X^{μ}

$$x^{\mu} = X^{\mu}\left(x^{\mu'}\right),$$
$$x^{\mu'} = X^{(-1)\,\mu'}\left(x^{\mu}\right),$$

with a Jacobian matrix $\Lambda^{\mu}_{\mu'} = \frac{\partial x^{\mu}}{\partial x^{\mu'}}$ and nonzero determinant Λ with $\mu, \mu' \in \{0, \ldots 3\}$. Fig. 2.2 illustrates how such a coordinate transformation indeed affects the geometry of physical space as it maps lines of constant coordinates in electromagnetic space to a specific configuration in physical space. Light rays which follow the coordinate lines are bent around the object hidden at the center.

This approach to finding a suitable physical space geometry fundamentally relies on the principle of covariance [2]. This principle implies all physical theories—including those of electromagnetism—do not fundamentally rely on the coordinates used to describe them. According to this coordinate-independent, covariant formulation of electromagnetism, *the electromagnetic and physical space are equivalent representations of the very same space-time*. Therefore, the fundamental characteristics of wave propagation in electromagnetic space are identical to those of physical space as these are transferred by the coordinate transformation. For example, if waves propagate through electromagnetic space without reflections or perturbations, this is also the case in physical space irrespective of the detailed form of the coordinate transformation.

The equivalence relations guarantee these fundamental properties of light propagation are transfered to the transformation-optical device. In this way, the basic geometry and material parameters within electromagnetic space directly affect the functionality

of the device. The geometrical and material properties of electromagnetic space must be chosen with great care.

In the case of an invisibility cloak, the waves need to be insensitive to changes in material parameters—necessary to bend the light— and should behave as if they never encountered any obstruction. The device should appear as an empty vacuum which does not scatter light in any way. This is why the first invisibility cloak [10] uses a flat and empty electromagnetic space to impose reflectionless propagation within an invisibility device.

A coordinate transformation $X^{\mu'}$ acts on the electromagnetic space in such a way that the wave propagation in physical space x^{μ} exactly corresponds to the desired functionality of the device. Fig. 2.2 shows how the invisibility device stretches the cylindrical coordinates (r', θ', z) at the origin such that the singularity at $r' = 0$ is mapped into the inner radius R_1—forming the inner region of the device—and such that the outer radius R_2 of the device is matched to the surrounding flat geometry of vacuum in a continuous way, [10]

$$\begin{cases} r' &= R_2 \, \frac{r-R_1}{R_2-R_1}, \\ \theta' &= \theta, \\ z' &= z. \end{cases} \tag{2.4}$$

In doing so, the light trajectories (geodesics) of electromagnetic space are transformed into light trajectories (geodesics) of physical space. Light is guided around and never enters the central region.

In summary, the electromagnetic space guarantees the fundamental reflectionless propagation within the invisibility device while the coordinate transformation determines light propagation. The coordinate transformation directly determines the geometry of physical space in such a way that the geodesics, the trajectories followed by light, correspond to the desired wave propagation inside the device. Appendix B proves that this is another consequence of the covariant formulation of electromagnetism on curved space-times.

Although the invisibility cloak convinced the electromagnetic community of the importance of transformation optics, both in designing innovative optical devices and increasing understanding of fundamental laws in electromagnetism [11], it does not completely express the impressive flexibility transformation optics offers.

Nontrivial electromagnetic spaces provide many degrees of freedom, as they might posses non-Euclidean geometries and nontrivial material parameters. On a conceptual level, non-Euclidean electromagnetic spaces provide optical analogues to many general relativistic geometries, such as compactified De Sitter spaces [12]. From a design perspective, non-Euclidean electromagnetic spaces might be chosen in a clever way to improve Euclidean transformation-optical material parameters. In this way, non-Euclidean transformation optics has led to broadband implementations of invisibility devices [13] and thin directional lenses [14].

Nontrivial materials and material interfaces extend the scope of transformation optics in another important way. Traditional empty electromagnetic spaces sustain three-dimensional unconstrained electromagnetic waves, which are usually expanded with respect to plane waves. Therefore, transformation-optical devices based on empty electromagnetic spaces do not introduce reflections because the medium appears to them as if it is a vacuum. It simply bends them [5], steers them [6] or guides them around obstructions [3] after which they emerge unaffected.

On the other hand, if electromagnetic spaces contain inhomogeneous media [9] or a planar mirror [15], light waves in the transformation-optical medium are fundamentally modified. Because they experience the materials of electromagnetic space, they will respectively refract in exactly the right way to avoid a central object—this has led to an optimized conformal invisibility cloak—or reflect from a distorted metallic surface in physical space as if they meet the planar mirror in electromagnetic space before distortion [15].

Additionally, it is also possible to introduce material interfaces to electromagnetic space. These sustain a zoo of confined, two-dimensional electromagnetic waves, e.g., plasmonic surface waves on metal-dielectric interfaces [16], guided modes in dielectric waveguides [17], Dyakonov waves at the interface of media with different anisotropy [18], etc.

Recent research focusses on how plasmonic surface waves sustained by metal-dielectric interfaces [19] are manipulated by transformation-optical media. In this chapter, we review the contributions of transformation optics to the manipulation of these surface waves. However, we believe that substantial progress in the development of transformation optics is to be made at the level of dielectric waveguides and light propagation through optic fibers [20].

2.2 Three-Dimensional Transformation Optics

This section explains in a mathematical way how transformation optics allows for the design of unconstrained three-dimensional electromagnetic media.

2.2.1 Electromagnetism on Curved Spaces

In the introduction, we motivated how an electromagnetic space with coordinates $x^{\mu'}$ uses a coordinate transformation with Jacobian $\Lambda^{\mu}_{\mu'} = \frac{\partial x^{\mu}}{\partial x^{\mu'}}$ and nonzero determinant $\Lambda = \det\Lambda^{\mu}_{\mu'}$ to impose the geometry, geodesics and fundamental behavior of light to a physical space with coordinates x^{μ}. However, we still need to relate the geometry of physical space to the metamaterial parameters of the transformation-optical device.

Because the transformation-optical medium should establish the very same electric fields **E**, magnetic fields **H** and power flow as in the designed physical space, the Maxwell equations corresponding to this medium

$$\partial_i \left(\epsilon^{ij} E_j\right) = 0, \tag{2.5}$$
$$\partial_i \left(\mu^{ij} H_j\right) = 0, \tag{2.6}$$
$$[ijk]\, \partial_j E_k = -\mu_0\, \partial_t \left(\mu^{ir} H_r\right), \tag{2.7}$$
$$[ijk]\, \partial_j H_k = \epsilon_0\, \partial_t \left(\epsilon^{ir} E_r\right). \tag{2.8}$$

should be identical to those of physical space derived in appendix B

$$\partial_i \left(\sqrt{g}\, \tilde{\epsilon} g^{ij} E_j\right) = 0, \tag{2.9}$$
$$\partial_i \left(\sqrt{g}\, g^{ij} H^j\right) = 0, \tag{2.10}$$
$$[ijk]\, \partial_j E_k = -\mu_0\, \partial_t \left(\sqrt{g}\, g^{ir} H_r\right), \tag{2.11}$$
$$[ijk]\, \partial_j H_k = \epsilon_0\, \partial_t \left(\sqrt{g}\, \tilde{\epsilon} g^{ir} E_r\right), \tag{2.12}$$

We limit the discussion to purely spatial metrics and coordinate transformations such that all Greek space-time indices μ are replaced by Roman indices m. Also, we assume that the electromagnetic space contains an isotropic homogeneous dielectric with relative permittivity $\tilde{\epsilon}$ as this allows extending our results to electromagnetic spaces containing a dielectric slab waveguide (Chapter 4).

To achieve this mapping, we compare the Maxwell equations of physical space to those of an electromagnetic medium with anisotropic and inhomogeneous relative permittivities ϵ^{ij} and permeabilities μ^{ij}. The Maxwell equations which describe the device indeed agree with those which describe physical space if its material parameters are related to the metric of physical space g_{ij} with determinant g

$$\epsilon^{ij} = \sqrt{g}\, \tilde{\epsilon}\, g^{ij}, \tag{2.13}$$
$$\mu^{ij} = \sqrt{g}\, g^{ij}. \tag{2.14}$$

Although we used the principle of Fermat (2.1) to motivate the geometrical ideas behind transformation optics, the scope of transformation optics does extend beyond the ray approximation (subsection A.3.3). The equivalence relations are imposed at the level of the full macroscopic Maxwell equations and retain their validity even in the subwavelength regime [21]. Therefore, plasmonic systems, graphene sheets and thin waveguides are also amendable to the ideas discussed above.

Once these equivalence relations (2.13) and (2.14) are implemented by metamaterials, *the transformation-optical medium truly behaves as if it is a Riemannian geometry*. We now understand in a physical way how an invisibility cloak modifies wave propagation without inducing reflections. In the presence of inhomogeneous materials, solutions to

the Maxwell equations are both determined by a refractive index, which takes propagation into account, and an impedance, which determines how waves reflect and refract as a consequence of boundary conditions imposed by material interfaces as is clear from the laws of Fresnel. In particular, the impedance measures the difference in electric and magnetic responses of a material. Because the equivalence relations imply the invisibility cloak has equal electric and magnetic responses, i.e., the medium is impedance-matched, reflections are completely suppressed.

The equivalence relations lead to another important observation. In principle, any coordinate transformation on a flat electromagnetic space induces nontrivial metrics (B.12)

$$g_{ij} = \Lambda_i^{i'} \Lambda_j^{j'} \delta_{i'j'},$$

and as a result transformation-optical devices are *inherently magnetic* (2.14). Unfortunately, traditional resonant metamaterials (subsection 2.4.1) suffer from substantial losses if they need to reach high relative permeabilities associated to strong resonances.

At the level of transformation optics, literature provides two approaches to avoid magnetic materials in order to mitigate these losses. First, the required response strongly depends on the initial polarization of the wave. Because the macroscopic Maxwell equations use a permeability μ^{ij} to couple the magnetic field strength $\mathbf{H}$ to the magnetic field $\mathbf{B}$

$$B^i = \mu_0 \mu^{ij} H_j,$$

one might choose the polarization of the magnetic field parallel to one of the principal axes, e.g.,

$$\mathbf{H} = H_y \mathbf{e}_y.$$

In this way, only one element of the permeability tensor truly matters [10].

Second, there exists a particular set of coordinate transformations—(quasi)-conformal transformations—which rely on techniques from complex analysis to reduce the anisotropy of material parameters. These techniques are discussed in the following subsection.

2.2.2 (Quasi)-Conformal Transformations

A conformal map X^i of electromagnetic to physical space has the desired property that the physical metric g_{ij} is proportional to the metric of electromagnetic space $g_{i'j'}$, with some spatially dependent factor $n(x^i)$

$$g_{ij} = \left[n(x^i)\right]^2 g_{i'j'}.$$

Therefore, if the electromagnetic space is flat $g_{i'j'} = \delta_{i'j'}$, the resulting material parameters (2.13) and (2.14) are isotropic

$$\epsilon = n(x^i)\, \tilde{\epsilon},$$
$$\mu = n(x^i),$$

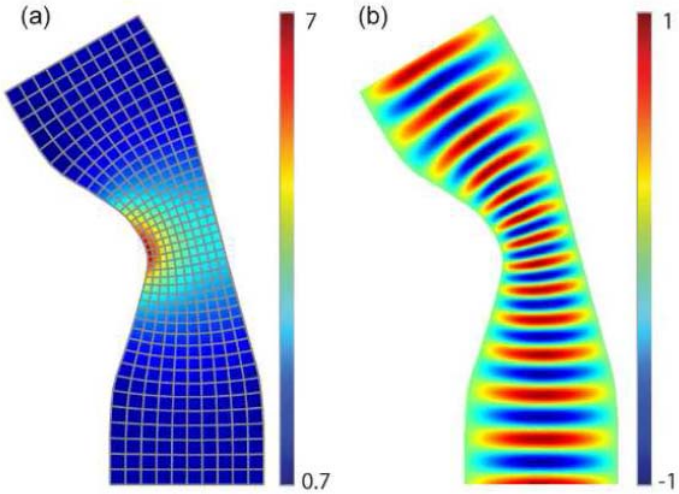

Figure 2.3: Permittivity map (left) and transmitted electric field (right) of a 'squeezed' bend. Figure reproduced with permission from Ref. [22].

and a nonmagnetic implementation of transformation-optics is readily available, i.e. $\epsilon_{eff} = n(x^i)^2$ and $\mu_{eff} = 1$.

Mathematically, however, the Liouville theorem restricts such maps to simple Möbius transformations—constant rescalings, rotations and translations—as soon as three- or higher-dimensional spaces are considered. Instead, one might use optimizations of three-dimensional coordinate transformations, quasi-conformal maps, which only approximately achieve isotropic material parameters because they minimize the anisotropy of the transformation [22].

Quasi-conformal maps have been widely applied to several disciplines in computation, aerodynamics, hydrodynamics and even electromagnetism [23], long before the advent of transformation optics. Therefore, numerical optimization techniques are readily available and provide an efficient tool to determine dielectric transformation media. Since (quasi)-conformal maps are particularly adapted to map any initial rectangular space, e.g., electromagnetic space, to a simply connected domain of arbitrary shape, e.g., physical space, dielectric materials may squeeze light through arbitrarily shaped waveguides or bend light in an arbitrary way (Fig. 2.3). Quasi-conformal techniques were also applied in designing a planar invisibility cloak at optical frequencies [24].

Although quasi-conformal maps are numerically very effective, it does not provide an analytical method to reduce anisotropy. Luckily, coordinate transformations related to two-dimensional devices—such as beam benders, beam shifters and cylindrical invisibility cloaks—always preserve one orthogonal direction of electromagnetic space,

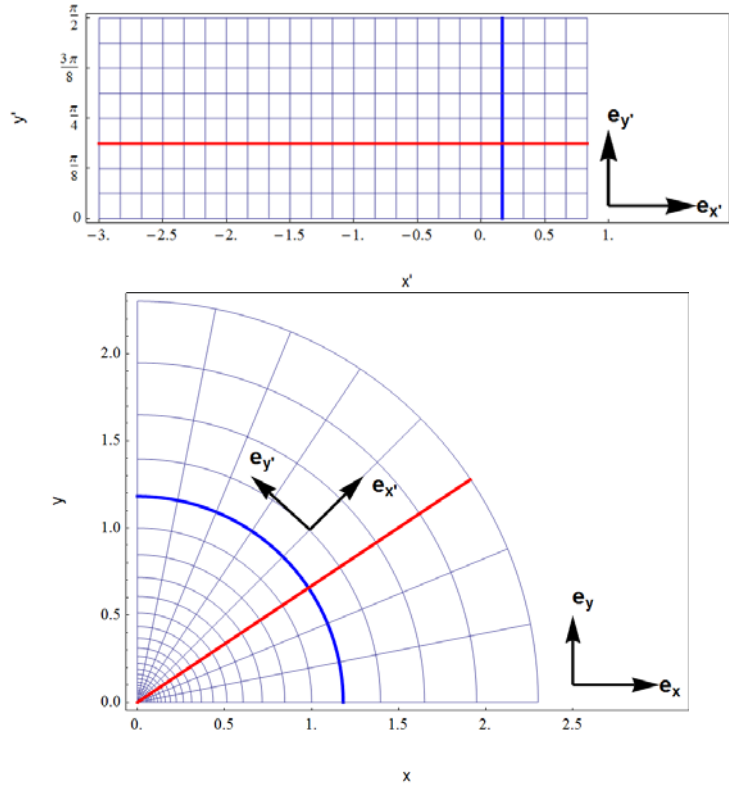

Figure 2.4: An illustration of a finite-embedded transformation by a conformal exponential map e^z. The map preserves right angles between coordinate lines which correspond to fixed y' (red) and x' (blue) coordinates in electromagnetic space (upper figure). Light which propagates along the blue trajectory in electromagnetic space is bent by the transformation in physical space (lower figure). Light which enters from below is not reflected if the geometry along the boundary is equal to that of the vacuum, i.e. Euclidean flat space.

which we call z

$$\begin{cases} x' &= X(x,y), \\ y' &= Y(x,y), \\ z' &= \sqrt{g_{zz}}\, z. \end{cases} \tag{2.15}$$

Such two-dimensional transformations have been used to manipulate surface wave propagation at plasmonic interfaces (section 2.3) and guided waves along waveguides (chapter 4). Because the orthogonal direction z is separated from the in-plane directions xy, the metric transformation rule (B.12) implies that geometries of two-dimensional transformation optics generally contain an induced metric γ_{ij} and a component g_{zz} orthogonal to it

$$g_{ij} = \begin{pmatrix} \gamma_{ij} & 0 \\ 0 & g_{zz} \end{pmatrix}. \tag{2.16}$$

Since Liouville's theorem does not prohibit the existence of perfectly conformal transformations $(X(x,y), Y(x,y))$ in two dimensions, Eq. (2.15) may be optimized to achieve perfectly isotropic material parameters in the plane of the waveguide. These conformal maps are elegantly represented by analytic functions

$$f(x+iy) = X(x,y) + iY(x,y).$$

Analyticity of conformal maps has two profound implications. First, a differentiable complex function is subject to Cauchy-Rieman conditions, which relate components of the Jacobian in the following way

$$\begin{aligned} \partial_x X(x,y) &= \partial_y Y(x,y), \\ \partial_y X(x,y) &= -\partial_x Y(x,y), \end{aligned} \tag{2.17}$$

and guarantee the two-dimensional metric γ_{ij} is isotropic

$$\begin{aligned} \gamma_{ij} &= \left[(\partial_x X)^2 + (\partial_x Y)^2\right], \\ &= \gamma(x,y)\ \delta_{ij}. \end{aligned} \tag{2.18}$$

As a consequence, material parameters associated a conformal transformation-optical medium are uniaxial (Eq. ((2.13) and Eq. (2.14))

$$\epsilon^{ij} = \begin{pmatrix} \tilde{\epsilon} & 0 & 0 \\ 0 & \tilde{\epsilon} & 0 \\ 0 & 0 & \gamma(x,y)\tilde{\epsilon} \end{pmatrix}, \tag{2.19}$$

$$\mu^{ij} = \begin{pmatrix} 1 & 0 & 0 \\ 0 & 1 & 0 \\ 0 & 0 & \gamma(x,y)\tilde{\epsilon} \end{pmatrix}. \tag{2.20}$$

Fig. 2.4 illustrates how a conformal exponential map $f(z) = e^z$,

$$\begin{cases} x &= \cos(y')\ e^{x'}, \\ y &= \sin(y')\ e^{x'}, \end{cases} \tag{2.21}$$

preserves angles—in particular orthogonal angles—between coordinate lines before and after transformation.

A second implication of analyticity is connected to the concept of finite-embedded coordinate transformations [6]. As shown in Fig. 2.4, a finite-embedded transformation is a local transformation which acts on a finite area in electromagnetic space. Then, physical space also contains a finite region with nontrivial transformation-optical parameters which is embedded into vacuum, the medium of the untransformed electromagnetic space. Fig. 2.4 shows how geodesics of a finite region in electromagnetic space appear to be bent in physical space due to a conformal coordinate transformation.

To ensure waves couple in and out of a transformation-optical device without being reflected, the metric components of physical space g_{ij} parallel to the interface—i.e. the

induced metric of g_{ij} on the surface separating the device from vacuum—should be identical to those of the surrounding medium δ_{ij}. In this way, the transversal electromagnetic fields do not notice any change in geometry until they are already inside the impedance-matched medium. Traditionally, this continuity of the metric is achieved if the coordinate transformation within the device reduces continuously to the identity transformation outside of the device. However, the analyticity of a conformal transformation prevents a continuous transition. Analytical continuation would imply the transformation is equal to the identity transformation both within and outside of the device. Therefore, analytic conformal transformations inherently suffer from insertion and extraction loss when applied to a finite region.

As explained in chapter 4, two-dimensional conformal transformations are compatible with two-dimensional surface waves, e.g., sustained by metal-dielectric interfaces. These plasmonic surface waves are discussed in the following section.

2.3 Plasmonic Transformation Optics

2.3.1 Introduction

The main motivation for applying transformation optics to two-dimensional systems, is provided by intense research efforts to produce integrated optical circuits [16], fully compatible with electronic Very Large Scale Integrated (VLSI) systems. Currently, computational speed is limited by metallic interconnects in VLSI. As a fast and broadband carrier for digital information, two-dimensional confined waves would greatly increase computational speed of such circuits. Because electronic circuits already make use of metals, investigations mainly focus on metal-dielectric optical circuits, i.e. plasmonics which sustain confined waves thanks to collective motions of free electrons within the metal (Fig. 2.5). These waves are also known as surface plasmons polaritons (SPP) and play a crucial role in optical sensing systems, spectroscopy, subdiffractional imaging and enhancement of fluorescence and Raman scattering [19].

On the conceptual level, two-dimensional systems are also interesting for investigating optical analogues of fundamentally curved Riemannian geometries such as two-spheres [25]. These investigations provide new ways for manipulating and preserving the shape of wave packets sustained by dielectric waveguides which may be applied to optical fiber telecommunication.

This section describes how several decisive applications of three-dimensional transformation optics, using two-dimensional coordinate transformations Eq.(2.15), are extended to plasmonic systems which sustain surface waves. We consider the metal-dielectric interface of Fig. 2.5 with permittivities ϵ_M of the metallic layer and ϵ_D of the dielectric layer having opposite signs.

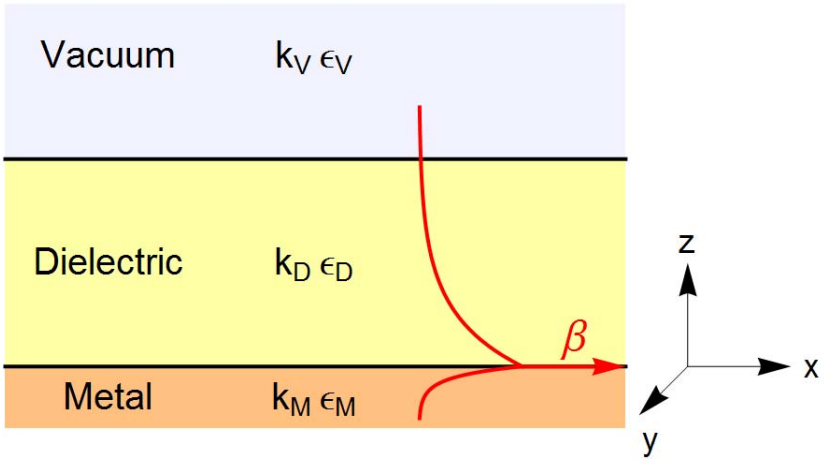

Figure 2.5: Illustration of a realistic metal-dielectric interface with metallic layer $\epsilon_M \in \mathbb{C}$, dielectric layer ϵ_D and vacuum layer ϵ_V. The dielectric layer is sufficiently thick such that the surface wave profile (red) extinguishes over several decay lengths $\frac{1}{2Im(k_D)}$ before reaching the vacuum.

Because the skin depth $\frac{1}{2Im(k_M)}$ of the metal layer is only several nanometers long, e.g., 23 nm for gold at wavelengths of $1.5\mu m$, current manufacturing techniques do not allow implementing transformation-optical media in the metallic layer. To our opinion, literature provides two different approaches to SPP manipulation with transformation optics. The most conservative extension of three-dimensional transformation optics to plasmonics simply uses the three-dimensional transformation-optical material parameters inside the dielectric and does not change the metallic layer [26] [27]. Another approach uses quasi-conformal transformations and thickness variations of the homogeneous dielectric layer to manipulate SPP's [27]. The latter approach is, however, only valid in the ray approximation.

2.3.2 Surface Plasmon Polaritons

Before considering the aforementioned implementations, we briefly consider how SPP surface waves propagate along a metal-dielectric layer normal to the z-direction. We choose our x-direction such that it coincides with the propagation direction as in Fig. 2.5. These surface waves are only consistent with boundary conditions of the Maxwell equations if they have the following electric fields [16]

$$\mathbf{E}_D = \mathbf{E}_{D0}\, e^{i\beta x} e^{-ik_D z}, \tag{2.22}$$

$$\mathbf{E}_M = \mathbf{E}_{M0}\, e^{i\beta x} e^{ik_M z}, \tag{2.23}$$

and propagation constant β

$$\beta = \frac{\omega}{c}\sqrt{\frac{\epsilon_M \epsilon_D}{\epsilon_M + \epsilon_D}}, \tag{2.24}$$

depending on the frequency ω and material parameters in the metal ϵ_M and the dielectric ϵ_D. Because the permittivity of the metal is complex, the SPP decays at propagation length scales $\frac{1}{2Im(\beta)}$. This restricts SPP propagation lengths of 1mm and provides an upper bound to the physical extent of optical devices. The orthogonal wave vectors

$$k_{M/D}^2 = \epsilon_{M/D}\frac{\omega^2}{c^2} - \beta^2, \tag{2.25}$$

increase with frequency. Therefore, high frequencies and small wavelengths result in strong confinement, while low frequencies and large wavelengths result in weak confinement.

2.3.3 Dielectric Permittivity Variations

A first attempt [26] to manipulate surface waves on a metal-dielectric interface with transformation optics simply limits the implementation of the desired material parameters (Eq. (2.13) - Eq. (2.14)) to the dielectric layer.

Fig. 2.6 shows the efficiency of such a limited implementation is wavelength-dependent. At a wavelength of $\lambda = 1.5\mu m$ the device performs particularly well because the decay length of the surface wave within the dielectric layer is larger than the skin depth of the metal (Eq. (2.25)). The electromagnetic energy mostly resides within the dielectric layer and the lack of a transformation-optical medium in the metal barely affects performance. In contrast, shorter wavelengths and higher frequencies increase the confinement. Therefore, the contribution of the skin depth of the metal becomes increasingly important when compared to the decay length within the dielectric. The performance of the device decreases as wavelengths become shorter.

Additionally, the metallic layer is intrinsically incompatible with the requirements of a cylindrical invisibility cloak as reflections should be avoided at all costs. Thus, the performance also depends on the nature of the transformation-optical device. For example, the planar invisibility cloak—which hides bumps in metal surface with a flat mirror in electromagnetic space—is completely compatible with the presence of a metallic-dielectric layer. The planar cloak does not show a degradation in performance with decreasing wavelength.

Ref. [27] considers a plasmonic 90-degree beam bend [27] and compares two coordinate transformations, a straightforward anisotropic transformation and a quasi-conformal transformation. As for the beam bend considered before (2.4), the anisotropic transformation from electromagnetic space $x^{i'} = \{x', y', z'\}$ to physical space with cylindrical coordinates $x^i = \left\{r, \phi, z\right\}$

$$\begin{cases} r &= & y', \\ \phi &= & \frac{\pi}{2}(1 - \frac{x'}{b}), \\ z &= & z', \end{cases} \tag{2.26}$$

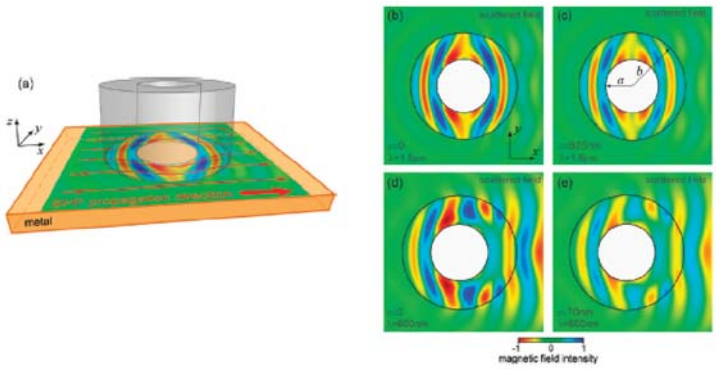

Figure 2.6: Plasmonic cylindrical invisibility cloak (a) with transformation-optical medium in the dielectric layer. Performance increases for $\lambda = 1.5\mu m$ (b) at the metal-dielectric interface and (c) at the surface of the dielectric layer, with respect to the performance at $\lambda = 600nm$ d) at the metal-dielectric interface and (e) at the surface of the dielectric layer. Figure reproduced with permission from Ref. [26].

is a finite-embedded transformation. As shown by the inset of (Fig. 2.7), a rectangular area $[0, b] \times [a, b]$ in electromagnetic space is transformed to a circular arc of outer radius b. Note the transformation is also two-dimensional in the sense of Eq. (2.15).

Before we move on to another attempt in literature to manipulate surface waves with thickness variations, we illustrate the power of transformation optics as a problem solving tool. We reconsider the simple example of a beam bender.

Fig. 2.4 and Fig. 2.7 show how plane waves propagating in the x'-direction in electromagnetic space, i.e. x' increases with time and y' is a constant, are transformed by the bender to trajectories in physical space which turn about the z-direction at a constant radius r. Generally, it is very difficult to find an analytic solution to wave propagation in a bi-anisotropic electromagnetic medium with ϵ^{ij} and μ^{ij}. Thanks to the coordinate transformation (2.26) and the transformation rules of a covector (B.7), this is most easily achieved within the framework of transformation optics.

First, we solve the problem in electromagnetic space, which is simply flat and empty. Propagating waves are thus represented by plane waves, e.g., polarized along the y-direction*

$$\mathbf{E} = E_0 \, e^{i\tilde{\beta}x'} \mathbf{e}_{y'},$$

propagating in the x'-direction.

*We ignore the z-dependence of the surface wave as it is not crucial to the argument considered here.

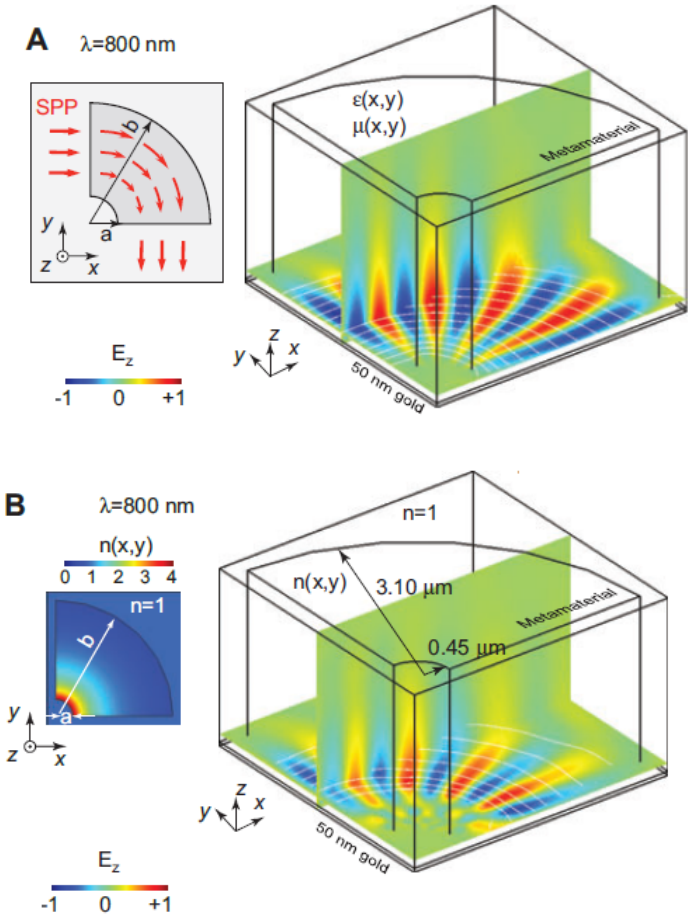

Figure 2.7: A 90-degree beam bend of plasmonic waves with anisotropic material parameters (up) and isotropic parameters (down) due to a quasi-conformal transformation. Figure reproduced with permission from Ref. [27].

Second, since electric fields are covectors, they transform according to the Jacobian of the coordinate transformation

$$\begin{aligned} E_i &= \Lambda_i^{i'} E_{i'}, \\ &= \Lambda_i^{y'} E_{y'}, \\ E_r &= E_0 \, e^{i\tilde{\beta}\, b\, (1-\frac{2}{\pi}\phi)}, \end{aligned} \tag{2.27}$$

where the y'-polarization of the electric field is transformed to a radial polarization and the phase advances with the azimuthal angle ϕ instead of x'.

Since the equivalence relations map the physical-space Maxwell equations onto those of the transformation-optical device, Eq. (2.27) is a solution of the involved wave equations

of a bi-anisotropic transformation-optical device. The fields propagate inside the device as if they are a 'turning' plane wave, in agreement with the principle of covariance.

Alternatively, a quasi-conformal proposal for a 90-degree bender uses the refractive index

$$n(r) = \frac{2}{\pi}\frac{b}{r}. \tag{2.28}$$

Fig. 2.7 shows the corresponding field amplitudes. Ref. [27] confirms that the transmission (95%) is slightly reduced with respect to the anisotropic implementation due to impedance-mismatches at the interfaces of the finitely-embedded coordinate transformation. This is in agreement with analytic coordinate transformations as discussed in section 2.2.2.

Although a partial implementation of traditional transformation-optical material parameters is successful from a practical point of view, it lacks conceptual strength and is less efficient at optical frequencies. These drawbacks appear because this approach does not take boundary conditions of the metal-dielectric interface into account. We resolve this in chapter 4.

2.3.4 Thickness Variations of the Dielectric Layer

As discussed in chapter 3 and Ref. [17], traditional two-dimensional devices use stepwise or continuous thickness variations of the dielectric layer to manipulate the propagation of surface waves through refraction or diffraction. Some of these devices are particularly effective, e.g., a Luneburg lens focuses light at its perimeter with a continuous thickness variation (Fig. 2.8). In retrospect, these devices were actually transformation-optical devices [17].

We illustrate the importance of thickness variations for a quasi-conformal Luneburg lens with an effective index of refraction

$$n(r) = \sqrt{2 - \left(\frac{r}{R}\right)^2}, \tag{2.29}$$

depending on the radial coordinate r with respect to the center of the lens and the radius R of the lens. Instead of implementing this refractive index, Ref. [28] proposes to modify the propagation constant β with a thickness variation.

Using the insights of our research on the slab waveguide (chapter 4 and chapter 5), we give a prelude to how thickness variations may become a part of a two-dimensional guided transformation optics, capable of manipulating surface waves in an effective way.

The relevant parameters of an electromagnetic device, in this case the refractive index profile and/or the thickness of the dielectric layer, are to be varied in such a way that it sustains a particular desired solution, e.g., provided by transformation optics (2.27). In agreement with thickness variations as a way to manipulate guided modes, we

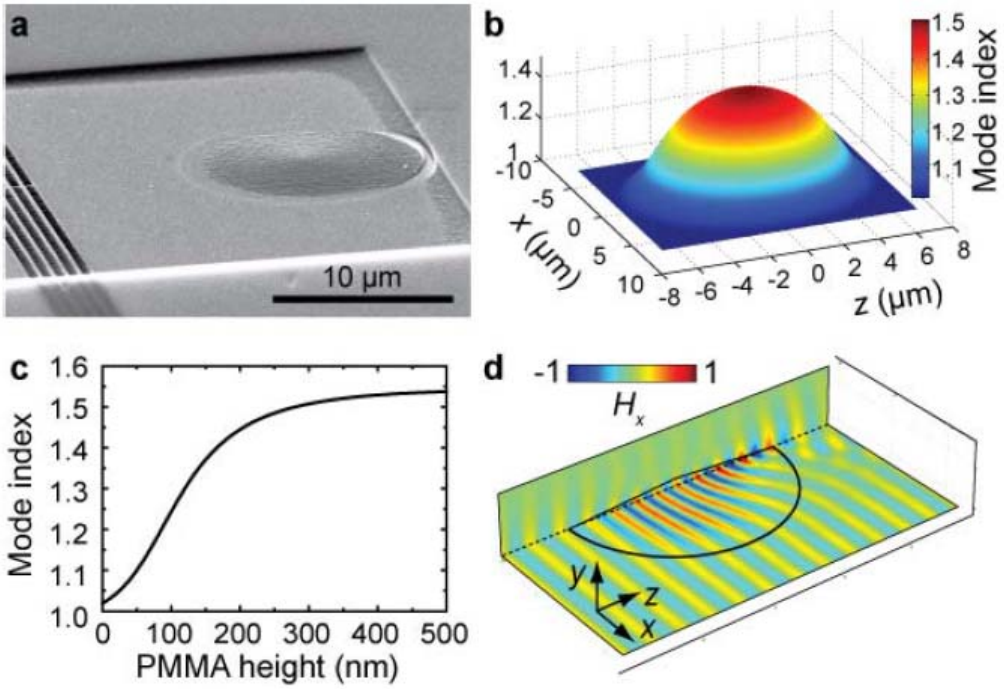

Figure 2.8: A $13\mu m$ diameter plasmonic Luneburg lens at $\lambda = 810nm$ designed with two-dimensional transformation optics using a thickness variation and a homogeneous medium: a) Scanning Electron Microscopy image b) effective index profile c) calibration of height versus mode index d) Normalized magnetic field with metal-dielectric interface in the xz-plane. Figure reproduced with permission from Ref. [28].

introduce a second step in the formulation of equivalence relations which includes the geometrical thickness of the dielectric slab as a parameter.

In the case of a 90-degree beam bender, the transformation-optical solutions (2.27) have an inhomogeneous phase $\phi(x^i)$. In the ray approximation, this is related to the propagation vector $\boldsymbol{\beta}$ of the plane wave $e^{i\phi(x^i)}$[1]

$$\boldsymbol{\beta} = \nabla\phi(x^i), \tag{2.30}$$

$$= \frac{1}{r}\frac{2b}{\pi}\tilde{\boldsymbol{\beta}}, \tag{2.31}$$

were we use the gradient operator in cylindrical coordinates. The propagation constant in the device β contains the propagation constant $\tilde{\beta}$ of the incident wave which would remain unmodified if there was no thickness variation.

As will be explained in more detail in chapters 3 and 4, the dispersion relation of material interfaces relates the thickness a of the dielectric layer to the propagation vector β. For the metal-dielectric-air interface in Fig. 2.5, this dispersion relation is equal to [16]

$$\tanh(k_D a) = \frac{\alpha_V\alpha_D + \alpha_D\alpha_M}{\alpha_D^2 + \alpha_V\alpha_M}, \tag{2.32}$$

with coefficients α_i for each $i \in \{M, D, V\}$ (2.25)

$$\alpha_i = \frac{k_i}{\epsilon_i} = \frac{\sqrt{\beta^2 - \epsilon_i\frac{\omega^2}{c^2}}}{\epsilon_i}.$$

It is therefore possible to solve (2.32) for the thickness a, if β is replaced by (2.31).

Finally, we point out the result (2.31) is, at first, very surprising. Although we derived the transformation of the electric field (2.27) from anisotropic coordinate transformations, the propagation vector β is equal to

$$\beta = n(r)\tilde{\beta},$$

with the quasi-conformal index $n(r)$ of Eq. (2.28). Our reasoning, however, depends on the ray approximation due to Eq. (2.30) so that both transformations yield identical results. Appendix A.3.3 summarizes the relevant assumptions and consequences of this approximation.

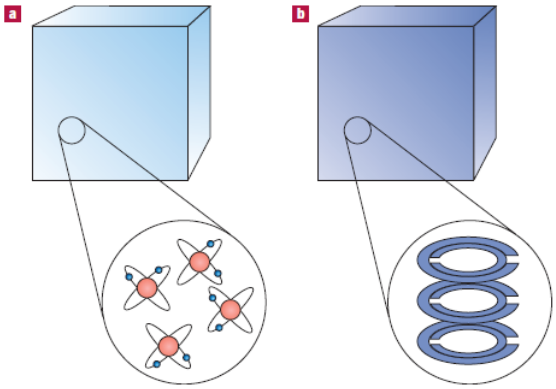

Figure 2.9: Difference between natural electromagnetic media (left) and metamaterials (right) as they impose macroscopic electromagnetic responses on light with large wavelengths. Picture reproduced with permission from Ref. [29].

2.4 Flatland Metamaterials

In the beginning of this chapter, we illustrated how transformation optics determines material parameters (2.13) and (2.14) of an optical device starting from the desired light propagation and fundamental behavior of light within the device.

These transformation-optical parameters are however highly nontrivial. For example, many devices require magnetic responses as imposed by Eq. (2.14) which are simply not accessible to natural materials at optical frequencies. Therefore, artificial materials—better known as metamaterials [29]—have been developed with fascinating electromagnetic properties which greatly extend those of natural materials [30] [31].

This section gives a general introduction to metamaterials. Additionally, we consider how graphene sheets provide a one-atom thick platform for two-dimensional transformation optics to manipulate electromagnetic waves confined to its surface.

2.4.1 Bulk Metamaterials

In the past decade, advancements in material design and nanofabrication techniques have given rise to a new class of artificial optical materials, metamaterials. Conceptually, metamaterials respond to light much in the same way as natural materials (Fig. 2.9). They consist of a structured array of fundamental constituents, meta-atoms, incorporated in a host matrix. The geometry and constitution of each meta-atom may vary throughout the material so that the local response to light is tuned in an inhomogeneous way.

Generally, metamaterials are a collection of artificial scatterers whose optical properties are determined by local responses due to each individual meta-atom. However, if the incident light has a long wavelength compared to the dimensions of the meta-atoms and their spacing, the electromagnetic responses of this collection of scatterers average so that the metamaterial is effectively described by a limited set of macroscopic material parameters, the permittivity ϵ^{ij} and permeability μ^{ij} of the metamaterial. This approximation is known as the effective medium approximation. It relates local responses, determined by the geometry and constitution of meta-atoms, to an averaged macroscopic description. Therefore, metamaterial properties directly affect the material parameters of the macroscopic Maxwell equations ((A.16) - (A.19)) which are designed by transformation optics.

Several homogenization techniques have been used to relate the local responses of each meta-atom to these averaged macroscopic responses. Some of them are analytical and existed long before metamaterials were conceived, such as the Clausius-Mosotti theory [32]—well-known for describing the polarization of an isotropic material—and the Maxwell Garnett theory [33]—applied to metallic spherical inclusions in a dielectric matrix. Other, more accurate determinations of macroscopic material parameters are provided by numerical calculations [34] or an experimental parameter retrieval technique which measures the transmission and reflection of light from a metamaterial slab to probe its material parameters [35].

The split-ring resonator (SRR), which was crucial to the first implementation of a cylindrical metamaterial cloak (Fig. 2.1), was the first meta-atom which effectively produced nontrivial and anisotropic magnetic responses. It consists of a metallic circuit with resonance frequency $\omega_0 = \frac{1}{\sqrt{LC}}$ derived from an electrostatic RLC model.

To obtain high magnetic responses, the split-ring resonators need to be excited by electromagnetic waves whose frequencies are close to the resonance frequency ω_0. However, resonance frequencies naturally induce dissipation losses in the meta-atom circuits [36]. In total, attenuations up to 10 dB per wavelength at optical frequencies have been observed for this kind of metamaterials. Generally, magnetic metamaterials are always adversely affected by loss. This motivates our search for two-dimensional nonmagnetic metamaterials.

Literature provides three solutions to mitigate dissipative losses of resonant metamaterials. First, one might avoid metallic resonant meta-atoms altogether and explore other promising materials such as high-temperature superconductors [37] and graphene [38]. However, a comparative study [36] pointed out that noble metals still outperform these materials at infrared and visible frequencies so that they are not suited for metamaterial implementations of integrated optical devices on photonic circuits as envisioned by this dissertation.

Because noble metals are expected to remain part of most metamaterial designs, literature contains various proposals for optimizing metallic meta-atoms as illustrated by Fig. 2.10. These meta-atoms implement a specific kind of hyperbolic metamaterials [39],

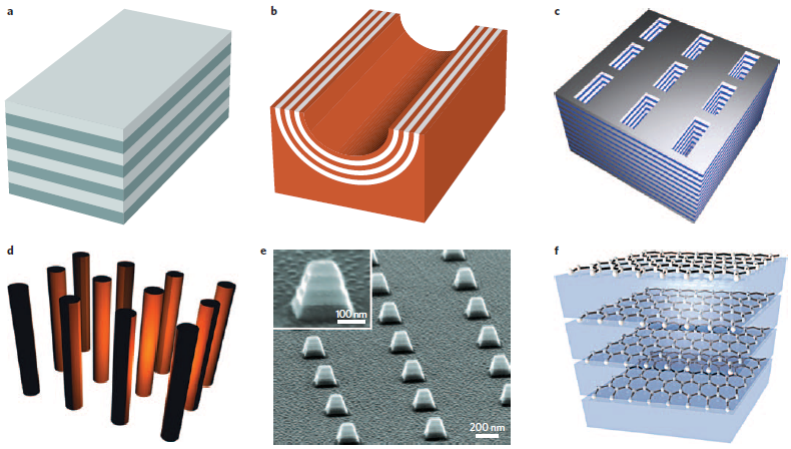

Figure 2.10: Examples of several hyperbolic metamaterials: a) Layered metal-dielectric structure, b) hyperlens, c) multilayer fishnet, d) nanorod arrays, e) arrays of metal-dielectric nanopyramids, f) graphene metamaterials. Picture reproduced with permission from Ref. [39].

which are important to applications in quantum optics, i.e. enhancement of stimulated Raman emission, and allowed designing subwavelength lensing systems. In particular, the meta-atom nanorods provide inhomogeneous uniaxial metamaterials which may be of great use to implement our beam bend design in chapter 5.

A second approach to eliminating losses of metamaterial implementations simply optimizes the design of the envisioned device, e.g., with quasi-conformal techniques, in such a way that anisotropic metamaterials are not required (subsection 2.2.2). This is indeed a promising approach at optical frequencies, as illustrated by the fabrication of a planar invisibility cloak [15].

Finally, one might use thin material sheets instead of bulk metamaterials, such that light is only slightly attenuated [40]. In this respect, two-dimensional meta-surfaces provide a new perspective to metamaterial applications. At infrared frequencies, one-atom thick material layers such as graphene provide interesting platforms to transformation-optical devices as discussed in the following subsection.

2.4.2 Graphene, a One-Atom Thick Platform

Although graphene has only been discovered a decade ago, its robustness and versatile chemical and optical properties make sure it is a key element to many nanophotonic optical devices [38]. Compared to metallic metamaterials, such as traditional split-ring resonators, graphene has the advantage that its response to light is tunable by external electric fields or bias potentials. Externally applied fields change the number of charge carriers which affect graphene's complex conductivity $\sigma = \sigma_r + i\sigma_i$ through variations

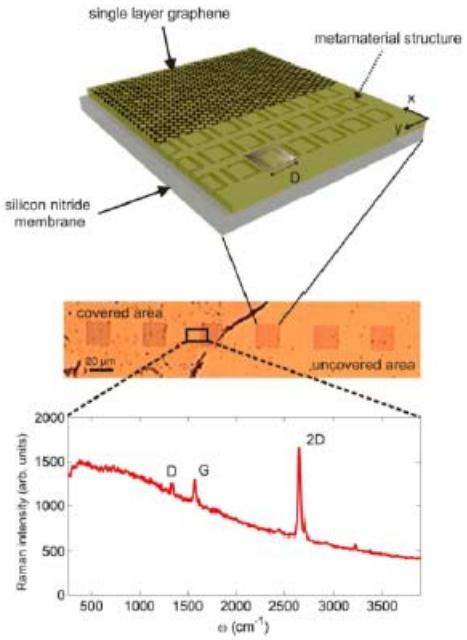

Figure 2.11: A hyrbid graphene split-ring resonator metamaterial which allows shifting the resonance and transmission efficiency of the resonator array: a schematic view (top), a microscopic image (middle) and a Raman spectrum (bottom). Figure obtained from Ref. [41]

in its chemical potential. Therefore, electrostatic doping affects the electromagnetic properties of the graphene sheet.

In combination with resonant metallic circuits, e.g., split-ring resonators, graphene is an attractive material as they allow to tune the resonance frequency and hence the response of the metamaterial. An example of such metamaterials is shown in inset f) of Fig. 2.11. The metallic circuits produce locally confined fields which enhance graphene's weak electromagnetic response, which may be modulated by external bias voltages [41]. These hybrid metamaterials are very important to plasmonic circuitry as they provide fast surface wave modulators and sensitive photodetectors.

In the context of two-dimensional metamaterials, the tunability of graphene may assume another important role [42]. Transverse magnetic surface waves on graphene—containing one in-plane magnetic component orthogonal to the propagation vector β—are only allowed by Maxwell's equations if they satisfy the following dispersion relation which contains the vacuum impedance $\eta_0 = \frac{\mu_0}{\epsilon_0}$ and conductivity σ

$$\beta^2 = \frac{\omega^2}{c^2}\left[1 - \left(\frac{2}{\eta_0 \sigma}\right)^2\right]. \tag{2.33}$$

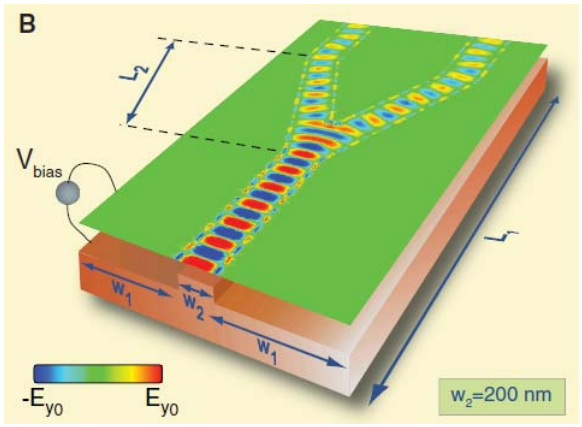

Figure 2.12: A beam splitter for transverse magnetic confined waves on a sheet of graphene with geometrical properties $L_1 = 1077nm$, $L_2 = 560nm$ and $w_1 + w_2 + w_3 = 600 + 200 + 600nm$. Figure reproduced with permission from Ref. [42].

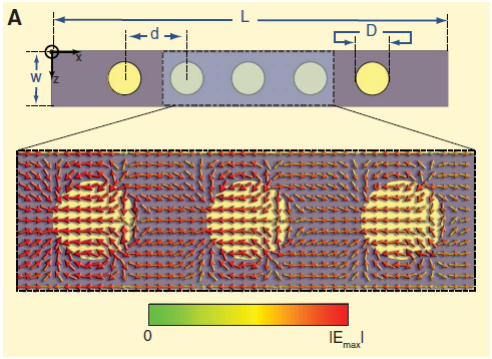

Figure 2.13: Creation of metallic scatterers on graphene for transversal-magnetic confined waves on the sheet. Figure reproduced with permission from Ref. [42].

At terahertz frequencies, however, the imaginary part of the conductivity σ_i might become negative for sufficiently strong local electric fields, such that transverse magnetic waves are no longer sustained. Fig. 2.12 shows how inhomogeneous local fields, arising from different thicknesses of the substrate layer material, select locations of negative σ_i in such a way that a beam splitter is implemented on a one-atom thick platform.

Next to truly two-dimensional transformation-optical devices, graphene also contributes to new kinds of flatland meta-atoms (Fig. 2.13). If bias potentials are applied in the right way, the sheet contains spherical islands which do not sustain transverse magnetic waves and act as a collection of local metallic scatterers which provide a homogenized response after field averaging.

The remainder of this dissertation develops a new framework to design material properties of another important two-dimensional medium, a slab waveguide.

References

[1] E. Wolf and M. Born, *Principles of Optics*, Pergamon press, 1965.

[2] S. M. Caroll, *An introduction to General Relativity, Space-time and Geometry*, Addison-Wesly, 2004.

[3] J. B. Pendry, D. Schurig, and D. R. Smith, "Controlling electromagnetic fields," *Science* **312**, 1780–1782, 2006.

[4] U. Leonhardt and T. G. Philbin, "Transformation optics and the geometry of light," *Progress in Optics* **53**, 69–152, 2009.

[5] M. D. Rahm, D. A. Roberts, J. B. Pendry, and D. R. Smith, "Transformation-optical design of adaptive beam bends and beam expanders," *Optics Express* **16**, 11555–11567, 2008.

[6] M. D. Rahm, S. A. Cummer, D. Schurig, J. B. Pendry, and D. R. Smith, "Optical design of reflectionless complex media by finite-embedded coordinate transformations," *Physical Review Letters* **100**, 063903–063908, 2008.

[7] J. B. Pendry, "Negative refraction makes a perfect lens," *Physical Review Letters* **85**, 3966–3969, 2000.

[8] J. Rho, Z. Ye, Y. Xiong, X. Yin, Z. Liu, H. Choi, G. Bartal, and X. Zhang, "Spherical hyperlens for two-dimensional sub-diffractional imaging at visible frequencies," *Nature Communications* **1**, 143–147, 2010.

[9] U. Leonhardt, "Optical conformal mapping," *Science* **312**, 1777–1780, 2006.

[10] D. Schurig, J. J. Mock, B. J. Justice, S. A.Cummer, J. B. Pendry, A. F. Starr, and D. R. Smith, "Metamaterial electromagnetic cloak at microwave frequencies," *Science* **314**, 977–980, 2006.

[11] P. G. N. Yu, M. A. Kats, F. Aieta, J. Tetienne, F. Capasso, and Z. Gaburro, "Light propagation with phase discontinuities: generalized laws of reflection and refraction," *Science* **334**, 333–337, 2011.

[12] I. I. Smolyaninov, "Metamaterial 'multiverse'," *Journal of Optics* **13**, 024004–024017, 2011.

[13] T. Tyc, H. Chen, C. T. Chan, and U. Leonhardt, "Non-euclidean cloaking for light waves," *Selected Topics in Quantum Electronics, IEEE Journal* **16**, 418–426, 2010.

[14] K. Yao, X. Jiang, and H. Chen, "Collimating lenses from non-euclidean transformation optics," *New Journal of Physics* **14**, 023011–023019, 2012.

[15] T. Ergin, N. Stenger, P. Brenner, J. B. Pendry, and M. Wegener, "Three-dimensional invisibility cloak at optical wavelengths," *Science* **328**, 337–339, 2010.

[16] T. W. Ebbesen, C. Genet, and S. I. Bozhevolnyi, "Surface-plasmon circuitry," *Physics Today* **61**, 44–50, 2008.

[17] R. R. A. Syms and J. R. Cozens, *Optical Guided Waves and Devices*, McGraw-Hill, London, 1992.

[18] M. I. D'yakonov, "New type of electromagnetic wave propagating at an interface," *Soviet Physical Journal of Experimental and Theoretical Physics* **67**, 714–716, 1988.

[19] S. A. Maier, *Plasmonics: Fundamentals and Applications*, Springer, 2007.

[20] L. H. Gabrielli, D. Liu, S. G. Johnson, and M. Lipson, "On-chip transformation optics for multimode waveguide bends," *Nature communications* **3**, 1217–1222, 2012.

[21] J. B. Pendry, A. Aubry, D. R. Smith, and S. A. Maier, "Transformation optics and subwavelength control of light," *Science* **337**, 549–552, 2012.

[22] N. I. Landy and W. J. Padilla, "Guiding light with conformal transformations," *Optics Express* **17**, 14872–14879, 2009.

[23] R. Schinzinger and P. A. A. Laura, *Conformal mapping: methods and applications*, Courier Dover Publications, 2012.

[24] J. Li and J. B. Pendry, "Hiding under the carpet: a new strategy for cloaking," *ArXiv Preprint arXiv:0806.4396* , 2008.

[25] R. Bekenstein, J. Nemirovsky, I. Kaminer, and M. Segev, "Shape-preserving accelerating electromagnetic wave packets in curved space," *Physics Review X* **4**, 011038, 2014.

[26] P. A. Huidobro, M. L. Nesterov, L. Martin-Moreno, and F. J. Garcia-Vidal, "Transformation optics for plasmonics," *Nano Letters* **10**, 1985–1990, 2010.

[27] M. Kadic, S. Guenneau, S. Enoch, P. A. Huidobro, L. Martín-Moreno, F. J. García-Vidal, J. Renger, and R. Quidant, "Transformation plasmonics," *Nanophotonics* **1**, 51–64, 2012.

[28] T. Zentgraf, Y. Liu, M. H. Mikkelsen, J. Valentine, and X. Zhang, "Plasmonic luneburg and eaton lenses," *Nature Nanotechnology* **6**, 151–155, 2011.

[29] J. B. Pendry, "Photonics: Metamaterials in the sunshine," *Nature Materials* **5**, 599–600, 2006.

[30] D. R. Smith, J. B. Pendry, and M. C. K. Wiltshire, "Metamaterials and negative refractive index," *Science* **305**, 788–792, 2004.

[31] P. Tassin, L. Zhang, T. Koschny, E. N.Economou, and C. M. Soukoulis, "Low-loss metamaterials based on classical electromagnetically induced transparency," *Physical Review Letters* **102**, 053901, 2009.

[32] J. D. Jackson, *Classical electrodynamics, 3rd ed.*, Wiley, 1998.

[33] R. Ruppin, "Evaluation of extended maxwell-garnett theories," *Optics Communications* **182**, 273–279, 2000.

[34] D. R. Smith and J. B. Pendry, "Homogenization of metamaterials by field averaging," *Journal of the Optical Society of America B* **23**, 391–403, 2006.

[35] D. R. Smith, D. Vier, T. Koschny, and C. M. Soukoulis, "Electromagnetic parameter retrieval from inhomogeneous metamaterials," *Physical Review E* **71**, 036617–036627, 2005.

[36] P. Tassin, T. Koschny, M. Kafesaki, and C. M. Soukoulis, "A comparison of graphene, superconductors and metals as cconductors for metamaterials and plasmonics," *Nature Photonics* **6**, 259–264, 2012.

[37] S. M. Anlage, "The physics and applications of superconducting metamaterials," *Journal of Optics* **13**, 024001, 2011.

[38] J. F. García de Abajo, "Graphene nanophotonics," *Science* **339**, 917–918, 2013.

[39] I. V. Iorsh, I. S. Mukhin, I. V. Shadrivov, P. A. Belov, and Y. S. Kivshar, "Hyperbolic metamaterials based on multilayer graphene structures," *Physical Review B* **87**, 075416–075420, 2013.

[40] N. K. Grady, J. E. Heyes, D. R. Chowdhury, Y. Zeng, M. T. Reiten, A. K. Azad, A. Taylor, D. A. R. Dalvit, and H. T. Chen, "Terahertz metamaterials for linear polarization conversion and anomalous refraction," *Science* **340**, 1304–1307, 2013.

[41] A. N. Grigorenko, M. Polini, and K. Novoselov, "Graphene plasmonics," *Nature Photonics* **6**, 749–758, 2012.

[42] A. Vakil and N. Engheta, "Transformation optics using graphene," *Science* **332**, 1291–1294, 2011.

Chapter 3

The Slab Waveguide

Dielectric slab waveguides provide a familiar platform for two-dimensional guided waves. Because the slab problem is similar to that of a quantum well, Maxwell's equations identify a particular orthogonal class of guided waves, the guided modes, with respect to which arbitrary confined waves may be investigated. On the conceptual level, this chapter provides the foundations of guided mode propagation in order to understand how they are to be manipulated. This provides us with tools to formulate a consistent two-dimensional transformation-optical framework in chapter 4. Numerically, we establish three criteria to interpret and evaluate finite-element simulations. In chapter 5 we apply these criteria to the design of a beam bender.

3.1 Macroscopic Maxwell Equations

As explained in appendix A, sufficiently dense media are described by the macroscopic Maxwell equations in the presence of free charges ρ_{free} and currents $\mathbf{j}_{\text{free}}$

$$\nabla \cdot \boldsymbol{\mathcal{D}} = \rho_{\text{free}}, \tag{3.1}$$
$$\nabla \cdot \boldsymbol{\mathcal{B}} = 0, \tag{3.2}$$
$$\nabla \times \boldsymbol{\mathcal{E}} = -\partial_t \boldsymbol{\mathcal{B}}, \tag{3.3}$$
$$\nabla \times \boldsymbol{\mathcal{H}} = \mathbf{j}_{\text{free}} + \partial_t \boldsymbol{\mathcal{D}}. \tag{3.4}$$

We use a curly typeset for expressiong of the electric field $\boldsymbol{\mathcal{E}}$ and the magnetic field strength $\boldsymbol{\mathcal{H}}$ in the time domain.*

This chapter investigates solutions to these Maxwell equations which are confined to a homogeneous, isotropic slab wave guide shown in Fig. 3.1. A slab waveguide consists of three discrete dielectric material layers—a substrate layer, a guiding layer and a cover

*Notational conventions are listed in table A.1 of appendix A.

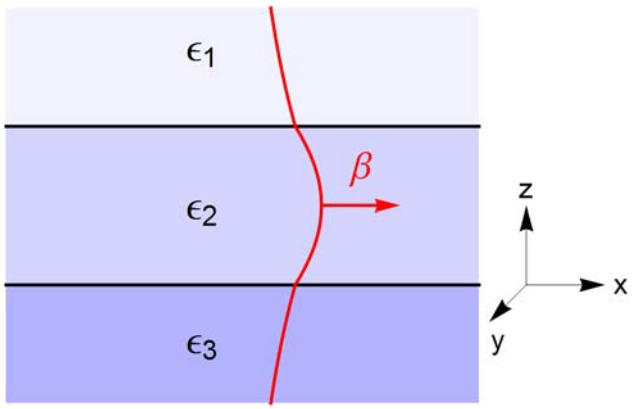

Figure 3.1: A slab waveguide, consisting of a cover layer ϵ_1, a guiding layer ϵ_2 and a substrate layer ϵ_3 parallel to the xy plane. The fundamental mode propagates in the plane with a propagation vector β.

layer—which are orthogonal to the z-axis in our reference frame. Therefore, we impose linear, local and instantaneous constitutive relations

$$\boldsymbol{\mathcal{D}} = \epsilon_0 \, \epsilon(z) \, \boldsymbol{\mathcal{E}}, \tag{3.5}$$

$$\boldsymbol{\mathcal{B}} = \mu_0 \, \boldsymbol{\mathcal{H}}, \tag{3.6}$$

with a stepwise relative permittivity profile $\epsilon(z)$ in the orthogonal coordinate z

$$\epsilon(z) = \begin{cases} \epsilon_1 & z > a, \\ \epsilon_2 & -a \leq z \leq a, \\ \epsilon_3 & z < -a. \end{cases} \tag{3.7}$$

The slab waveguide is fundamentally different from bulk, infinitely extended media. Because bulk media are translationally invariant in every direction, all monochromatic solutions with frequency ω are expandable with respect to a complete basis of plane waves

$$\boldsymbol{\mathcal{E}} = \frac{1}{(2\pi)^3} \int d\mathbf{k} \, \tilde{\mathbf{E}}(\mathbf{k}) \, e^{\mathrm{i}(\mathbf{k} \cdot \mathbf{r})} \, e^{-\mathrm{i}\omega t}, \tag{3.8}$$

$$\boldsymbol{\mathcal{H}} = \frac{1}{(2\pi)^3} \int d\mathbf{k} \, \tilde{\mathbf{H}}(\mathbf{k}) \, e^{\mathrm{i}(\mathbf{k} \cdot \mathbf{r})} \, e^{-\mathrm{i}\omega t}, \tag{3.9}$$

where the magnitude of wave vector $\mathbf{k}$ is fixed by a dispersion relation depending on the refractive index n of the medium

$$k^2 = n^2 \, \frac{\omega^2}{c^2}. \tag{3.10}$$

Eqs. (3.8)- (3.9) are crucial to the *plane wave expansion technique* which solves for the coefficients $\tilde{\mathbf{E}}(\mathbf{k})$ and $\tilde{\mathbf{H}}(\mathbf{k})$ to determine wave propagation within an unconstrained

medium. Each plane wave component $\tilde{\mathbf{E}}(\mathbf{k})$ and $\tilde{\mathbf{H}}(\mathbf{k})$ has a transverse polarization with respect to its propagation direction and does not depend on the coordinates parallel to that direction.

In contrast, the slab waveguide of thickness $2a$ in Fig. 3.1 is a constrained medium. The permittivity profile (3.7) breaks the translation symmetry in the orthogonal direction z with respect to a bulk material. Therefore, solutions to the Maxwell equations are subject to boundary conditions at dielectric interfaces with normal $\mathbf{n}$

$$\mathbf{n} \times \mathcal{E} = 0 \quad \text{Continuous tangential } \boldsymbol{\mathcal{E}} \text{ components,} \tag{3.11}$$
$$\mathbf{n} \times \mathcal{H} = 0 \quad \text{Continuous tangential } \boldsymbol{\mathcal{H}} \text{ components,} \tag{3.12}$$
$$\mathbf{n} \cdot \mathcal{D} = 0 \quad \text{Continuous normal } \boldsymbol{\mathcal{D}} \text{ component,} \tag{3.13}$$
$$\mathbf{n} \cdot \mathcal{B} = 0 \quad \text{Continuous normal } \boldsymbol{\mathcal{B}} \text{ component.} \tag{3.14}$$

These conditions introduce geometrical dependencies to the slab waveguide solutions, i. e. the location of the material interfaces.

This chapter explains how—analogous to the plane wave expansions (3.8)-(3.9)— propagation of an initial confined wave profile is determined by monochromatic two-dimensional (guided) modes with angular frequency ω

$$\boldsymbol{\mathcal{E}} = \mathbf{E}(x, y, z)\, e^{-\mathrm{i}\omega t}, \quad \boldsymbol{\mathcal{H}} = \mathbf{H}(x, y, z)\, e^{-\mathrm{i}\omega t}.$$

Because the material parameters, e.g., the permittivity profile $\epsilon(z)$, distinguish between planar xy and orthogonal z coordinates, we assume that these guided modes conform to separation of variables

$$\mathbf{E}(x, y, z) = \mathbf{Z}_E(z)\, e^{\mathrm{i}\beta x}, \quad \mathbf{H}(x, y, z) = \mathbf{Z}_H(z)\, e^{\mathrm{i}\beta x}. \tag{3.15}$$

Before we derive guided mode solutions, it is instructive to eliminate some redundancy which is inherent to the complete set of Maxwell equations. Because the dielectric does not contain free charges ρ_{free} or currents $\mathbf{j}_{\text{free}}$, the electric and magnetic Gauss laws Eqs. (3.1)-(3.2) are automatically taken into account by the law of Faraday Eq. (3.3) and Ampère Eq. (3.4). These reduce to the following six coupled scalar equations when applied to the separated solutions (3.15),

$$\begin{aligned} \partial_z H_y &= \mathrm{i}\omega\epsilon_0\, \epsilon(z)\, E_x, \\ \omega\mu_0\, H_y &= \partial_z E_x - \mathrm{i}\beta\, E_z, \\ \beta\, H_y &= -\omega\epsilon_0\, \epsilon(z)\, E_z. \end{aligned} \tag{3.16}$$

$$\begin{aligned} \partial_z E_y &= -\mathrm{i}\omega\mu_0\, H_x, \\ \omega\epsilon_0\, \epsilon(z)\, E_y &= \mathrm{i}\beta\, H_z - \partial_z H_x, \\ \beta\, E_y &= \omega\mu_0\, H_z. \end{aligned} \tag{3.17}$$

Eq. (3.16) and Eq. (3.17) identify two sets of self-contained solutions which are distinguished by their polarization. The transverse magnetic polarization (TM) with E_x, E_z and H_y is sensitive to the transversal permittivity profile thanks to the orthogonal electric field E_z, while the transverse electric polarization with H_x, H_z and E_y is not fundamentally affected by the permittivity profile.

The TM and TE solutions are respectively determined by the transverse components H_y or E_y. Thus, Eq. (3.16) and Eq. (3.17) decouple into two independent scalar equations for each region $i \in \{1, 2, 3\}$

$$\partial_x^2 H_y + \partial_z^2 H_y + \epsilon_i \frac{\omega^2}{c^2} H_y = 0, \tag{3.18}$$

$$\partial_x^2 E_y + \partial_z^2 E_y + \epsilon_i \frac{\omega^2}{c^2} E_y = 0, \tag{3.19}$$

which completely determine the confined solutions without any additional approximation. These equations are particular examples of the general Helmholtz equations in homogeneous media

$$\begin{aligned} \Delta H_y + \epsilon_i \frac{\omega^2}{c^2} H_y = 0, \\ \Delta E_y + \epsilon_i \frac{\omega^2}{c^2} E_y = 0, \end{aligned} \tag{3.20}$$

with Laplacian

$$\begin{aligned} \Delta &= \partial_x^2 + \partial_y^2 + \partial_z^2, \\ &= \Delta_{xy} + \partial_z^2. \end{aligned} \tag{3.21}$$

Importantly, separability of the electromagnetic fields implies the Laplacian operator also splits into an in-plane Δ_{xy} and an orthogonal ∂_z^2 operator. Transformation optics will be used to modify the in-plane Laplacian in chapter 4. For now, we established that confined solutions with a particular TM polarization are crucially determined by one Helmholtz equation. This equation is valid at the same level as the original Maxwell equations describing the waveguide (3.1)-(3.4).

3.2 Guided Modes

3.2.1 Implications of Separability

As suggested by (3.21), the generalized Helmholtz equation (3.20) splits into two distinct parts when acting on a separable solution

$$H_y = \Phi_H(x, y)\, Z_H(z).$$

If we define a separation constant β, the in-plane propagation equation

$$\Delta_{xy} \Phi_H(x, y) = -\beta^2 \Phi_H(x, y), \tag{3.22}$$

is solved by a two-dimensional infinitely-extended plane wave while the orthogonal modal equation remains to be solved

$$\partial_z^2 Z_H(z) + \left[\epsilon(z)\frac{\omega^2}{c^2} - \beta^2\right] Z_H(z) = 0. \tag{3.23}$$

For a plane wave ansatz (3.15), the TM Maxwell equations (3.16) reduce to

$$\mathbf{E} = \begin{pmatrix} \frac{-i}{\epsilon_0 \omega\ \epsilon_i}\ \partial_z Z_H(z) \\ 0 \\ \frac{-\beta}{\epsilon_0 \omega\ \epsilon_i}\ Z_H(z) \end{pmatrix} \quad \mathbf{H} = \begin{pmatrix} 0 \\ Z_H(z) \\ 0 \end{pmatrix}.$$

Similar to a plane wave expansion, we investigate the propagation of arbitrary confined waves $H_{y\ in}$ in terms of a superposition of independently propagating guided modes $Z_H^{(m)}$ enumerated by an integer positive number $m \in \mathbb{N}$

$$H_{y\ in}(x,z) = \sum_m^N \tilde{H}_m\ Z_H^{(m)}(z)\ e^{\mathrm{i}\beta^{(m)}x}. \tag{3.24}$$

To this aim, we require a norm that selects the parts of $H_{y\ in}$ which belong to a specific guided mode [1]. Fortunately, guided waves are confined to the waveguide such that the time-averaged Poynting vector

$$\begin{aligned} \mathbf{S} &= \frac{1}{2}\ \mathrm{Re}\left[\ \mathbf{E} \times \mathbf{H}^*\ \right], \\ &= \frac{\beta}{2\omega\epsilon_0\ \epsilon_i}\ |Z_H(z)|^2\ \mathbf{e}_x, \end{aligned}$$

corresponds to a finite power

$$P = \frac{\beta}{2\epsilon_0\omega} \int dz\ \frac{1}{\epsilon(z)} |Z_H(z)|^2 < \infty. \tag{3.25}$$

Therefore, it is possible to construct a Hilbert space with a norm associated to TM waves

$$\langle f, g \rangle = \int \mathrm{d}z\ \frac{1}{\epsilon(z)}\ f(z) g^*(z). \tag{3.26}$$

The modal wave equation (3.23) reduces to a one-dimensional eigenvalue problem connected to the Hermitian mode operator $\hat{L}$

$$\hat{L} = \left[\partial_z^2 + \epsilon_i\right]$$

with discrete eigenvalues $\beta^{(m)}$ and an orthogonal set of eigenfunctions $Z_H^{(m)}$

$$\hat{L} Z_H^{(m)} = (\beta^{(m)})^2 Z_H^{(m)}. \tag{3.27}$$

Thus, when applied to eigenmodes $Z_H^{(m)}(z)$, Eq. (3.25) expresses the modal power P_m corresponding to the order m,

$$P_m = \frac{\beta}{2\epsilon_0\omega}\int dz\ \frac{1}{\epsilon(z)}|Z_H^{(m)}(z)|^2, \tag{3.28}$$

associated to a guided mode of order m. This coefficient provides an effective way to measure the efficiency with which a waveguide transports a particular guided mode. We will keep track of the fundamental mode $Z_H^{(0)}$ which we want to manipulate with a consistent, two-dimensional, guided transformation optics.

3.2.2 Transverse Magnetic Modes

We now present a traditional approach to finding the guided modes of a planar slab waveguide [2]. Since the modal equation (3.23) in each region $i \in \{1,2,3\}$ of the slab contains constant coefficients k_i

$$k_1^2 = \beta^2 - \epsilon_1\frac{\omega^2}{c^2}, \tag{3.29}$$

$$k_2^2 = \epsilon_2\frac{\omega^2}{c^2} - \beta^2, \tag{3.30}$$

$$k_3^2 = \beta^2 - \epsilon_3\frac{\omega^2}{c^2}, \tag{3.31}$$

the wave equations (3.23) are readily solved by the following ansatz for the magnetic field $Z_H(z)$

$$\begin{aligned} i=1 \quad & Z_H(z) = A\ e^{k_1 z} + B\ e^{-k_1 z}, \\ i=2 \quad & Z_H(z) = C\cos(k_2 z) + D\sin(k_2 z), \\ i=3 \quad & Z_H(z) = E\ e^{k_3 z} + F\ e^{-k_3 z}. \end{aligned} \tag{3.32}$$

The wave vector coefficients k_1, k_2 and k_3 crucially determine the orthogonal dependence of the magnetic field. Fig. 3.2 distinguishes three situations.

In this dissertation, we investigate the manipulation of *guided modes*. A guided mode is confined to the slab and propagates in a parallel direction with respect to its interfaces. Therefore, the coefficients (3.29)-(3.31) are necessarily positive. In combination with the wave equations of the slab and surrounding layers, these coefficients restrict the allowed range of the effective in-plane propagation vector β at a fixed frequency. More specifically, Fig. 3.3 shows the propagation vector β lies in between three light cones, associated to free propagation in the substrate, cover and slab

$$\epsilon_1\frac{\omega}{c} < \beta < \epsilon_2\frac{\omega}{c} \quad \text{and} \quad \epsilon_3\frac{\omega}{c} < \beta < \epsilon_2\frac{\omega}{c}.$$

Therefore, the effective wavelength $\lambda_{eff} = \frac{2\pi}{\beta}$ is smaller than that of free waves in the cover or the substrate layer. We notice the guiding layer only sustains guided mode

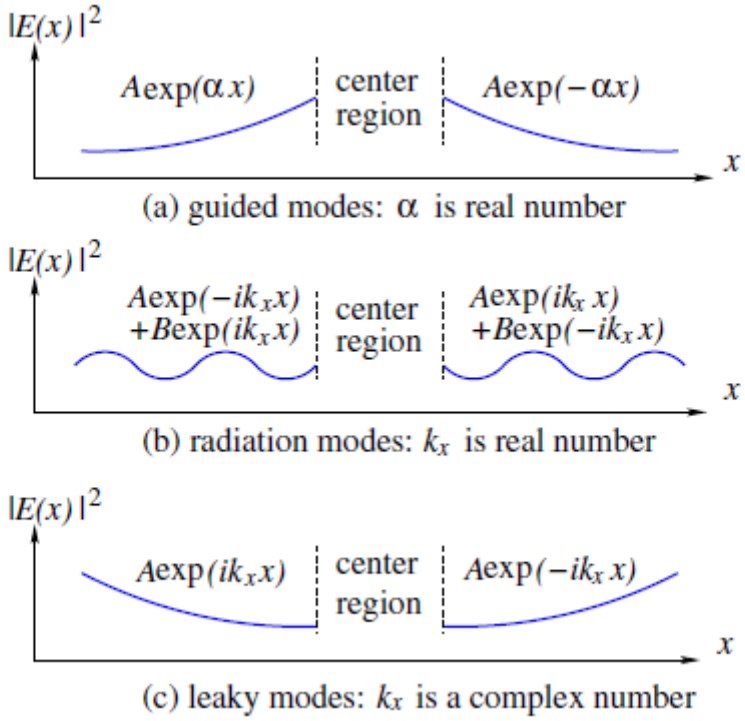

Figure 3.2: Comparison of (a) guided modes, (b) radiation modes and (c) leaky modes in a one-dimensional waveguide. Independent from detailed index variations within the guide, the modal power (solid lines) decays exponentially, oscillates or increases outside the slab. Figure reproduced with permission from Ref. [3].

solutions if it is denser than the surrounding media

$$\epsilon_1, \epsilon_3 < \epsilon_2. \tag{3.33}$$

Second, we distinguish *radiation modes*. These modes radiate energy to infinity. The coefficients k_1 and k_3 are pure imaginary numbers and the propagation vector β is smaller than that on the cover and substrate light cones. In contrast to guided modes, the normal wave vectors k_1 and k_3 take continuous values. The argument of subsection 3.2.1, which leads to discrete propagation vectors, breaks down because the power operator (3.25) does not approach zero at infinity.
Finally, the propagation vector within the slab may take complex values with non-vanishing real and imaginary components. The electromagnetic energy decays exponentially at a characteristic length $\frac{1}{Im(\beta)}$. Therefore, conservation of energy imposes that the extinction coefficients k_1 and k_3 are also partially imaginary. These solutions are called *leaky modes* despite the fact that they are no true eigenmodes of the slab waveguide. In fact, they are a linear superposition of radiation and guided modes which form a basis for all confined solutions to the slab waveguide.

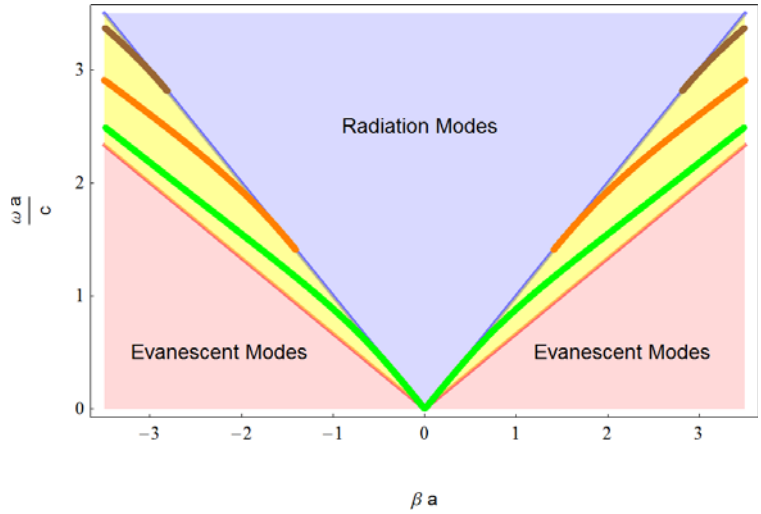

Figure 3.3: Numerical determination of TM fundamental (green), first (orange) and second order (brown) guided mode dispersion in a symmetric slab waveguide for simulational parameters of table 3.1. The light cones of the vacuum/cover (blue) and the light cone of the guiding layer (red) restrict the values of guided mode propagation constants β.

We now return to finding the guided modes associated to a particular slab waveguide. To obtain their profiles and their effective propagation vector, we apply tangential boundary conditions (3.11) and (3.12) to both interfaces $z = a$ and $z = -a$ of the slab waveguide in Fig. 3.1.

First, we deal with the problem of determining a unique solution to the Helmholtz equations. This is not guaranteed by the aforementioned boundary conditions at the material interface. Generally, a scalar field u, subject to external boundary conditions, requires a Sommerfeld radiation condition [4] at infinity which selects 'outwardly propagating' solutions. If the wave vector k associated to u is complex, the extended Sommerfeld radiation condition requires $r^3 e^{-ikr}\left[\left(ik - \frac{1}{r}\right)u - \partial_r u\right]$ is bounded. This is particularly important when deriving 'radiation modes' of a waveguide, with imaginary coefficients k_1 and k_3.

Because we are interested in purely confined guided modes, we circumvent this technical complication if we impose that

$$\lim_{z\to\pm\infty} Z_H(z) = 0.$$

Therefore, the A and F are set to zero in Eq. (3.32). The continuity of the magnetic field strength (3.12) at $z = \pm a$ provides the following constraints

$$Be^{-k_1 a} = (C\cos(k_2 a) + D\sin(k_2 a)), \tag{3.34}$$
$$Ee^{-k_3 a} = (C\cos(k_2 a) - D\sin(k_2 a)), \tag{3.35}$$

to the ansatz (3.32). Additionally, the continuity of the tangential electric field

$$Z_{E_x} = \frac{1}{\omega\epsilon_0\ \epsilon_i}\partial_z Z_{H_y} \tag{3.36}$$

amounts to

$$k_1 B e^{-k_1 a} = \frac{k_2\epsilon_1}{\epsilon_2}\left(C\sin(k_2 a) - D\cos(k_2 a)\right), \tag{3.37}$$

$$k_3 E e^{-k_3 a} = -\frac{k_2\epsilon_3}{\epsilon_2}\left(C\sin(k_2 a) + D\cos(k_2 a)\right). \tag{3.38}$$

To obtain a nontrivial solution, at least one of the coefficients B, C, D and E is different from zero. Therefore, the determinant of the four-by-four matrix associated to Eq. ((3.34)-(3.38)) vanishes if

$$\tan(2k_2 a) = \frac{\frac{k_2}{\epsilon_2}\left(\frac{k_1}{\epsilon_1} + \frac{k_3}{\epsilon_3}\right)}{\left(\left(\frac{k_2}{\epsilon_2}\right)^2 - \frac{k_1}{\epsilon_1}\frac{k_3}{\epsilon_3}\right)}. \tag{3.39}$$

This is a *dispersion relation*. Together with the Helmholtz equation, it (3.39) completely characterizes guided modes.

The dispersion relation determines the phase velocity v_ϕ of the mode through its relation to the propagation vector β

$$v_\phi(\omega) = \frac{\omega}{\beta} = \frac{c}{n_{eff}}. \tag{3.40}$$

In this way, it imposes a global refractive index n_{eff} which is not related in an analytical way to the refractive indices of the media in the guiding structure. It is because of this effective index, which removes the constraints of the guiding problem, that traditional guided wave optical devices work in much the same way as free three-dimensional optical devices [2].

Since boundary conditions of a TM wave

$$H_y \quad \text{continuous}\ ; \quad \frac{1}{\epsilon(z)}\partial_z H_y \text{ continuous}, \tag{3.41}$$

only differ from those of a TE wave through exchange of $\epsilon(z)$ and μ

$$E_y \quad \text{continuous}\ ; \quad \frac{1}{\mu(z)}\partial_z E_y \text{ continuous},$$

the dispersion relation of a TE guided mode is readily obtained from the TM dispersion relation (3.39)

$$\tan(2k_2 a) = \frac{k_2\left(k_1 + k_3\right)}{\left(k_2^2 - k_1 k_3\right)}, \tag{3.42}$$

where all permittivities ϵ_i are replaced by permeabilities μ_i. In deriving Eq. (3.42), we assume the slab is nonmagnetic with $\mu_i = 1$.

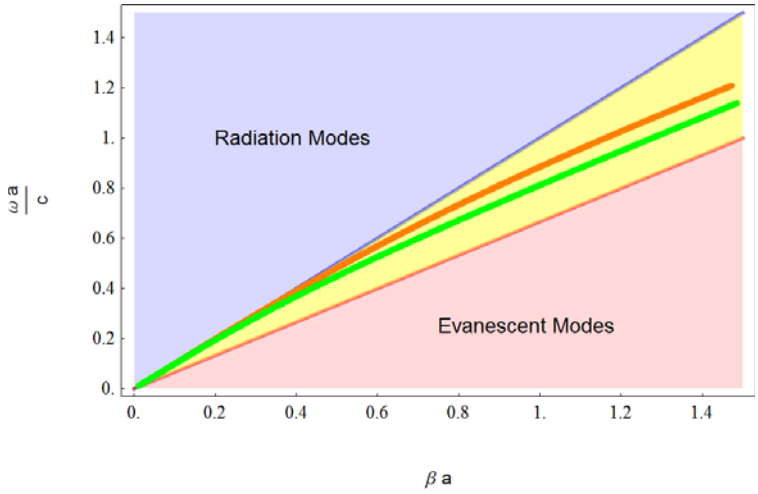

Figure 3.4: TM (orange) and TE (green) dispersion relations of the fundamental guided mode for simulation parameters of table 3.1.

After specifying some key properties of the waveguide—material parameters ϵ_i, the slab thickness $2a$ and the frequency ω—the dispersion relation determines which propagation vector β corresponds to a guided mode. In particular, Fig. 3.4 compares the fundamental TM and TE modes of the waveguide for our preferred simulation parameters of Table 3.1.

For a symmetric slab waveguide with

$$\epsilon_2 > \epsilon_1 \quad \epsilon_2 = \epsilon_3,$$

the right-hand side of the TM dispersion relation (3.39) is larger than that of the TE dispersion relation 3.42. Therefore, the TM orthogonal slab coefficient k_2 deviates more strongly from the light cone of the guiding layer than that of TE. It follows the TM mode is less sub-wavelength than the TE mode. Additionally, because both modes do not have a cut-off frequency ω_c, they always coexist in a waveguide. This has important implications when the slab waveguide is slightly perturbed, e.g. by thickness variations. Coupling between TE and TM modes is an important point of attention in subsection 3.3.3 and chapter 5.

3.2.3 A Symmetric Slab Waveguide

In the case of a symmetric slab waveguide, with identical substrate and cover layers,

$$\epsilon_1 = \epsilon_3 \quad \text{and} \quad k_1 = k_3,$$

fields are expected to be purely (anti)-symmetric with respect to the symmetry plane $z = 0$. Therefore, one material interface, e.g., $z = a$, imposes all relevant boundary conditions.

Frequency	Propagation Constant	Permittivity profile	
$f_0 = 200THz$	$\beta = 4.68\ 10^6 \frac{1}{m}$	Cover layer	$\epsilon_1 = 1$
$\tilde{\omega} = 0.848$	$\tilde{\beta} = 0.935$	Guiding layer	$\epsilon_2 = 2.25$
		Substrate layer	$\epsilon_3 = 1$

Table 3.1: Parameters of the single-mode slab waveguide with thickness $d = 2a = 0.4\ \mu m$.

The dispersion relation (3.39) now corresponds to a polynomial of second order with two non-degenerate solutions,

$$\tan(k_2 a)^2 + \tan(k_2 a)\frac{\alpha_1^2 - \alpha_2^2}{\alpha_1 \alpha_2} - 1 = 0. \tag{3.43}$$

For simplicity, we express the dispersion relation with respect to the following parameters $\alpha_1 = \frac{k_1}{\epsilon_1}$ and $\alpha_2 = \frac{k_2}{\epsilon_2}$. The discriminant of this equation is always positive and yields two independent solutions

$$\tan(k_2 a) = \frac{\epsilon_2}{\epsilon_1}\frac{k_1}{k_2} \quad \text{even TM modes,} \tag{3.44}$$

$$\tan(k_2 a) = -\frac{\epsilon_1}{\epsilon_2}\frac{k_2}{k_1} \quad \text{odd TM modes,} \tag{3.45}$$

which are either even or odd and orthogonal to each other.

Using the technical computing software *Mathematica*, we solved the dispersion relation up to third-order guided modes (Fig. 3.3) using the parameters of table 3.1.

Apart from the absence of cut-offs for the fundamental mode, the scale-invariance of the guiding problem is extremely important. It is possible to rewrite the dispersion relation (3.39) in terms of two dimensionless parameters, a dimensionless frequency ω_{eff}

$$\omega_{eff} = \frac{\omega a}{c}, \tag{3.46}$$

and an effective propagation vector β_{eff} of the mode

$$\beta_{eff} = \beta a. \tag{3.47}$$

Indeed, if the right hand side of the dispersion relation (3.3) is multiplied and divided by half the slab thickness a, this constant a may be combined with the k_1, k_2 and k_3 coefficients (3.29)-(3.31) which are expressed as a function of ω_{eff} and β_{eff}.

We now have a look at two important consequences of scale-invariance. First, the guide always sustains guided modes, even when the slab thickness is deeply subwavelength. This is very interesting for integrated applications, which currently rely on single

metal-dielectric interfaces [5]. Second, thickness variations perturb the mode profile, determined by $k_i a$ for each layer i, because they affect the magnitude of the propagation vector. Then, field profile mismatches initiate reflection and refraction processes [2]. Our new technique developed in chapter 4 will combine two sources of scattering to guided modes, a variation in the permittivity tensor of the guiding layer and a variation in thickness, in such a way that they compensate each other. To obtain an intuition for the effects of thickness variations on guided modes, we establish an analogy between the time-independent Schrödinger equation and the Helmholtz equation (3.18).

3.2.4 A Quantum Analogy

If a particle with effective mass m^* and energy E is affected by a one-dimensional potential $V(z)$, its wave equation is a solution to the time-independent Schrödinger equation

$$-\frac{\hbar^2}{2m^*}\partial_z^2\Psi + [V(z) - E] = 0. \tag{3.48}$$

This is mathematically equivalent to the Helmholtz equation (3.18) if one identifies

$$E = -\frac{\hbar^2}{2m^*}\,\beta^2,$$
$$V(z) = -\frac{\hbar^2}{2m^*}\,\frac{\omega^2}{c^2}\,\epsilon(z).$$

The permittivity profile of the slab acts as a confining potential with a geometrical thickness $2a$ and a depth

$$\frac{\hbar^2}{2m^*}\frac{\omega^2}{c^2}\left[\epsilon_2 - \epsilon_1\right].$$

If both equations are written in a dimensionless form through a rescaling of the orthogonal coordinate $\xi = \frac{z}{a}$, an effective potential V_{eff} and energy E_{eff} appear

$$E_{eff} = -\frac{\hbar^2}{2m^*}\,\beta_{eff}^2,$$
$$V_{eff}(z) = -\frac{\hbar^2}{2m^*}\,\omega_{eff}^2\,\epsilon(z). \tag{3.49}$$

We immediately recognize the dimensionless parameters, β_{eff} and ω_{eff}.

To establish a full analogy between the constrained waveguide and a quantum well, we also need consistent boundary conditions next to matched wave equations. Luckily, the boundary conditions of the quantum problem —these impose continuous probability densities and currents—

$$\Psi \quad \text{continuous} ; \quad \frac{1}{m^*}\partial_z\Psi \quad \text{continuous},$$

Mode order m	Analytical cutoff $\tilde{\omega}_c^{(m)}$	Numerical cutoff $\tilde{\omega}_c^{(m)}$
0	0.000	0.0000
1	1.4050	1.4052
2	2.8099	2.8102

Table 3.2: Comparison of numerically predicted cutoff frequencies obtained from the dispersion relation (3.52) to numerically obtained cut-offs of finite-element simulations in Fig. 3.3.

are identical to the boundary conditions of the guiding problem (3.41) if the effective mass m^* plays a similar role in quantum mechanics as the permittivity in electromagnetism. This observation lies at the heart of transformation-optical applications to effective quantum systems [6].

The previous subsection already identified the thickness as a key parameter of the dispersion relation. We now return to the effect of a thickness variation on confined waves. A thickness variation affects the effective potential and energy of the guided mode (Eq. (3.49)). On the one hand, a decrease in slab thickness also decreases the depth of the confining potential. The guided modes extend further into the outer regions and have lower extinction coefficients k_1 and k_3. On the other hand, as the thickness increases, the potential well deepens and highly confines the mode to the guide.

We distinguish three regimes. First, when the thickness is small, guided mode propagation is mostly influenced by the permittivities of the cover and the substrate. Intuitively, this is a result of low confinement when the energy of the mode mostly resides outside of the slab. Second, the high-thickness regime is dominated by the permittivity of the slab and the energy is mostly confined within the slab. Third, in the intermediate case, the guide is necessarily described by its effective index lying in between the slab and outer layer refractive indices. These observations become very relevant in chapter 5 because the importance of boundary conditions increases as the thickness decreases.

3.2.5 Field profiles and cut-off frequencies

In this subsection, we establish analytical predictions of field profiles and cut-off frequenties to benchmark numerical simulations explained in the following section. As shown in Fig. 3.3, higher order modes $Z_H^{(m)}$ with propagation vectors $\beta^{(m)}$ have a cut-off frequency $\omega_c^{(m)}$ when the extinction coefficient

$$\begin{aligned}\left(k_1^{(m)}\right)^2 &= (\beta^{(m)})^2 - \epsilon_1 \frac{\omega^2}{c^2}, \\ &= [\epsilon_2 - \epsilon_1] \frac{\omega^2}{c^2} - (k_2^{(m)})^2, \end{aligned} \tag{3.50}$$

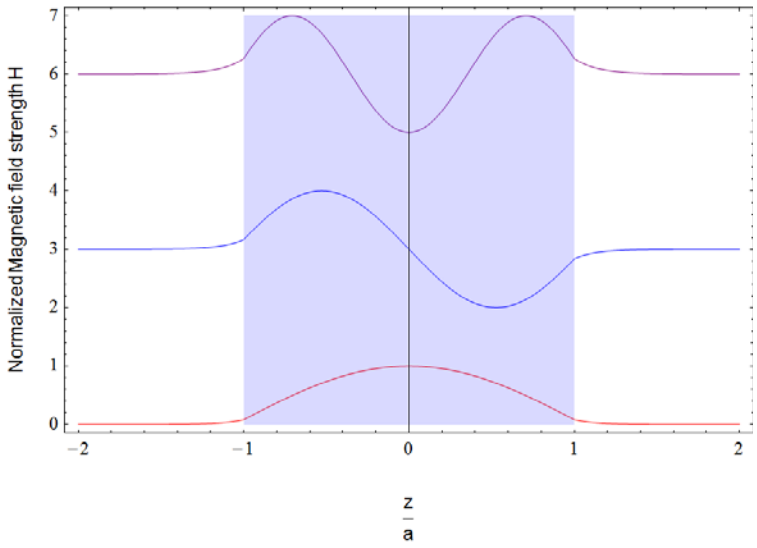

Figure 3.5: Fundamental (lower), first (middle) and second order (upper) field profiles for a frequency $1.80PHz$ and slab thickness $2a = 0.4\mu m$.

is zero. The dispersion relations ((3.44)-(3.45)) determine the associated values of the orthogonal wave-vector $k_2^{(m)}$ for eigenmodes of order m

$$k_2 a = m\frac{\pi}{2} \quad m \in \mathbb{N}. \tag{3.51}$$

If Eqs. (3.50) and (3.51) are combined, the locations of the cut-off are obtained. Table 3.2 compares the numerically obtained cut-off effective frequencies $\omega_{c,\,\mathrm{eff}}^{(m)}$ to those predicted by (3.52). It turns out they are determined by the value of the effective potential (3.49)

$$\begin{aligned} V_c^{(m)} &= a^2 (k_2^{(m)})^2, \\ &= m^2 \frac{\pi^2}{4}, \end{aligned} \tag{3.52}$$

and the associated energy E_{eff} is equal to that of a free wave propagating through the cover and the substrate.

Intuitively, cut-offs occur when the particle-analogue of the guided mode experiences no potential depth. Therefore, the V-parameter

$$V = \omega_{eff} \sqrt{\epsilon_2 - \epsilon_1}, \tag{3.53}$$

is related to the threshold potential for which all higher-order modes are not bound. It estimates how many modes a waveguide supports. Next to the number of supported modes, it is also an important parameter to estimate bending losses in optical fibers [2].

The field profiles are found when substituting the numerical solutions of ω and β into the ansatz (3.32)

$$Z_H^{(m)} = \begin{cases} cos(k_2 a + m\frac{\pi}{2})\, e^{-k_1(z-a)} & z \geq a, \\ cos(k_2 z + m\frac{\pi}{2}) & |z| \leq a, \\ (-1)^m\, cos(k_2 a + m\frac{\pi}{2})\, e^{k_1(z+a)} & z \leq -a \end{cases}, \tag{3.54}$$

using Eq. (3.29) and Eq. (3.30) to determine k_1 and k_2. Fig. 3.5 shows three modes at $1.80PHz$ corresponding to an effective potential $V_{eff} = 71.06$. Since the effective potential of sixth-order modes $V^{(6)}_{c\,eff} = 88$ is larger than the V-parameter, all orders larger than $m = 5$ are not sustained for this frequency by this particular waveguide.

3.3 Numerical Verification of the Dispersion Relation

We now compare our analytical predictions to numerically simulated guided modes. In this way we confirm the accuracy of our numerical solution of the dispersion relation before we continue to the actual derivation and confirmation of our new guided transformation-optical technique.

The commercial software *Comsol Multiphysics* provides an efficient finite-element software to solve arbitrary partial differential equations. In particular, Comsol is equipped with a dedicated radio-frequency (RF) module capable of solving Helmholtz equations in the frequency domain. Details about the solution method are provided in Appendix C.

Fig. 3.6 shows the two-dimensional simulation domain, which represents the cross-section of the slab waveguide geometry corresponding to the parameters of Table 3.1. The cross-section comprises the propagation direction and the direction normal to the slab. Thus, the TM-magnetic field lies in the direction pointing out of the page while nonzero electric field components are parallel to the propagation direction and orthogonal to the slab.

The simulation domain is highly reduced by two symmetries of the guiding problem C.2. First, infinitely extended plane waves preserve translation symmetry in the y-direction. This simplification is not applicable to diffracting waves (section 3.4) and does not include inhomogeneous media which depend on the y-coordinate (chapter 5). Second, the waveguide material parameters and fundamental modes are symmetric with respect to the xy-plane. Using appropriate boundary conditions which respect this symmetry, e.g,. Perfect Electric Conductor boundaries, the upper half of the simulation domain completely determines the guided mode solutions. Thus, the domain is half the size of the original domain. As a consequence, all our analytical and numerical results are expressed in terms of half the thickness of the waveguide $d = 2a$.

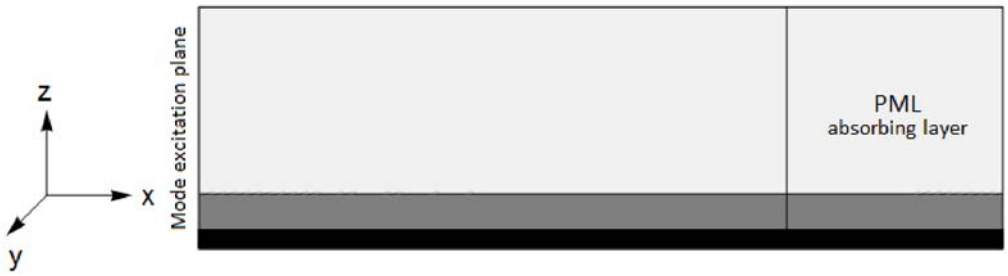

Figure 3.6: Slab waveguide simulation geometry consisting of a field-excitation at the input port (left) and a Perfectly Matched Layer (PML) to absorb the field at the right. We see the complete cover layer (dark and light gray) and the guiding layer (black) with differential mesh sizes, dense in the waveguide and coarser outside the waveguide.

To verify the accuracy of the propagation vector β as predicted by the dispersion relation, we excite magnetic fields profiles (3.54) at frequencies $f_0 = \frac{\omega}{2\pi}$ of $200THz$ and $1.80PHz$. The former only sustains one fundamental TM mode while the latter sustains more than three guided modes as illustrated in Fig. 3.5.

In subsection 3.3.3, we explain how inaccurate solutions of the dispersion relation split the incident profile decomposes into several other TM, TE or radiation modes. In other words, the incident profile is sensitive to *mode coupling*. Therefore, the numerical results are analyzed in three ways.

First, we apply a PEC condition to the upper boundary of the domain such that any radiation mode, which approaches this boundary unattenuated, is reflected. The resulting standing wave provides evidence for radiation modes and numerical inaccuracies. A second way to verify mode conservation, investigates reflections occurring during propagation. This results in intensity modulations which are detected by the Voltage Standing Wave Ratio (VSWR) associated to the magnetic field. Thus, the VSWR provides an estimation of the reflection induced by material inhomogeneities, mesh structures and boundary conditions (subsection 3.3.2). Third, we introduce the concept of modal decomposition as a way to measure how the total power P is redistributed among different guided modes with modal power P_m (3.28) during propagation. Perfect guided mode propagation preserves the modal power. Additionally, we verify the in-plane electric field is always parallel to the direction of propagation as is required for TM-modes. These TE-components arise from reflections when TM and TE modes couple (subsection 3.3.3).

3.3.1 Modal Field Profiles

Fig. 3.7 compares the numerically obtained electromagnetic fields to the theoretical predictions using the propagation vector and the frequency from the dispersion relation.

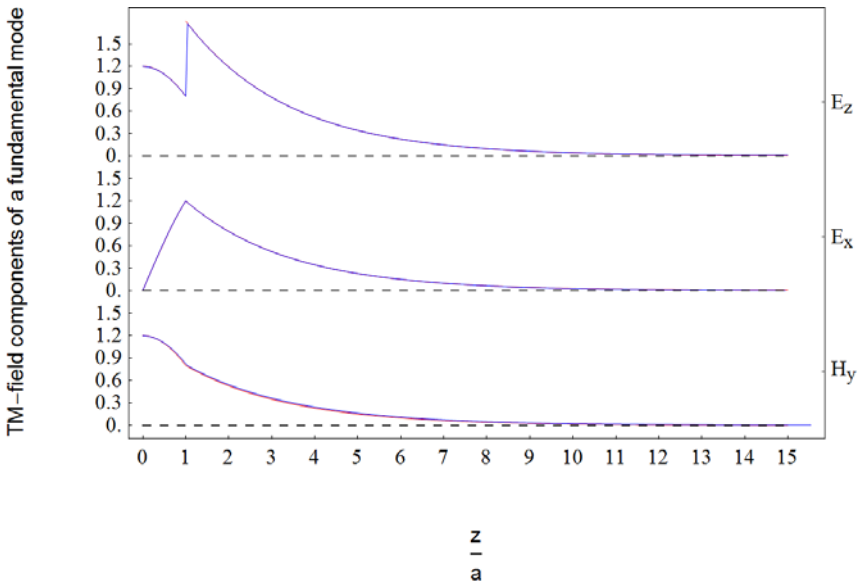

Figure 3.7: TM-fields of the fundamental mode $200THz$ below cut-off as a function of the orthogonal coordinate z for finite-element simulations (blue) and analytical predictions (red).

They are in excellent agreement. The exponential tails do not decouple into radiative modes, even at the logarithmic scale. Additionally, the fields E_y, H_x and H_z are zero, as expected for a TM polarization.

The higher-order modal solutions at $1.80PHz$ in Fig. 3.8 also agree with the analytical model. Because both odd and even magnetic fields are considered, the simulation domain comprises the complete transversal extent of the slab. The mode number is readily observed from the number of nodes in the guiding layer and confinement is much stronger than that of the modes in Fig. 3.7 at a lower frequency. At high frequencies, the internal reflections from the edges of the guiding layer induce additional interference effects, as is observed in the xz-plane images of Fig. 3.8. Enhanced confinement with increasing effective frequency $\tilde{\omega}$, i. e. increasing the frequency or slab thickness, is indeed a consequence of the dispersion curve moving away from the light cone of the cover/substrate (Fig. 3.3). It also implies higher-order modes are less confined than modes of lower order. The simulation in Fig. 3.8 also shows higher-order modes have increased effective wavelengths as the absorptive Perfectly Matched Layer (PML) on the right of the xz-plane attenuates the wave at larger distances.

3.3.2 Voltage Standing Wave Ratio (VSWR)

The Voltage Standing Wave Ratio (VSWR) is an important tool to estimate whether our transformation-optical waveguides induce reflections. We use two-dimensional simulations to calibrate guided mode propagation in an unperturbed guide.

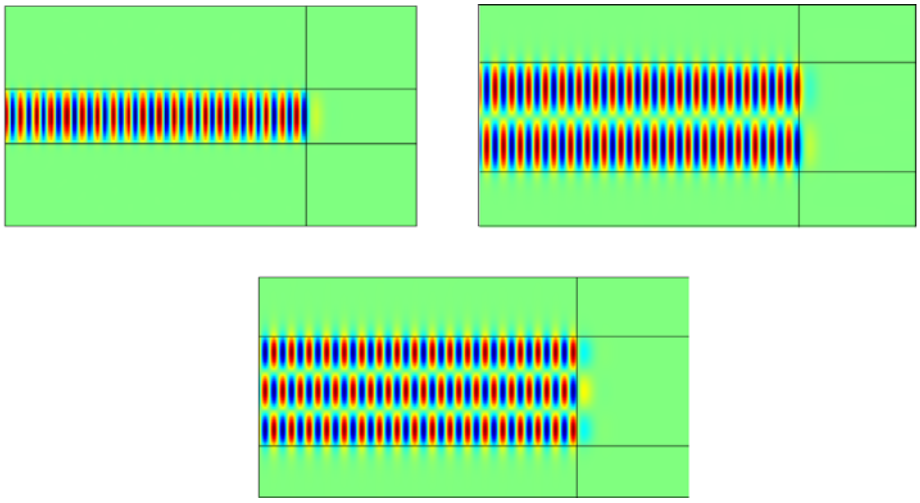

Figure 3.8: Finite-element simulations of magnetic field profiles in the xz-plane comprising the propagation direction and the normal to the slab at $1.80PHz$. The number of nodes identifies fundamental mode ($m = 0$ on the left), the first-order mode ($m = 1$ on the right) and the second-order mode ($m = 2$ in the middle).

Suppose the incident magnetic field

$$\mathbf{H}_{in} = H_{in}(x,z)\ \mathbf{e}_y,$$

is partially reflected due to material inhomogeneities, interfaces or mesh irregularities. We assume the reflected field

$$\begin{aligned}\mathbf{H}_r &= H_r(x,z)\ \mathbf{e}_y,\\ &= r\ e^{i\phi(x)} H_{in}(x,z)\ \mathbf{e}_y,\end{aligned}$$

preserves the TM polarization and is proportional to the incoming field. The reflection introduces a phase difference $\phi(x)$ and a reflection coefficient $r = \frac{|H_r|}{|H_{in}|}$. These approximations are valid for a single-mode guide if the coupling to the fundamental TE mode is weak.

Because of reflections, the magnetic field amplitude is modulated along the guide

$$|H_{in}(x,z) + H_r(x,z)| = |H_{in}|\ \sqrt{1 + r^2 + 2\ r\ \cos(\phi(x))}. \tag{3.55}$$

As is generally known [7], the VSWR

$$VSWR = \frac{H_{max}}{H_{min}} = \frac{1+r}{1-r}, \tag{3.56}$$

allows estimating the reflected power with respect to incoming power

$$\frac{P_r}{P_{in}} = \left(\frac{VSWR - 1}{VSWR + 1}\right)^2.$$

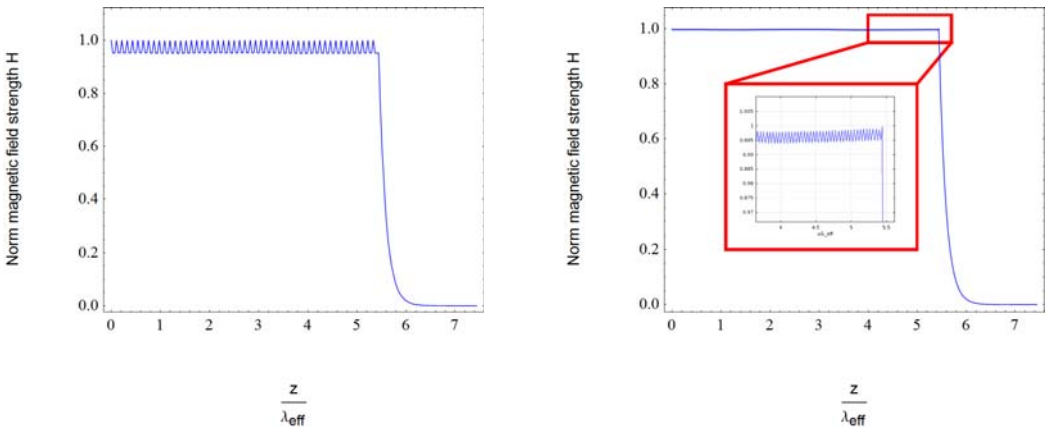

Figure 3.9: The VSWR for two different meshes, a quadrilateral (left) and a tetrahedral (right) mesh corresponding to reflection coefficients in Table 3.3. The amplitudes are strongly suppressed in the case of a tetrahedral mesh as shown by the inset.

Combining Eq. 3.55 and Eq.3.56 leads to the global reflection coefficient r of the perturbations

$$r = \frac{H_{max} - H_{min}}{H_{max} + H_{min}}. \tag{3.57}$$

An important contribution to reflections occurs due to limited resolution of the numerical simulations. Fig. 3.9 shows the norm of the total magnetic field—which allows determining the VSWR using Eq. 3.56—obtained by identical simulation domains with two different meshes, a quadrilateral and a tetrahedral mesh. Meshes consist of finite surface or volume elements covering the entire simulation domain. They are crucial to the finite-element technique which reduces continuous Maxwell equations to discrete equations through integration over each infinitesimal mesh element (Appendix C). Reflections occur either through coarse mesh subdivisions, which distort the VSWR with spiky jumps, or reflections from the PML in Fig. 3.6. The estimated reflections are small and decrease with the size of the coarsest mesh element (Table 3.3). Still, it is not possible to keep on reducing the mesh distortion because the solution time and required memory capacity increase exponentially for large three-dimensional simulations discussed in chapter 5.

For two-dimensional simulations, the computational concerns mentioned above are less stringent. It is possible to attain extremely fine mesh resolutions for which the VSWR loses its spikes and obtains a smooth sinusoidal behavior, as predicted by Eq. (3.55). For extremely fine meshes we only observe reflections due to the PML layer, which is 0.1%. Also, Fig. 3.9 provides a check on the efficiency of the PML absorbing layer, which attenuates the fields over four orders of magnitude in both simulations. Therefore, the parameters of the PML layers lead to sufficient performance to become part of our three-dimensional simulations.

Relative mesh resolution	Tetrahedral mesh	Quadrilateral mesh
Coarser (2X)	0.33%	2.4% (P)
Medium (1X)	0.20% (P)	1.6%
Finer (0.5X)	0.13%	0.7%

Table 3.3: Reflection coefficients r of unperturbed waveguides depending on the relative mesh resolution defined for each meshing algorithm separately. Reflections corresponding to Fig. 3.9 are indicated by (P).

3.3.3 Modal Decomposition and Coupling Efficiency

We now take another step to deepen our understanding of guided wave propagation along a slab waveguide. As mentioned in the introduction, guided modes

$$\mathbf{H}^{(m)}(x,z) = Z_H^{(m)}(z)\, e^{\mathrm{i}\beta^{(m)}x}\, \mathbf{e}_y,$$

provide an orthogonal basis to any initial transverse magnetic profile $\mathbf{H}(x=0,z)$ which is expanded using coefficients $\tilde{H}_m$. To be completely rigorous, one should also include the radiation modes with a continuous range of orthogonal propagation vectors k_z

$$H_{y\,in}(x=0,z) = \sum_{m=1}^{N} \tilde{H}_m\, Z_H^{(m)}(z) + \frac{1}{2\pi}\int_{-\infty}^{\infty} \tilde{H}(x=0,k_z)\, e^{\mathrm{i}k_z z}. \tag{3.58}$$

If the initial profile has a TE polarization, its electric field follows an analogous expansion

$$E_{y\,in}(x=0,z) = \sum_{m=1}^{N} \tilde{E}_m\, Z_E^{(m)}(z) + \frac{1}{2\pi}\int_{-\infty}^{\infty} \tilde{E}(x=0,k_z)\, e^{\mathrm{i}k_z z}. \tag{3.59}$$

To manipulate guided mode propagation, we will modify the permittivity and thickness of the guiding layer in an inhomogeneous way. Therefore, *the expansion coefficients $\tilde{H}_m$ and $\tilde{E}_m$ will be perturbed* during propagation and modes may exchange energy, even if they have opposite polarizations. The aim of this dissertation is, of course, to choose the appropriate variations which prohibit this mode coupling.

We generalize the expansions (3.58) and (3.59) to account for the evolution of an initial profile with arbitrary polarization and expand it with respect to TM and TE modes. It turns out the power flow still provides a means of constructing a generalized norm [8]

$$\begin{aligned} P &= \frac{1}{2}\,\mathrm{Re}\left[\int dy\, dz\ (\mathbf{E}\times\mathbf{H}^*)\ \cdot\ \beta\right], \\ &= \frac{1}{4}\quad \int dy\, dz\ [(\mathbf{E}\times\mathbf{H}^*) + (\mathbf{E}^*\times\mathbf{H})]\ \cdot\ \beta. \end{aligned} \tag{3.60}$$

The Poynting vector is integrated over both transversal coordinates y and z, although the y-coordinate only becomes important when including diffraction (section 3.4). In an unperturbed guide energy conservation guarantees every mode is mutually orthogonal to all other modes irrespective of the TE or TM signature [2]. They do not couple and the modal power is preserved. Additionally, only transversal field components contribute to the power flow because the longitudinal field components (Eq. (3.61)-(3.62)) are imaginary with respect to the other components. Thus, an arbitrarily polarized field with transversal components

$$\mathbf{E}_t = \sum_m \alpha_m \, \mathbf{E}_t^{(m)}(x=0,z),$$
$$\mathbf{H}_t = \sum_m \alpha_m \, \mathbf{H}_t^{(m)}(x=0,z),$$

is expanded with respect to transversal basis fields

$$\left(\mathbf{E}_t^{(m)}, \mathbf{H}_t^{(m)}\right),$$

corresponding to TM or TE modes. If the guided wave propagates along the x-direction, the transversal TM-fields become

$$\mathbf{H}_t^{(m)}(x,z) = Z_H^{(m)}(z)\, e^{i\beta^{(m)}x}\, \mathbf{e}_y \; ; \quad \mathbf{E}_t^{(m)}(x,z) = \frac{-\beta}{\epsilon_0 \omega \epsilon(z)}\, H_y(x,z)\, \mathbf{e}_z, \tag{3.61}$$

while the transversal TE-fields are

$$\mathbf{H}_t^{(m)}(x,z) = \frac{\beta}{\mu_0 \omega}\, E_y(x,z)\, \mathbf{e}_z \; ; \quad \mathbf{E}_t^{(m)}(x,z) = Z_E^{(m)}(z)\, e^{i\beta^{(m)}x}\, \mathbf{e}_y. \tag{3.62}$$

We use a polarization-independent notation for the expansion coefficients α_m as they either belong to TM expansion modes, reducing to $\tilde{H}_m$, or TE expansion modes, reducing to $\tilde{E}_m$.

Using the power (3.60) as a norm to the unpolarized initial profile, the expansion coefficients are extracted

$$\alpha_m = \frac{\int dy\, dz \, \left[\left(\mathbf{E}_t \times \mathbf{H}_t^{*(m)}\right) + \left(\mathbf{E}_t^{*(m)} \times \mathbf{H}_t\right)\right] \cdot \beta}{\int dy\, dz \, \left[\left(\mathbf{E}_t^{*(m)} \times \mathbf{H}_t^{*(m)}\right) + \left(\mathbf{E}_t^{*(m)} \times \mathbf{H}^{(\mathbf{m})}{}_t\right)\right] \cdot \beta}. \tag{3.63}$$

In the end, these coefficients determine how much a mode m is present in the guided wave at a particular waveguide slice. We will use Eq. (3.63) to estimate the *efficiency* with which the initial TM fundamental mode is maintained by our tranformation-optical waveguide bend in chapter 5. Here, we validate Eq. (3.63) for the case of the unperturbed waveguide which supports a fundamental TM and TE mode. This is a final check of the accuracy of our two-dimensional simulations.

If the initial profile propagates along the x-axis, the fundamental TM and TE mode coefficients

$$H_0 = \frac{-1}{2} \frac{\int dy\, dz \left[H_y + \frac{\epsilon_0 \omega \epsilon(z)}{\beta} E_z\right] H_y^{*(0)}(z)}{\int dy\, dz\, |H_y^{*(0)}(z)|^2}, \tag{3.64}$$
$$E_0 = \frac{1}{2} \frac{\int dy\, dz \left[E_y + \frac{\mu_0 \omega}{\beta} H_z\right] E_y^{*(0)}(z)}{\int dy\, dz |E_y^{*(0)}(z)|^2},$$

rely respectively on the profiles $Z_H(z)$ and $Z_E(z)$ in Eq. (3.54).The contribution η of the fundamental TM or TE mode is respectively

$$\eta_{TM\to TM} = |H_0|^2 \; ; \quad \eta_{TM\to TE} = |E_0|^2. \tag{3.65}$$

Since we excite a TM mode at the entrance of the slab, $\eta_{TM\to TM}$ represents the propagation efficiency while $\eta_{TM\to TE}$ is the conversion efficiency. To obtain normalization-independent results, we define a *coupling efficiency* η^c as the ratio

$$\eta^c_{TM\to TM} = \frac{\eta^L_{TM\to TM}}{\eta^0_{TM\to TM}} \; ; \quad \eta^c_{TE\to TE} = \frac{\eta^L_{TE\to TE}}{\eta^0_{TM\to TM}}, \tag{3.66}$$

of the propagation efficiency after four effective wavelengths $L = 4\lambda_{eff}$ by the input efficiency close to the excitation plane $L = 0$

$$\eta^{\text{output}}_{TM\to TM} = 99.5\% \quad \eta^{\text{output}}_{TM\to TE} = 0.$$

Except for a numerical inconsistency of 0.5%, which may be related to numerical errors e.g., using a quadrilateral mesh, these coupling efficiencies confirm our simulations solved for pure TM modes.

To conclude this section, we mention how guided modes respond to small perturbations in a waveguide with small refractive index contrasts. In such a perturbed waveguide, it is still possible to define guided modes locally with slowly varying amplitudes. The corresponding coefficients α_m satisfy the following coupled mode equations [2]

$$\frac{d\alpha_m}{dz} = i\beta^{(m)}\alpha_m + \sum_{m\neq n} \alpha_n \frac{\langle H_y^{(n)} \partial_z H_y^{(m)} \rangle}{\langle H_y^{(m)} H_y^{(m)} \rangle}. \tag{3.67}$$

Therefore, mode coupling is highly reduced if the waveguide preserves its normal symmetry. Then, the partial derivative ∂_z with odd parity prevents coupling between modes of different parities. Second, the fundamental TM mode of a single-mode waveguide is quite robust as it only couples to radiation modes or the fundamental TE mode. In the remainder of this dissertation, we limit ourselves to single mode waveguides and pay attention to maintain the orthogonal symmetry of the guide, with symmetric thickness variations and permittivity profiles which only depend on in-plane coordinates.

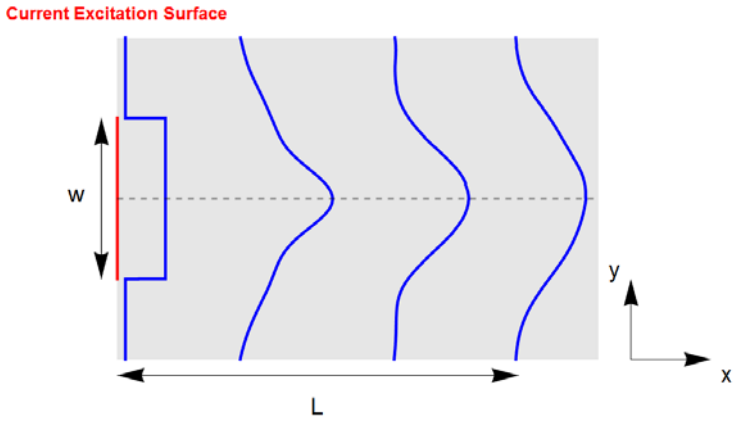

Figure 3.10: Numerically obtained diffracting guided waves as a consequence of truncation in the excitation plane.

3.4 Diffractive Guided Modes

In real-life applications, the inserted confined profile

$$H_y(x, y, z) = Z_H(z)\ \Phi(x, y), \tag{3.68}$$

consists of an orthogonal fundamental mode contribution $Z_H(z)$ and an in-plane xy dependence $\Phi(x, y)$ due to truncation or diffraction in the y-direction orthogonal to the propagation direction x. Fig. 3.10 illustrates these effects for a truncated plane wave of width w after a propagation length L. The effects of diffraction are estimated by the Fraunhofer diffraction angle Θ and the Fresnel factor N_F–which distinguishes near fields $N_F >> 1$ from far fields $N_F << 1$

$$N_F = \frac{\beta}{2}\frac{w^2}{L},$$
$$\Theta = \frac{\pi}{w\beta}.$$

This section has two objectives. First, we *extend the plane wave expansion technique* (Eq. (3.8)-(3.9)) to diffracting guided waves such that we are able to predict the VSWR of a diffracting beam. Due to energy spread, it is expected the VSWR deviates fundamentally from the planar dependence of eigenmodes which we obtained inFig. 3.9. Second, we corroborate our results with finite-element simulations of two initial profiles: a truncated plane wave of beam width w (Fig. 3.10)

$$\Phi_P(y) = \Pi\left(\frac{y}{w}\right), \tag{3.69}$$

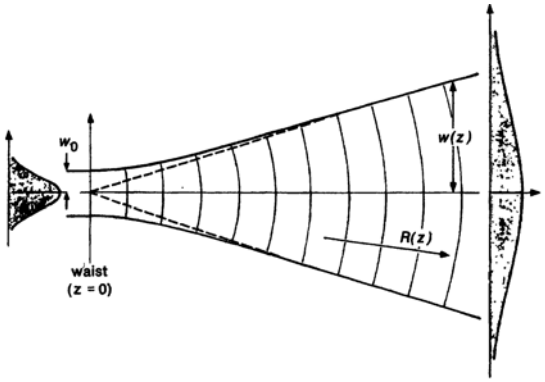

Figure 3.11: Geometrical parameters of a fundamental Gaussian profile: The curvature $R(x)$ and waist $w(x)$. Figure reproduced with permission from Ref. [9].

and a cylindrical Gauss-Hermite profile whose parameters—beam waist $w(x)$, curvature $R(x)$ and Rayleigh range x_R—are explained by Fig. 3.11

$$\begin{aligned} \Phi_G(x,y) &= Y_0 \sqrt{\frac{w(0)}{w(x)}}\, e^{-\left(\frac{y}{w(x)}\right)^2} e^{\mathrm{i}\beta x + \mathrm{i}\frac{\beta y^2}{2R(x)} - \mathrm{i}\frac{1}{2}\arctan\left(\frac{x}{x_R}\right)} \\ \text{with} \quad w(x) &= w(0)\, \sqrt{1+\left(\frac{x}{x_R}\right)^2}, \\ R(x) &= x\, \left(1+\left(\frac{x}{x_R}\right)^2\right). \end{aligned} \tag{3.70}$$

Diffraction breaks translational symmetry in the y-direction. Therefore, the simulation domain is affected in three ways. First, the simulation domain is inherently three-dimensional. This increases computational demands. Second, the guide is completely surrounded by absorbing PML layers since waves now propagate both in the x- and the y-direction. Third, arbitrary initial profiles cannot rely on built-in excitation techniques provided by *Comsol*. We developed an excitation technique, relying on surface currents, although these currents pose additional constraints on the PML design (appendix C). In total, these simulations require intense computational power. As a result, compromises are made between increased resolution—number of mesh elements—and geometrical dimensions of the simulation domain—sufficiently long to observe diffraction and sufficiently wide to excite broad initial field profiles.

3.4.1 Plane Wave Expansion Technique

The study of gaussian beams, e.g. Gaussian-Hermite, Gaussian-Laguerre and Bessel beams is currently leading to fascinating applications in laser beam optics, optical tweezing, trapping of metallic and high refractive index particles, and diffractionless

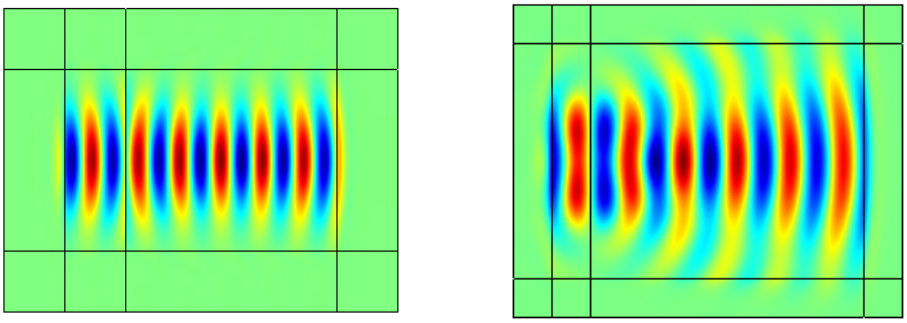

Figure 3.12: Frequency-domain finite-element simulations showing the in-plane magnetic field strength for a Gaussian-Hermite excitation of waist $w(0) = 7.5a = 3.75\mu m$ (left) and a truncated plane wave with beam width $w = 15a = 7.5\mu m$ (right). Both profiles are initially compressed and only spread after a limited distance.

propagation. All these beam profiles may be derived from a fundamental gaussian beam if appropriate differentiation operators act repeatedly on it [10]. Similarly to Eq. 3.9, we describe the in-plane profile $\Phi(x, y)$ of an arbitrary guided wave as follows

$$\Phi(x, y) = \frac{1}{2\pi} \int dk_y \, A(k_y) \, e^{\mathrm{i}\sqrt{\beta^2 - k_y^2}\,(x-l) + \mathrm{i}k_y y}. \tag{3.71}$$

Finite-element simulations in Fig. 3.12 illustrate this in-plane dependence of gaussian and truncated plane wave magnetic field strengths H_y. We don't consider the orthogonal dependence $Z_H(z)$ as it is fixed by boundary conditions and the in-plane propagation constant β. The location of the excitation surface $x = l$ provides an additional parameter which is optimized to the case of plane or gaussian waves respectively.

The angular spectrum $A(k_y)$ depends on the orthogonal in-plane wave vector k_y and is equal to the Fourier transform of the initial profile

$$A(l, k_y) = \int dy \, \Phi(l, y) \, e^{-ik_y y}. \tag{3.72}$$

Then, Eq. 3.71 readily provides the magnetic norm at the center of the beam ($y = 0$)

$$|\Phi(x, 0)| = \sqrt{\left\| \frac{1}{2\pi} \int dk_y \, A(k_y) \, e^{i\sqrt{\beta^2 - k_y^2}\,(x-l)} \right\|^2}, \tag{3.73}$$

which leads to the VSWR.

3.4.2 Truncated Planar Waves

Fig. 3.10 shows how our numerically predicted plane guided waves propagate after excitation at $l = 0$. The angular spectrum (Eq. 3.72) is a simple Fourier transform of a

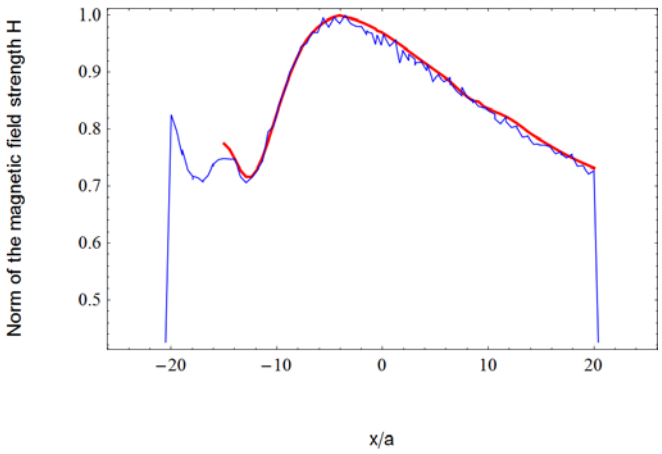

Figure 3.13: Comparison of the magnetic field strength norm determined by a tetrahedrally-meshed finite-element simulation and the numerical plane wave expansion method (left) and the corresponding plane diffraction pattern in the xy-plane (right). The beam width $15a = 3\mu m$ is expressed relative to the slab thickness $2a$.

Heaviside profile (Eq. 3.69)

$$A_P(k_y) = w \, \frac{\sin(\frac{k_y w}{2})}{\frac{k_y w}{2}}, \tag{3.74}$$

which is proportional to the familiar Sinc-function $\mathrm{Sinc}(x) = \frac{\sin(x)}{x}$.

Fig. 3.13 compares the numerical integral (Eq. (3.71)) of *Mathematica*, to the finite-element results for a tetrahedral mesh. Surprisingly, the dependence of the norm in Fig. 3.13 indicates a truncated plane wave initially compresses due to diffraction.The location of the field excitation plane at $l = -13a$ corresponds to a 'w'-shape of the magnetic norm at the center $y = 0$. After reaching a maximum at the plane of focus $x = -5a$, the energy spreads and the magnetic norm decreases again as expected. Therefore, a truncated plane wave acts as if it has a radius of curvature and a waist similar to a gaussian beam (3.70). This complex parameter imposes the same curved wave front as in the real representation. Analogously, the curvature of a plane wave is caused by imaginary contributions of $\sqrt{\beta^2 - k_y^2}$ in the plane wave expansion (3.71). This explains why the truncated plane wave is not completely focused.

For calibration purposes, we investigate the magnetic norm of a realistic quadrilateral mesh with reduced resolution. As seen in Fig. 3.14, the magnetic field strength norm clearly suffers from reflections despite optimization of the simulation domain was with thick PML layers and increased absorption strength. The oscillations have two scales, a fast scale corresponding to the limited mesh resolution discussed in subsection 3.3.2 and a slow scale. Slow scale variations result from the absorbing layers at the sides of the simulation domain, as these were not present in the two-dimensional simulations.

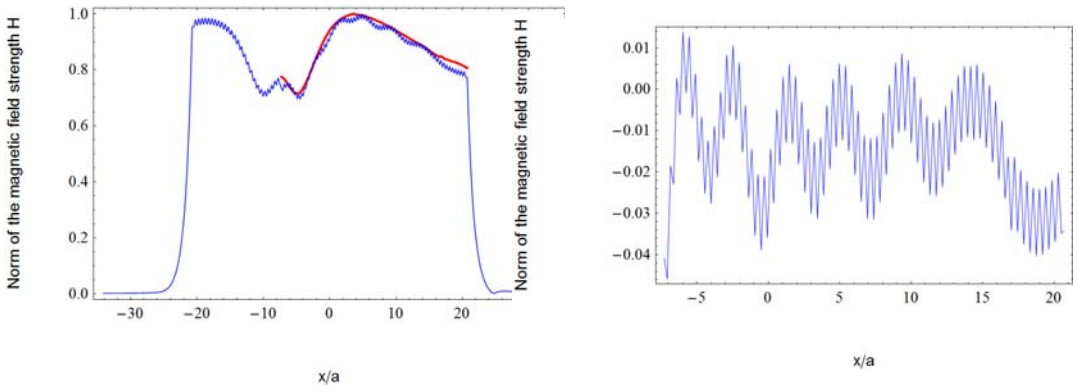

Figure 3.14: Comparison of the magnetic field strength norm determined by a quadrilaterally-meshed finite-element simulation and the numerical plane wave expansion method (left) and oscillations to the right of the excitation surface due to reflections after subtraction of the background (right). The beam width $15a = 3\mu m$ is expressed relative to the slab thickness $2a$.

Because the plane wave components enter at an oblique angle, which increases with the normal wave vector k_y, the built-in PML absorbing layers of *Comsol* cannot reduce reflections completely.

3.4.3 Gauss-Hermite Cylindrical Waves

The fundamental Gaussian beam Eq.(3.70) is a solution to the paraxial Helmholtz equation [9]

$$\left[2\mathrm{i}\beta\partial_x + \partial_y^2\right]\Phi_G(x,y) = 0,$$

which minimizes beam waist divergence in the spatial domain and the momentum spread due to diffraction in the reciprocal domain [10]. Again, we derive the angular spectrum using Eq. (3.72)

$$A_G(l,k_y) = \sqrt{\frac{\pi}{b(l)}}e^{-\frac{k_y^2}{4b(l)}}, \tag{3.75}$$
$$b(l) = \sqrt{\frac{1}{w(l)^2 + \mathrm{i}\frac{\beta}{2R(l)}}},$$

which is a gaussian profile with reciprocal beam waist $b(x)$. Since we want to limit diffraction throughout the simulation domain, we optimize the location of the excitation plane so that the coordinate of the zero-curvature plane coincides with the center of the propagation domain. Fig. 3.12 shows the point of zero curvature and minimal waist indeed occurs at a half the propagation distance L from the excitation surface, corresponding to the coordinate $x = 5a$.

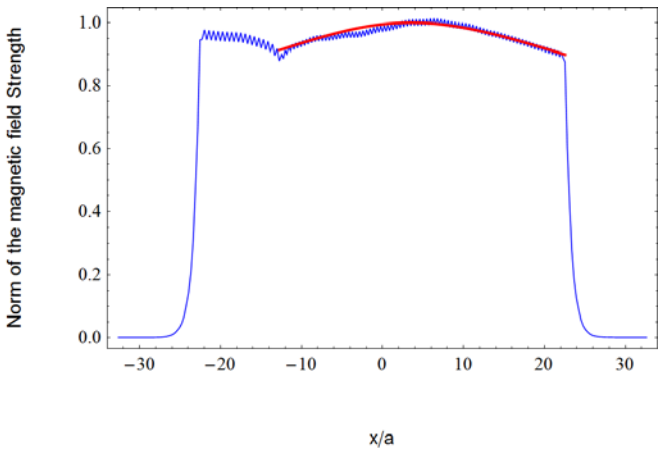

Figure 3.15: Comparison of the magnetic field strength norm determined by a finite-element simulation and the numerical plane wave expansion method. The beam waist is $7.5a = 1.5\mu m$ is expressed relative to the slab thickness $2a$.

Fig. 3.15 compares the result of the plane wave expansion to finite-element calculations with a quadrilateral mesh. As expected by the choice of the initially excited profile, diffraction initially focuses the wave and only spreads the energy after crossing a point of zero curvature at $x = 5a$.

3.5 Conclusion

In this chapter, we discussed general concepts related to the guided waves in slab waveguides. These concepts, e.g., beam diffraction, effective phase velocity and the voltage standing wave ratio, will play a crucial role to interpret the results in the subsequent chapters, where we introduce a two-dimensional extension of transformation optics to develop slab waveguides that transform the propagation of guided waves.

References

[1] P. Hertel, "Dielectric waveguides," *Lectures delivered at TEDA Applied Physics School, Nankai University, Tianjin, PRC* , 1–41, 2009.

[2] R. R. Syms and J. R. Cozens, *Optical Guided Waves and Devices*, McGraw-Hill, London, 1992.

[3] J. Hu and C. R. Menyuk, "Understanding leaky modes: Slab waveguide revisited," *Advances in Optics and Photonics* **1**, 58–106, 2009.

[4] S. H. Schot, "Eighty years of sommerfeld's radiation condition," *Historia Mathematica* **19**, 385–401, 1992.

[5] T. W. Ebbesen, C. Genet, and S. I. Bozhevalnyi, "Surface-plasmon circuitry," *Physics Today* **61**, 44–51, 2008.

[6] S. Zhang, D. A. Genov, C. Sun, and X. Zhang, "Cloaking of matter waves," *Physics Review Letters* **100**, 123002–123005, 2008.

[7] Z. D. Popović and B. D. Popović, *Introductory Electromagnetics*, Apprentice Hall, 2000.

[8] D. Marcuse, "Coupled-mode theory for anisotropic optical waveguides," *The Bell System Technical Journal* **54**, 985–995, 1975.

[9] A. E. Siegman, *Lasers*, University Science Books, 1986.

[10] F. Pampaloni and J. Enderlein, "Gaussian, hermite-gaussian, and laguerre-gaussian beams: A primer," *physics/0410021* , 1–29, 2004.

Chapter 4

Guided Transformation Optics

In this chapter, we develop a new kind of transformation optics, guided transformation optics, which modifies the wave propagation of fundamental TM modes along a slab waveguide. Since the waveguide problem is, on the one hand, a propagation problem described by an in-plane Helmholtz equation and, on the other hand, an eigenvalue problem determined by boundary conditions in the orthogonal direction, our newly developed approach deviates from traditional transformation optics in two ways. First, we use Helmholtz equations instead of Maxwell equations to establish equivalence relations. These relations map Helmholtz equations of physical space to Helmholtz equations of the device with electromagnetic material parameters ϵ^{ij} and μ^{ij}. Second, a traditional implementation of transformation optics modifies the cover and substrate layers of the waveguide. We provide a two-dimensional implementation which only modifies the material parameters inside the guiding layer. In this way, guided transformation optics does succeed in manipulating guided modes sustained by realistic, symmetric wave-guides with uniform cover and substrate layers.

4.1 Introduction

The formalism of guided transformation optics provides an alternative to three-dimensional transformation optics which allows for realistic manipulation of guided mode propagation along a slab waveguide. This introduction provides an overview of our newly developed analytical method which is further analyzed in the remainder of this chapter. Additionally, we provide an intuitive explanation of why a homogeneous waveguide bend is prone to decoupling and bending loss.

4.1.1 Guided Transformation Optics: an Overview

Fig. 4.1 illustrates two distinct stages when applying our new technique. As a first step, we use differential-geometric techniques to determine the *electromagnetic equivalence*

parameters of the waveguide. An incident fundamental TM mode along the y-direction

$$\mathbf{H} = Z_H^{(0)}(z)\, e^{\mathrm{i}\,\tilde{\beta}\,y}\, \mathbf{e}_x, \tag{4.1}$$

should preserve its fundamental characteristics, e.g. mode order and dispersion relation, when propagating in the transformation-optical device. Therefore, we ensure that the electromagnetic space contains a waveguide with identical properties, i.e. thickness $2\tilde{a}$, permittivity profile $\tilde{\epsilon}(z)$ and frequency ω, as the initial waveguide which guides the modes towards the device. Together with the fundamental mode dispersion relation (3.44), these wave-guide properties determine the initial propagation vector $\tilde{\beta}$ as a function of frequency ω.

As soon as the initial guided modes enter the device, they are manipulated by a finite-embedded, two-dimensional coordinate transformation

$$\begin{cases} x' &= X(x,y), \\ y' &= Y(x,y), \\ z' &= z, \end{cases} \tag{4.2}$$

which distinguishes an in-plane transformation $(X(x,y), Y(x,y))$ from an orthogonal trivial transformation z. This coordinate transformation transforms the fundamental initial guided mode in electromagnetic space to a guided mode in physical space with a Riemannian geometry.

To obtain novel electromagnetic equivalence relations, we use a different approach than that of traditional transformation optics. Instead of identifying Maxwell equations of the waveguide, we *identify the in-plane Helmholtz wave equations* of physical space

$$\Delta_{xy}\Phi_H(x,y) = -\left(\tilde{\beta}\right)^2\, \Phi_H(x,y), \tag{4.3}$$

to those of the device. Because the laplacians $\Delta(x,y)$ in physical space are determined by the coordinate tranformation and the Riemannian metric, these also determine our equivalence relations.

Because of the strict distinction between in-plane and out-of-plane transformations, we do not consider any orthogonal dependence on z to derive the Helmholtz equivalence relations. At this stage, a full implementation of material parameters *in each region of the waveguide*, i.e. the cover, the guiding layer and the substrate, is required to preserve the mode profile after transformation (upper right Fig. 4.1). We refer to this situation as 'full' transformation optics, as opposed to the partial implementation considered in the next stage of the design.

In the second step, we *limit the material parameters to the guiding layer only*. This partial implementation of transformation optics introduces boundary conditions to the problem. The thickness of the slab waveguide becomes another important transformation-optical parameter as it tunes boundary conditions and the dispersion relation of the

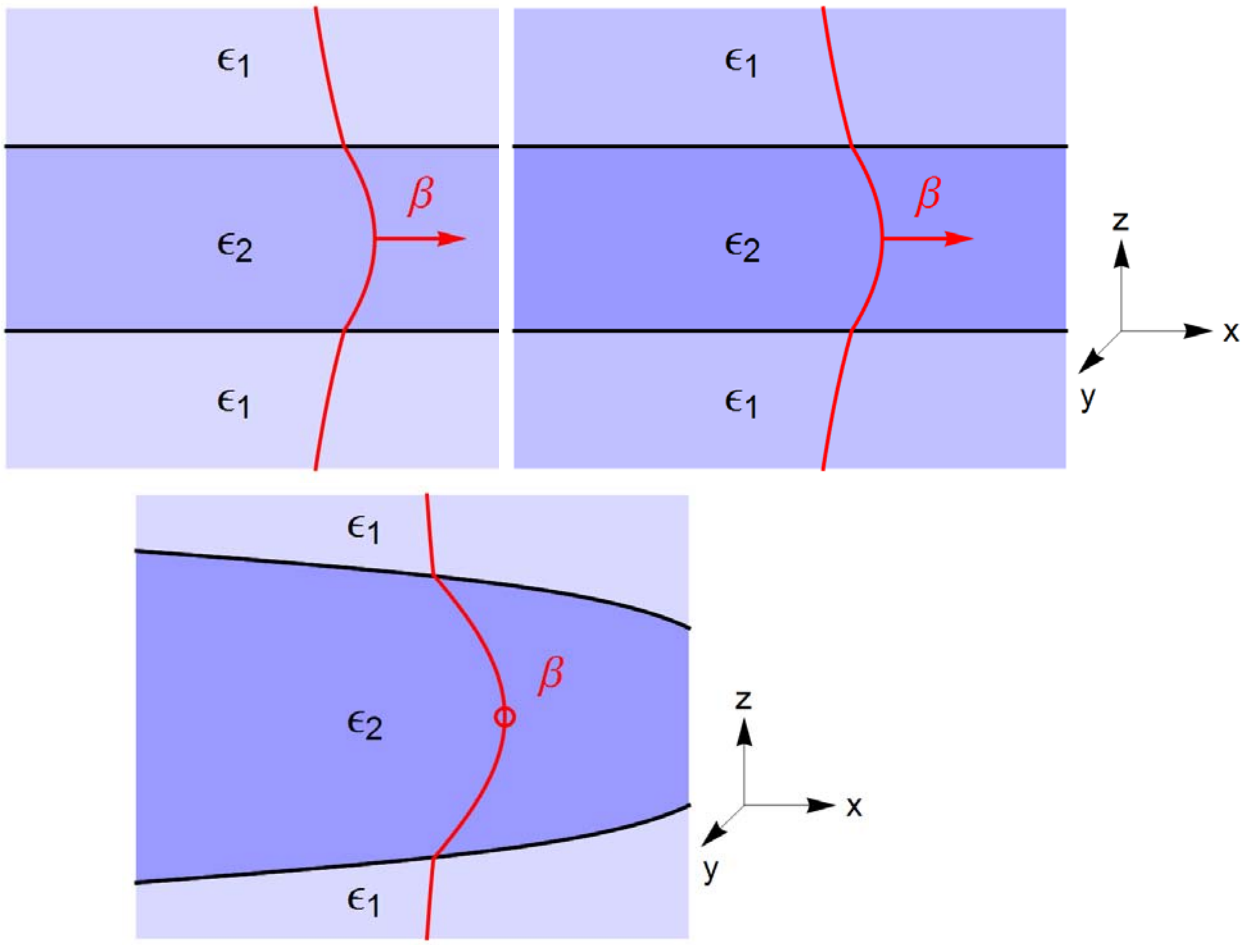

Figure 4.1: Two distinct stages in guided transformation-optical design. The electromagnetic space (upper left) consists of an unperturbed waveguide identical to that leading towards our device. First, this waveguide is transformed by a conformal coordinate transformation (upper right). Traditional 'full' transformation optics imposes the transformation with modified material parameters in both the cover, guiding and substrate layer (dark blue shades). Second, we use a thickness variation (lower) which imposes an identical dispersion relation as 'full' transformation optics while being compatible with vacuum cover and substrate layers (light blue shades).

guided device

$$\begin{aligned} \tan(k_2 a) &= \frac{\epsilon_2}{\epsilon_1}\frac{k_1}{k_2}, \\ k_1 &= \sqrt{\beta(x,y)^2 - \epsilon_1\frac{\omega^2}{c^2}}, \\ k_2 &= \sqrt{\epsilon_2\frac{\omega^2}{c^2} - \beta(x,y)^2}. \end{aligned} \tag{4.4}$$

in such a way that the effective index of the guided mode (3.40)

$$n_{eff} = \frac{c\beta}{\omega},$$

is identical to that of a full transformation-optical implementation. Only then, it is possible to preserve the desired propagation properties which we know from three-dimensional transformation optics.

The separability of the two-dimensional coordinate transformation (4.2) has important consequences. Thanks to the transformation rule of the metric (B.12), the coordinate transformation leads to an in-plane induced metric γ_{ij} and an out-of-plane contribution $g_{zz} = 1$ with $i, j \in \{x, y\}$

$$g_{ij} = \begin{pmatrix} \gamma_{ij} & 0 \\ 0 & 1 \end{pmatrix}. \tag{4.5}$$

It also transfers separable fields in electromagnetic space

$$\mathbf{H}(x', y', z') = \begin{pmatrix} \Phi(x', y')\ Z_H(z') \\ 0 \\ 0 \end{pmatrix}, \tag{4.6}$$

to separable solutions in physical space thanks to the covector transformation rule (B.7)

$$\mathbf{H}(x, y, z) = \begin{pmatrix} \left[\partial_x X(x,y)\ \Phi(x,y)\right]\ Z_H(z) \\ \left[\partial_y X(x,y)\ \Phi(x,y)\right]\ Z_H(z) \\ 0 \end{pmatrix}. \tag{4.7}$$

This is particularly true for the incident plane wave (4.1) on the guided transformation-optical device.

To increase compatibility of the coordinate transformation with the slab waveguide, we exclusively use *conformal transformations* (subsection 2.2.2) which constrain the Jacobian $\Lambda_i^{i'} = \frac{\partial x^{i'}}{\partial x^i}$ in the following way

$$\partial_x X(x, y) = \partial_y Y(x, y), \tag{4.8}$$

$$\partial_x Y(x, y) = -\partial_x X(x, y). \tag{4.9}$$

These Cauchy-Riemann relations impose an isotropic, but inhomogeneous, induced metric γ_{ij} to the plane of the slab (B.12)

$$g_{ij} = \begin{pmatrix} \gamma(x,y) & 0 & 0 \\ 0 & \gamma(x,y) & 0 \\ 0 & 0 & 1 \end{pmatrix}. \tag{4.10}$$

The equivalence relations (2.19) yield uniaxial material parameters, which contain the profile $\tilde{\epsilon}(z)$ of the waveguide in electromagnetic space (Fig. 4.1)

$$\epsilon^{ij} = \begin{pmatrix} \tilde{\epsilon}(z) & 0 & 0 \\ 0 & \tilde{\epsilon}(z) & 0 \\ 0 & 0 & \gamma(x,y)\tilde{\epsilon}(z) \end{pmatrix} \quad \mu^{ij} = \begin{pmatrix} 1 & 0 & 0 \\ 0 & 1 & 0 \\ 0 & 0 & \gamma(x,y) \end{pmatrix}. \tag{4.11}$$

The advantages of conformal transformations are twofold. First, the coordinate transformation allows for *nonmagnetic* material parameters which otherwise require challenging metamaterial to implement (section 2.4). Because the normal magnetic field strength H_z vanishes (Eq.4.7), the magnetic contribution to the Maxwell equations (A.21)

$$\begin{aligned} B^i &= \mu^{ij} H_j, \\ &= \mu^{ix} H_x + \mu^{iy} H_y, \end{aligned}$$

does not contain the nontrivial uniaxial magnetic component μ^{zz} (Eq. (4.11)).

Second, another subtle advantage becomes clear when considering the boundary conditions of the transformation-optical medium

$$\begin{aligned} H_x \quad &\text{continuous} ; \quad E_x \propto \frac{1}{\epsilon^{xx}(z)} \partial_z H_y \quad \text{continuous}, \\ H_y \quad &\text{continuous} ; \quad E_y \propto \frac{1}{\epsilon^{yy}(z)} \partial_z H_y \quad \text{continuous}. \end{aligned}$$

Thanks to the in-plane symmetry of the relative permittivity ϵ^{ij} (Eq. (4.11))

$$\epsilon^{xx} = \tilde{\epsilon}(z) = \epsilon^{yy},$$

boundary conditions on the untransformed slab interfaces $z = \pm a$ are identical to those of the fundamental waveguide in electromagnetic space with permittivity profile $\tilde{\epsilon}(z)$ (Eq. (3.7)). Apparently, the conformal transformation and the boundary conditions are independent degrees of freedom which are tuned by our two-step approach to guided transformation optics. In particular, this separability leads to distinct in-plane (3.22) and modal (3.23) wave equations in physical space.

The extraordinary component of the permittivity $\epsilon^{zz} = \gamma(x,y)\,\tilde{\epsilon}(z)$ is exclusively responsible for modifying propagation. As a part of the in-plane Helmholtz equation, this permittivity component imposes an effective index of refraction to guided modes. In addition, fundamental TE modes are not aware of the normal permittivity component ϵ^{zz} as their electric field lies completely within the plane of the waveguide. *Only TM guided modes are amendable to guided transformation optics.* Because of these observations, we conclude that the conformal coordinate transformation is compatible with the geometry of the slab waveguide.

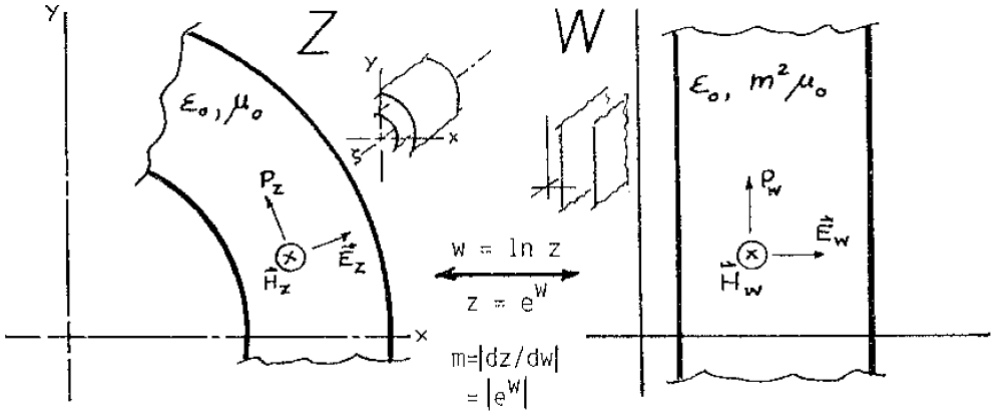

Figure 4.2: Simplification of wave propagation in a homogeneous beam bend. A conformal logarithmic map transforms the homogeneous bend to a straight waveguide with inhomogeneous electromagnetic material parameters to investigate bend properties with a simplified geometry. Figure reproduced with permission from Ref. [1].

4.1.2 Wave Equations and Transformation Optics

Before we derive the analytical motivations for the claims made so far, we put the manipulation of Helmholtz and other wave-equations into context. Even before transformation optics was conceived, conformal transformations were already used to simplify physical problems in several scientific fields such as aerodynamics (calculating lift of an airplane wings) fluid dynamics (manipulating the Navier-Stokes equation) acoustics (studying vibrating membranes with inhomogeneous boundaries) and electrostatics (reducing a capacitor with an inhomogeneous dielectric to a homogeneous capacitor of different width) [1].

We illustrate the power of conformal transformations by considering a homogeneous waveguide (Fig. 4.2) which is bent over an arbitrary angle. Because the waveguide bend breaks translation symmetry, its wave equations are difficult to solve. If we transform the coordinates x and y which describe the homogeneous bend with a conformal exponential map

$$\begin{cases} x &= \cos(v)\, e^u, \\ y &= \sin(v)\, e^u \end{cases}, \tag{4.12}$$

the geometry simplifies to a straight waveguide although the homogeneous medium is replaced by an inhomogeneous medium. Traditional three-dimensional transformation optics is now capable of calculating these new parameters and demonstrates why *a homogeneous waveguide bend does not perform well* for guided modes.

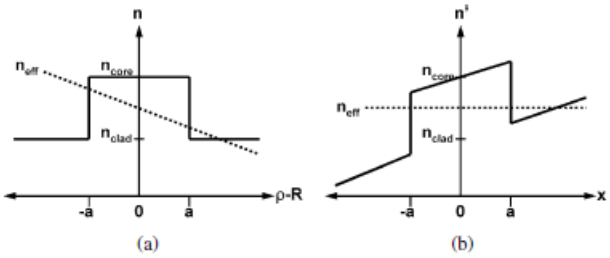

Figure 4.3: The effective index n_{eff} of a mode sustained by a homogeneous beam bend (left) compared to the effective index n'_{eff} of a straight beam bend with inhomogeneous refractive index profile n' (right). Figure reproduced with permission from Ref. [2]

According to the metric transformation rule (B.12), the geometry in electromagnetic space is equal to

$$g_{i'j'} = \Lambda^{i}_{i'}\Lambda^{j}_{j'}\delta_{ij}, \tag{4.13}$$

$$= \begin{pmatrix} e^{2u} & 0 & 0 \\ 0 & e^{2u} & 0 \\ 0 & 0 & 1 \end{pmatrix}, \tag{4.14}$$

and electromagnetic parameters follow from the equivalence relations (2.13) and (2.14)

$$\epsilon^{ij} = \begin{pmatrix} \tilde{\epsilon} & 0 & 0 \\ 0 & \tilde{\epsilon} & 0 \\ 0 & 0 & e^{2u}\tilde{\epsilon} \end{pmatrix}. \tag{4.15}$$

The modes propagating through a bent waveguide with refractive index n' correspond to the modes propagating through a straight waveguide of refractive index n

$$n' = ne^{u}, \tag{4.16}$$

$$\approx n(1+u), \tag{4.17}$$

where we assume the orthogonal coordinate u, which measures the separation of the interfaces, is small [2].

If we now apply the quantum well model which was established in subsection 3.2.4, we notice the depth of the potential well (3.49) is directly affected by the inhomogeneous refractive index

$$V_{eff}(u) \propto \omega^2_{eff}\,\tilde{\epsilon}\,2u, \tag{4.18}$$

such that light is more confined at the outer edge of the guide than on the inner edge.

The quantum model allows drawing two conclusions regarding the bending loss of a homogeneous waveguide. First, part of the electromagnetic energy at the inner boundary is converted to radiation modes due to weak confinement. At the inner boundary

the effective wavelength is close to that of vacuum so that tunneling is facilitated. Second, the V parameter (3.53) and cut-off effective potentials $V^{(m)}$ (Eq. (3.52)) increase with refractive index. Therefore, higher-order modes may be stripped from the guide during bending as mentioned in Ref. [3].

The aforementioned examples use *reverse engineering* to understand a fixed physical problem of physical space in terms of a simplified description in electromagnetic space. Transformation optics contributes to these developments in exactly the opposite way. Transformation optics makes use of new degrees of freedom provided by nano-structured media (subsection 2.4.1) to design previously unknown optical devices starting from simple electromagnetic spaces. Therefore, transformation optics changes the old question 'How can we understand a device with complicated structure with coordinate transformations' to 'How can we find a coordinate transformation which defines material parameters I want to implement'. The example of the beam bend is striking. Instead of modeling bend losses with conformal transformations and beam propagation methods (BPM) as in Ref. [2], an approach of transformation optics will actively search for materials which suppress such losses or eliminate them completely [3].

The importance of conformal transformations to several scientific fields, implies these fields somehow have the same mathematical foundation. Indeed, the physics of all these situations fundamentally relies on differential-geometric operators, such as Laplacians, divergences and rotors, within the wave equations. Therefore, derivations made in this chapter might be directly applicable to other physical problems.

Future contributions of transformation optics to fields outside of electromagnetism are expected to be relevant. In combination with ingenious techniques from material science, the operators within wave-equations are now amendable to design. Transformation optics currently extends its scope to other fields, e.g. cloaking applications in hydrodynamics [4] and quantum physics [5], and has already contributed to optimization of computing algorithms [6]. With these applications in mind, we explore the transformation properties of one particular differential-geometric operator, the Laplacian in Riemannian space-time.

4.2 Wave Equations in Spatial Geometries

In this section, we derive the covariant magnetic Helmholtz equation in physical space for an arbitrary geometry g_{ij}. We will apply these general wave equations to metrics which are generated by conformal transformations (Eq. (4.10)). These results are directly available for establishing the electromagnetic equivalence relations. For detailed derivations, we refer the reader to Appendix B.

4.2.1 A Covariant Wave Equation

The magnetic Helmholtz equation in physical space is derived from the generalized laws of Faraday (B.41) and Ampère (B.42) on a Riemannian geometry

$$\varepsilon_{ijk}\,\nabla^j E^k = \; i\omega\mu_0\, H_i, \tag{4.19}$$

$$\varepsilon^{ijk}\,\nabla_j H_k = -i\omega\epsilon_0\,\left(\tilde{\epsilon}(z)\; g^{ir} E_r\right), \tag{4.20}$$

with totally antisymmetric Levi-Civita tensors (Eq. (B.16) and Eq. (B.18))

$$\varepsilon^{ijk} = \frac{\pm 1}{\sqrt{g}}\,[ijk],$$
$$\varepsilon_{ijk} = \pm\;\sqrt{g}\,[ijk]\,.$$

As in Euclidean space, we apply a generalized rotor (B.38) to the law of Ampère (4.20) to decouple electric and magnetic fields in the Maxwell equations. Thanks to metric compatibility (B.31), which allows putting metric components out of the covariant derivatives, the left hand side of the law of Ampère (4.20) is equal to

$$\begin{aligned}[\nabla\times(\nabla\times\mathbf{H})]_i &= \epsilon_{ijk}\nabla^j\left(\epsilon^{klm}\nabla_l H_m\right),\\ &= \sum_{jklm}[ijk]\,[klm]\,\nabla^j\nabla_l H_m,\end{aligned} \tag{4.21}$$

while the right hand side is simplified with the law of Faraday (4.19)

$$\epsilon_0\;\tilde{\epsilon}(z)\;\partial_t\,[\nabla\times\mathbf{E}] = \frac{\tilde{\epsilon}(z)\omega^2}{c^2}H^i. \tag{4.22}$$

At this point, we derive the wave equations in the bulk of the material and ignore the boundaries, i. e. z-dependence of the permittivity profile. Combining Eq. (4.21) and Eq. (4.22), we obtain the magnetic wave equation on a Riemannian geometry

$$\nabla^l\nabla_l H_i - \nabla^l\nabla_i H_l + \frac{\tilde{\epsilon}(z)\omega^2}{c^2}.$$

The second term is further simplified by the commutation rule of covariant derivatives (B.36) and the magnetic Gauss law, i.e. $\nabla^l H_l = 0$

$$\nabla^l\nabla_l H_i - R_{il}H^l + \frac{\tilde{\epsilon}(z)\omega^2}{c^2}H_i = 0. \tag{4.23}$$

In this way, the Ricci curvature tensor R_{il} directly influences the wave equation. Since we consider a flat electromagnetic space, this term does not contribute

$$R_{il} = 0. \tag{4.24}$$

Wave equation (4.23) may be derived in a more elegant way which makes use of the Principle of Equivalence. Any Riemannian geometry g_{ij} becomes locally flat at a space-time point when described by normal coordinates. With respect to these coordinates, Eq. (4.23) simplifies to the wave equation in a flat, Euclidean geometry

$$\partial^l \partial_l H_i - \partial^l \partial_i H_l + \frac{\tilde{\epsilon}(z)\omega^2}{c^2} H_i = 0. \tag{4.25}$$

The general expression of the wave equation with respect to arbitrary coordinates, e. g., those we use to describe our physical space, are found by 'changing' partial derivatives ∂_i to covariant derivatives ∇_i. This is in agreement with the wave equation (Eq. (4.23)) we derived before from the Maxwell equations.

However, because partial derivatives commute in a flat space

$$\partial^l \partial_i = \partial_i \partial^l,$$

wave equation (4.25) is equivalently expressed in another way

$$\partial^l \partial_l H_i - \partial_i \partial^l H_l + \frac{\tilde{\epsilon}(z)\omega^2}{c^2} H_i = 0. \tag{4.26}$$

If the Principle of Equivalence were applied to this equation, it would lead to another covariant wave equation, different from Eq. (4.23) by a term containing the Ricci tensor (B.36). This inconsistency due to commutating partial derivatives is better known as curvature coupling [7]. It is resolved by postulating a fixed order of partial derivatives $\partial^l \partial_i$ such that Eq. (4.23) is indeed the correct extension of the Euclidean wave equation to a wave equation in Riemannian geometry.

4.2.2 A Flat Perspective

Generally, transformation-optical devices are designed so that their Maxwell equations in a flat Euclidean space ((2.5)-(2.8)) are identical to the Maxwell equations of a curved physical space ((2.9)-(2.12)). To achieve a reliable match, both Maxwell equations need to be expressed with respect to partial derivatives so that all contributions due to the metric are clearly visible.

Similarly, we need to rewrite the covariant wave equation on physical space (4.23) in such a way that it only contains partial derivatives. Since the Ricci tensor R_{ij} disappears for flat electromagnetic spaces, the only contribution of the Riemannian geometry to the wave equation arises due to the Laplacian Δ acting on the covector magnetic field strength $\mathbf{H}$

$$(\Delta \mathbf{H})_r = \nabla^l \nabla_l H_r.$$

In particular, the Christoffel symbols Γ^r_{ij} (B.32) include geometrical dependencies in the covariant derivatives of the Laplacian

$$\nabla_j H_i = \partial_j H_i - \Gamma^r_{ij} H_r, \tag{4.27}$$

$$\Gamma^i_{jk} = \frac{1}{2} g^{ir} \left[\partial_j g_{rk} + \partial_k g_{jr} - \partial_r g_{jk} \right]. \tag{4.28}$$

We use two approaches to establish the wave equation in terms of partial derivatives. First, we developed a computer code in *Mathematica* which calculates the dependence on geometry g_{ij} by brute force, inserting the Christoffel symbols into the Laplacian Δ. This program is also capable of calculating general Laplacians for arbitrary differentiable and invertible coordinate transformations on non-Euclidean geometries.

Second, we obtain an intuitive feel for the wave-equations when writing it in terms of partial derivatives. Section B.4 derives these wave equations in an analytical way for three distinct tensorial objects: a scalar $\phi(x^i)$, a vector field H^i an a covector field H_i. The scalar wave equation is most frequently used in (conformal) applications outside of transformation optics and has a Laplacian which is better known as the Laplace-Beltrami operator

$$\frac{1}{\sqrt{g}}\partial_j\Big(\sqrt{g}g^{jr}\partial_r\phi(x^i)\Big)+\frac{\tilde{\epsilon}(z)\omega^2}{c^2}\phi(x^i)=0. \tag{4.29}$$

The vector equations (B.58) are rather complicated for a general Riemannian metric. Still, they have been successfully applied to describe the propagation of wavepackets in a waveguide glued onto a sphere [8].

We will however formulate the equivalence relations based upon the *covector wave equations* in physical space (B.54)

$$\begin{aligned}&\sqrt{g}g^{jr}\partial_r\left(\frac{1}{\sqrt{g}}\partial_j H_i\right)-\sqrt{g}g^{jr}\partial_r\left(\frac{1}{\sqrt{g}}\partial_i H_j\right)\\ &-\sum_{j\,k\,s\,l\,m} g^{jr}\,[ijk]\,[slm]\,\Gamma^k_{rs}\,\partial_l H_m+\frac{\tilde{\epsilon}(z)\omega^2}{c^2}H_i=0,\end{aligned} \tag{4.30}$$

which consists of three coupled equations for $i\in\{x,y,z\}$.

4.2.3 A Conformal Wave Equation

Using a conformal induced metric (4.10), the wave equations in physical space (Eq. 4.30) simplify considerably. As expected, the conformal transformation treats in-plane magnetic field components in a similar way and yields x- and y-component wave equations which are of the same form. We express them in one equation with index $i,j\in\{x,y\}$ and $j\neq i$,

$$\frac{1}{\gamma(x,y)}\Big[\partial_x^2+\partial_y^2\Big]H_i+\frac{\partial_j\gamma(x,y)}{\gamma(x,y)^2}\Big[\partial_i H_j-\partial_j H_i\Big]+\frac{\partial_i\gamma(x,y)}{\gamma(x,y)}\partial_z H_z+\partial_z^2 H_i+\frac{\tilde{\epsilon}(z)\omega^2}{c^2}H_i=0.$$

On the other hand, the z-component is expected to behave fundamentally different

$$\frac{1}{\gamma(x,y)}\Big[\partial_x^2+\partial_y^2\Big]H_z+\partial_z^2 H_z+\frac{\tilde{\epsilon}(z)\omega^2}{c^2}H_z=0, \tag{4.31}$$

and remains independent from the coupled x- and y- wave equations due to the two-dimensional transformation (Eq. (4.2)). Because we consider transformed TM guided

modes of electromagnetic space (4.7) with no magnetic field orthogonal to the waveguide

$$H_z(x, y, z) = 0, \tag{4.32}$$

we can safely ignore the z-component wave equation (4.31).

The remaining wave equations seem quite complicated. Still, because they were obtained by a coordinate transformation acting on the Helmholtz equation in electromagnetic space, they carry some of its fundamental characteristics. For example, separable solutions which are consistent with the TM condition (Eq. (4.32)),

$$\mathbf{H} = \begin{pmatrix} \Phi_{H_x}(x, y) Z_{H_x}(z) \\ \Phi_{H_y}(x, y) Z_{H_y}(z) \\ 0 \end{pmatrix},$$

are still able to separate the wave equation into in-plane wave equations

$$\frac{1}{\gamma(x, y)} \left[\partial_x^2 + \partial_y^2\right] \Phi_{H_i} + \frac{\partial_j \gamma(x, y)}{\gamma(x, y)^2} \left[\partial_i \Phi_{H_j} - \partial_j \Phi_{H_i}\right] = -\left(\tilde{\beta}\right)^2 \tag{4.33}$$

and distinct modal wave equations which are *unaffected* by the transformation (4.2)

$$\partial_z^2 Z_{H_i}(z) + \left[\frac{\tilde{\epsilon}(z)\omega^2}{c^2} - \left(\tilde{\beta}\right)^2\right] Z_{H_i}(z) = 0. \tag{4.34}$$

We might go a step further and wonder how the full transformation-optical device in Fig. 4.1 manipulates initial plane guided modes (4.1). Similar to the example (2.27) in chapter 2, we may calculate the transformed magnetic fields using the covector transformation rule (B.7) and the Jacobian of the coordinate transformation (4.2)

$$\begin{aligned} \Phi_{H_x} &= \partial_x X \, \Phi(x, y), \\ \Phi_{H_y} &= -\partial_x Y \, \Phi(x, y), \\ Z_{H_x}(z) &= Z_H^{(0)}(z) = Z_{H_y}(z), \end{aligned}$$

with

$$\begin{aligned} \Phi(x, y) &= e^{i\tilde{\beta} y'(x,y)}, \\ &= e^{i\tilde{\beta} Y(x,y)}. \end{aligned} \tag{4.35}$$

Although the normal dependence of the fields $Z_H^{(0)}(z)$ is again not affected, the in-plane dependence of solutions (4.35) does change with respect to electromagnetic space. The fields obtain a spatially-dependent phase $\phi(x, y)$

$$\phi(x, y) = \tilde{\beta} \, Y(x, y), \tag{4.36}$$

which is proportional to the initial propagation vector $\tilde{\beta}$ of the mode, or equivalently, proportional to the propagation vector of the guided mode in electromagnetic space.

Within the ray approximation (A.30), this phase is related to the new, physical propagation vector of the transformation-optical medium

$$\begin{aligned}\boldsymbol{\beta} &= \nabla\phi(x,y),\\ &= \partial_x\phi(x,y)\ \mathbf{e}_x + \partial_y\phi(x,y)\ \mathbf{e}_y.\end{aligned} \tag{4.37}$$

Using the Cauchy-Riemann conditions of the conformal coordinate transformation (Eq. (4.9)) and the expression of the in-plane induced metric (Eq. (B.12))

$$\gamma(x,y) = (\partial_x X)^2 + (\partial_x Y)^2, \tag{4.38}$$

Eq. (4.37) leads to the magnitude β of the physically realized propagation constant inside the bend

$$\begin{aligned}\beta &= \tilde{\beta}\sqrt{(\partial_x X)^2 + (\partial_x Y)^2},\\ &= \tilde{\beta}\sqrt{\gamma(x,y)}.\end{aligned} \tag{4.39}$$

Thus, we confirm a coordinate transformation affects the propagation of a mode through changes in the effective index

$$n_{eff} = \sqrt{\gamma(x,y)}\ \tilde{n}_{eff}, \tag{4.40}$$

which depends on the induced metric $\gamma(x,y)$ in the ray approximation A.3.3.

To conclude this section, we verify if the transformed solutions indeed solve both wave equations (4.33) and (4.34). We already observed the normal z-dependence of a fundamental TM mode

$$Z_H^{(0)}(z) = \begin{cases} e^{-k_1 z} & z > a,\\ \cos(k_2 z) & |z| \le a,\\ e^{k_1 z} & z < -a \end{cases}, \tag{4.41}$$

and the modal wave equation (4.34) are both unaffected. The extinction coefficients (3.29), (3.30) and (3.31) depend however on the in-plane wave equation through the separation constant $\tilde{\beta}$

$$k_1^2 = \left(\tilde{\beta}\right)^2 - \frac{\tilde{\epsilon}_1\omega^2}{c^2}, \tag{4.42}$$

$$k_2^2 = \frac{\tilde{\epsilon}_2\omega^2}{c^2} - \left(\tilde{\beta}\right)^2. \tag{4.43}$$

Luckily, quantum numbers, such as the propagation constant $\tilde{\beta}$ corresponding to the energy of a particle-analogon in a quantum well (3.49), are conserved by full transformation optics as a consequence of the principle of covariance. Generally, this allows describing eigenstates of a complicated system with respect to transformed base functions of electromagnetic space, each associated to a conserved quantum number [9].

When the transformed solution (4.35) is inserted in the in-plane wave equation (4.33), we observe the separation constant of electromagnetic space $\tilde{\beta}$ is identical to that of the

wave equation in physical space. The logarithmic terms $\frac{\partial_j \gamma(x,y)}{\gamma(x,y)}$ cancel contributions from the Laplacian in such a way that the left-hand side is constant and equal to the right hand side $-\tilde{\beta}^2$. We come back to this observation in section 4.4 when we impose homogeneous media in the cover and substrate layer such that a magical cancellation is no longer possible.

In conclusion, full transformation optics changes the effective index of a guided mode without affecting the boundary conditions, the normal dependence of the fields—including the extinction coefficients k_i connected to the in-plane wave equation—and the normal wave equation. Because the orthogonal wave equations and field factors have no fundamental impact on the in-plane propagation, *traditional transformation optics is obliged to modify both the cover, guiding and substrate layer of a waveguide.*

4.3 Equivalence Relations

The equivalence relations of guided transformation optics are formulated in a two-step procedure described by Fig. 4.1. First, we map the in-plane Helmholtz equations between the physical space and an arbitrary electromagnetic medium to obtain the electromagnetic material parameters. Second, we consider how boundary conditions of a partial implementation deviate from the full transformation-optical design and compensate this with an additional parameter, the thickness of the slab $2a$.

4.3.1 Helmholtz Equations of an Arbitrary Electromagnetic Medium

To achieve the very same in-plane propagation with our transformation-optical device as in our designed Riemannian geometry, we look for electromagnetic parameters ϵ^{ij} and μ^{ij} which yield the very same in-plane wave equation (4.33) as that of physical space derived in the previous subsection

$$\frac{1}{\gamma(x,y)}\left[\partial_x^2+\partial_y^2\right]\Phi_{H_i}+\frac{\partial_j\gamma(x,y)}{\gamma(x,y)^2}\left[\partial_i\Phi_{H_j}-\partial_j\Phi_{H_i}\right]=-\left(\tilde{\beta}\right)^2. \tag{4.44}$$

The most general wave equation (A.28) corresponding to bi-anisotropic material parameters is derived in appendix A. It fully agrees with wave equations in literature for the case of an inhomogeneous isotropic material (subsection A.3.3). Instead of this bi-anisotropic medium, the conformal transformation suggests a uniaxial medium

$$\epsilon^{ij}=\begin{pmatrix}\tilde{\epsilon} & 0 & 0\\ 0 & \tilde{\epsilon} & 0\\ 0 & 0 & \epsilon_z\end{pmatrix};\quad \mu^{ij}=\begin{pmatrix}\tilde{\mu} & 0 & 0\\ 0 & \tilde{\mu} & 0\\ 0 & 0 & \mu_z\end{pmatrix},$$

which is most capable to mimick the physical space wave equation (4.44).

The *uniaxial wave equation* strictly distinguishes in-plane components H_i with $i \in \{x, y\}$

$$\left[\partial_x^2 + \partial_y^2\right] H_i + \frac{\epsilon_z}{\tilde{\epsilon}} \partial_z^2 H_i + \frac{\epsilon_z \tilde{\mu} \omega^2}{c^2} H_i + \frac{\partial_j \epsilon_z}{\epsilon_z} \left[\partial_i H_j - \partial_j H_i\right] = 0, \tag{4.45}$$

from the out-of-plane component z

$$\begin{aligned} &\left[\partial_x^2 + \partial_y^2\right] H_z + \mu_z \partial_z^2 H_z + \frac{\tilde{\epsilon} \mu_z \omega^2}{c^2} H_z \\ &+ \frac{\partial_x \tilde{\epsilon}}{\tilde{\epsilon}} \left[\partial_z H_x - \partial_x H_z\right] + \frac{\partial_y \tilde{\epsilon}}{\tilde{\epsilon}} \left[\partial_z H_y - \partial_y H_z\right] = 0. \end{aligned} \tag{4.46}$$

To impose a vanishing z-component of the magnetic field strength for TM modes, Eq. (4.46) implies the in-plane permittivity $\tilde{\epsilon}$ are independent of x and y.

We rewrite Eq. (4.45) such that variables x and y are separated from z. If we divide Eq. (4.45) by $\alpha = \frac{\epsilon_z}{\tilde{\epsilon}}$ and introduce a separability constant β, this leads to the in-plane uniaxial wave equation

$$\frac{1}{\alpha} \left[\partial_x^2 + \partial_y^2\right] H_i + \frac{\partial_j \alpha}{\alpha^2} \left[\partial_i H_j - \partial_j H_i\right] = -\beta^2 H_i,$$

and the modal uniaxial wave equation

$$\partial_z^2 H_i + \left[\frac{\tilde{\epsilon} \omega^2}{c^2} - \left(\tilde{\beta}\right)^2\right] H_i = 0. \tag{4.47}$$

In this form, we are able to compare the wave equation of the device (4.45) to that of physical space (4.44). Mapping is achieved if the in-plane permittivity $\tilde{\epsilon}$ is equal to the profile of the guide in electromagnetic space $\tilde{\epsilon}(z)$ and if the extraordinary parameter ϵ_z is linked to the conformal in-plane metric $\gamma(x, y)$

$$\begin{cases} \alpha &= \gamma(x, y), \\ \epsilon_z &= \gamma(x, y)\, \tilde{\epsilon}(z), \\ \tilde{\epsilon} &= \tilde{\epsilon}(z), \\ \tilde{\mu} &= 1. \end{cases} \tag{4.48}$$

We notice there is *no need for a magnetic material parameter*, as the TM mode eliminates the H_z component equation which couples to the extraordinary magnetic permeability μ_z.

4.3.2 Guided Transformation Optics

As a second step in Fig. 4.1, we implement the material parameters (4.48) in a partial way. Instead of manipulating the complete profile in electromagnetic space

$$\begin{cases} \tilde{\epsilon}_1 & z > a, \\ \tilde{\epsilon}_2 & |z| < a, \\ \tilde{\epsilon}_1 & z < -a, \end{cases}$$

so that the cover, guiding and substrate layer are uniaxial media as in Eq. (4.48), we retain the homogeneous and isotropic medium $\tilde{\epsilon}_1$ in the cover and substrate layer. We only use the nonmagnetic equivalence relations for the guiding layer

$$\epsilon_2^{ij} = \begin{pmatrix} \tilde{\epsilon}_2 & 0 & 0 \\ 0 & \tilde{\epsilon}_2 & 0 \\ 0 & 0 & \gamma(x,y)\,\tilde{\epsilon}_2 \end{pmatrix}. \tag{4.49}$$

Such a partial implementation should not prohibit some desirable characteristics which were realized by full transformation optics: the TM mode should be preserved by the device, i.e. $H_z = 0$, the effective index of the mode n_{eff} should contain an additional metric contribution with respect to the effective index of the incident guide $\tilde{n}_{eff}$

$$n_{eff} = \sqrt{\gamma(x,y)}\,\tilde{n}_{eff},$$

and the orthogonal dependence (4.41) should not be modified in a fundamental way. In this subsection, we will derive our results for a trivial constant isotropic rescaling X in the plane of the slab

$$\begin{cases} x' &= X\,x, \\ y' &= X\,y, \\ z' &= z, \end{cases} \tag{4.50}$$

which is the simplest implementation of a two-dimensional conformal transformation. In the following section, we motivate how the results of constant rescalings are extended to inhomogeneous coordinate transformations.

Because we consider a symmetric slab waveguide, all boundary effects are contained within one material interface, e.g., the cover-guiding layer interface at $z = a$. The in-plane wave equation in the cover layer—which is simply an untransformed Helmholtz equation—

$$\left[\partial_x^2 + \partial_y^2\right] H_i^{(1)} = -\beta_1^2 H_i^{(1)}, \tag{4.51}$$

and the wave equation in the guiding layer obtained from (4.45) and (4.48)

$$\frac{1}{\gamma(x,y)}\left[\partial_x^2 + \partial_y^2\right] H_i^{(2)} + \frac{\partial_j \gamma(x,y)}{\gamma(x,y)^2}\left[\partial_i H_j^{(2)} - \partial_j H_i^{(2)}\right] = -\beta_2^2 H_i^{(2)}, \tag{4.52}$$

are separated by their modal equations by two distinct separation variables, β_1 for the cover layer and β_2 for the guiding layer.

Two remarks are in order. Because we evaluate the performance of partial transformation optics at the level of the guided transformation-optical device—implemented by material parameters in a flat, Euclidean space—the metric components in these equations are simple scalar functions which are defined by Eq. (4.48). Additionally, we exploit the TM condition (4.32) and do not consider the z-component of the wave equations. The associated modal wave equations are identical to those of electromagnetic

space

$$\partial_z^2 H_i^{(1)} + \left[\frac{\tilde{\epsilon}_1 \omega^2}{c^2} - \beta_1^2\right] H_i^{(1)} = 0, \tag{4.53}$$

$$\partial_z^2 H_i^{(2)} + \left[\frac{\tilde{\epsilon}_2 \omega^2}{c^2} - \beta_2^2\right] H_i^{(2)} = 0. \tag{4.54}$$

We distinguish the fields in the cover $H^{(1)}(x, y, z)$ from those in the guiding layer $H^{(2)}(x, y, z)$ as they are solutions to distinct wave equations matched by boundary conditions at the interface $z = a$. In fact, due to the logarithmic terms $\frac{\partial_i \gamma(x,y)}{\gamma(x,y)^2}$ in the in-plane wave equation of the guiding layer, *it is impossible to find exact separable solutions*

$$\Phi_{H_i}^{(1)}(x, y) Z_{H_i}^{(1)}(x, y) \; ; \quad \Phi_{H_i}^{(2)}(x, y) Z_{H_i}^{(2)}(x, y),$$

to decouple the modal wave equation from the in-plane wave equation. If exact separability were possible and boundary conditions were completely taken into account by the orthogonal factor $Z_H(z)$, the continuity of the (in-plane) magnetic field strength would imply the fields in the cover and the guiding layer are identical up to a constant factor

$$\Phi^{(1)}(x, y) \propto \Phi^{(2)}(x, y).$$

Therefore, the Laplacians

$$\left[\partial_x^2 + \partial_y^2\right] H_i^{(1)} \propto \left[\partial_x^2 + \partial_y^2\right] H_i^{(2)},$$

are also proportional and constant. The metric term in Eq. (4.52) now introduces a spatial dependence to the separability constant β_2 such that exact separation of variables is violated. This is why we investigate the consequences of constant rescalings as an intermediate step to obtain consistent boundary conditions. Section 4.4 considers which conditions ensure approximately separable results for inhomogeneous conformal transformations.

We now consider a constant coordinate rescaling (4.50). The induced metric follows from the transformation rule (B.12)

$$\gamma_{ij} = \begin{pmatrix} X^2 & 0 \\ 0 & X^2 \end{pmatrix},$$

with $\gamma(x, y) = X^2$. The electromagnetic equivalence relation implies the guiding layer has a uniaxial permittivity (4.49) which is related both to the rescaling factor X and the incident guiding layer permittivity $\tilde{\epsilon}_2$

$$\epsilon^{ij} = \begin{pmatrix} \tilde{\epsilon}_2 & 0 & 0 \\ 0 & \tilde{\epsilon}_2 & 0 \\ 0 & 0 & X^2\, \tilde{\epsilon}_2 \end{pmatrix}.$$

The thickness of the waveguide now contributes to the guiding problem in the following way. If the problem is separable, the in-plane fields in the vacuum and the guiding layer are continuous at the interface

$$\Phi_{H_i}^{(1)}(x,y) = \Phi_{H_i}^{(2)}(x,y),$$

since the orthogonal dependence relies exclusively on separated $Z_{Hi}(z)$ factors. In addition, the Laplacian operators of the wave equations in the cover and the guiding layer simplify to

$$\left[\partial_x^2 + \partial_y^2\right] H_i^{(1)} = \beta_1^2 H^{(1)}, \tag{4.55}$$

$$\left[\partial_x^2 + \partial_y^2\right] H_i^{(2)} = X^2 \beta_2^2 H^{(2)}. \tag{4.56}$$

Because the guiding layer is implemented by a transformation-optical medium, we know the separation constant β_2 is equal to the propagation vector $\tilde{\beta}$ of the electromagnetic space $\tilde{\beta}$. To obtain a global effective index, the Laplacians (4.55) and (4.56) should match

$$\begin{aligned} \beta_1^2 &= X^2\, \beta_2^2 \\ &= X^2(\tilde{\beta})^2. \end{aligned} \tag{4.57}$$

In this way, the separation constant β_1 of the in-plane cover wave equation (4.55) is *identical to that of a guided mode which would exist in a 'full' transformation-optical waveguide* (Eq. (4.39)). The thickness variation compensates for the modified, homogeneous cover and substrate layer.

In a 'full' transformation-optical approach, light is only aware of the electromagnetic space. Therefore, a full transformation-optical device with modified parameters in the cover, guiding and substrate layer preserves the dispersion relation of the electromagnetic space $\tilde{\beta}(\omega)$. To achieve this with a partial implementation in the guiding layer only, we make use of a relative and symmetric thickness variation $a = A\tilde{a}$ which is illustrated in Fig. 4.1 with initial thickness $2\tilde{a}$ and relative thickness A.

The dispersion relation for our partial implementation is derived from the modal wave equations (4.47). As mentioned above, we assume the orthogonal dependence $Z_{H_i}(z)$ does not fundamentally change within the guiding device, i.e. it should still be possible to use the modal wave equations to define extinction coefficients

$$k_1^2 = \beta_1^2 - \frac{\tilde{\epsilon}_1 \omega^2}{c^2},$$

$$k_2^2 = \frac{\tilde{\epsilon}_2 \omega^2}{c^2} - \beta_2^2,$$

which are identical to Eq. (4.42) and Eq. (4.43), except for a difference in separation constants

$$\beta_1 = X\tilde{\beta}, \tag{4.58}$$

$$\beta_2 = \tilde{\beta}. \tag{4.59}$$

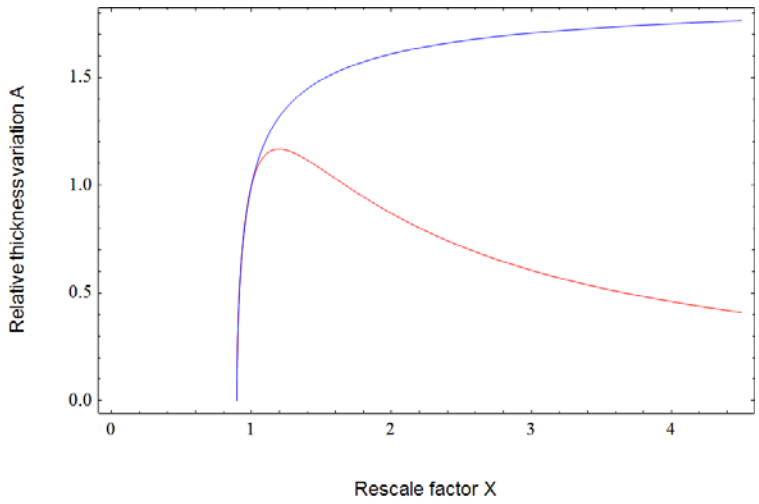

Figure 4.4: Equivalence relation for a geometrical parameter: Dependence of the relative slab thickness A on a rescale factor X for a uniaxial (blue) and an isotropic (red) implementation for an initial effective frequency $\omega_{eff} = 0.8378$ and propagation vector $\tilde{\beta}_{eff} = 0.9352$ corresponding to the numerical simulations in chapter 5.

A homogeneous rescaling maintains parallel interfaces $z = \pm a$ to the central plane of symmetry. It only requires one discrete jump from $z = \tilde{a}$ to $z = a$ at the entrance of the device. Combined with preservation of boundary conditions by uniaxial media, the dispersion relation (4.4) has the same appearance as for an untransformed slab waveguide

$$\tan(k_2 A\tilde{a}) = \frac{\tilde{\epsilon}_2}{\tilde{\epsilon}_1}\frac{k_1}{k_2}. \tag{4.60}$$

Inverting the tangens function, a relative thickness variation A as a function of constant rescaling X is obtained

$$A = \frac{1}{\sqrt{\tilde{\epsilon}_2\omega_{eff}^2 - (\tilde{\beta}_{eff})^2}}\ \mathrm{ArcTan}\left(\frac{\tilde{\epsilon}_2}{\tilde{\epsilon}_1}\frac{\sqrt{X^2(\tilde{\beta}_{eff})^2 - \tilde{\epsilon}_1\omega_{eff}^2}}{\sqrt{\tilde{\epsilon}_2\omega_{eff}^2 - (\tilde{\beta}_{eff})^2}}\right). \tag{4.61}$$

This is an additional equivalence relation of the guided transformation-optical device. Because we calculate the relative thickness with respect to the initial thickness $\tilde{a}$, Eq (4.61) contains effective dimensionless frequencies ω_{eff} and propagation vectors $\tilde{\beta}_{eff}$ which are completely determined by the initial wave.

Fig. 4.4 shows the analytical dependence of relative slab thickness on the rescaling factor X for two variations of guided transformation optics. The first variety comprises the *uniaxial electromagnetic equivalence relation* (4.48) discussed before. However, it is also possible to implement the guided device with an isotropic material if the TM condition $H_z = 0$ is slightly relaxed. Isotropic materials also map the H_x and H_y wave equations perfectly, but do not establish the TM condition $H_z = 0$ because they couple to the H_x

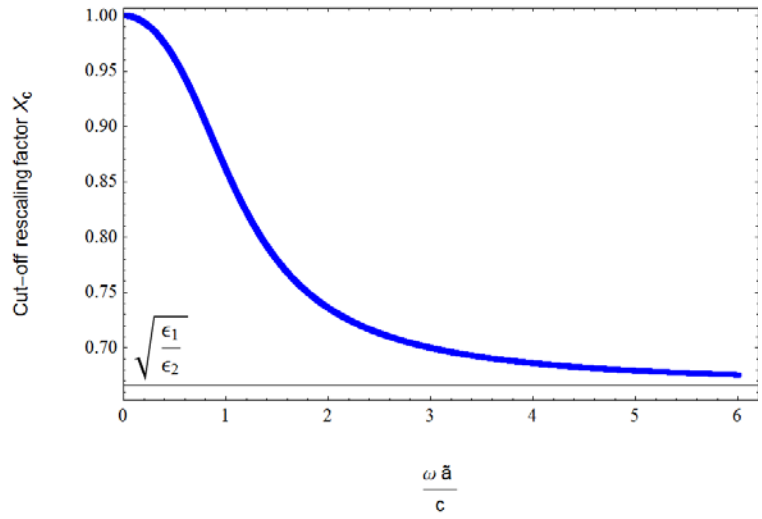

Figure 4.5: Cut-off constant rescale factor X_c as a function of the effective frequency at the entrance of the waveguide.

and H_y fields derived in the appendix (Eq. (A.29)). Only in the limit of thin slabs, when the fundamental mode inside the guiding layer has a small orthogonal derivative

$$\partial_z Z_{H_i}(z) \propto k_2 a \sin(k_2 a) << 1,$$

the guide realizes full transformation optical fields. We will briefly consider the performance of an isotropic beam bender in chapter 5. However, the uniaxial medium is more attractive because it is mathematically rigorous and implementable with hyperbolic metamaterials (subsection 2.4.1).

Clearly, not all rescalings X lead to guided devices which are capable of sustaining the initial fundamental mode. If the rescaling factor decreases, the extinction coefficients k_1 (4.58) becomes imaginary such that the modes radiate into the cover and substrate layer. Therefore, transformation-optical devices which require high phase velocities and low effective indices—e.g., the traditional cylindrical invisibility cloak of chapter 2—are not easily implemented by guided transformation optics because they require low rescalings.

The cut-off rescaling X_c occurs when k_1 reaches zero (Fig. 4.5)

$$X_c^2 = \frac{1}{\tilde{\beta}_{eff}^2}\, \tilde{\epsilon}_1 \omega_{eff}^2, \tag{4.62}$$

and is calculated in a numerical way depending on the effective initial frequency ω_{eff} and the associated propagation vector $\tilde{\beta}_{eff}$. According to our numerical solution in Fig. 4.5, there are two important regimes. At high frequencies and guiding layer thick-

ness, the threshold scaling factor X_c decreases until it saturates

$$X_c \overset{\omega_{eff}\to\infty}{\to} \sqrt{\frac{\tilde{\epsilon}_1}{\tilde{\epsilon}_2}}.$$

For low frequencies or low thicknesses, the threshold value X_c increases but never exceeds $X = 1$ which corresponds to an unperturbed waveguide manipulated by an identity transformation. Therefore, a constant rescaling does not impose a fundamental limit on the thickness of the waveguide in order to guarantee the guiding device works, i.e., all rescalings which increase the effective index are allowed. We will verify the behavior of a waveguide bend for various thicknesses in chapter 5.

These conclusions show that clever coordinate transformations, e.g., quasi-conformal transformations and non-Euclidean transformations would greatly enhance the scope of guided transformation optics as they are capable of reducing anisotropy (chapter 2). To implement conventional invisibility devices, which require high internal velocities $v = \frac{c}{n_{eff}}$ such that the inner cavity boundaries are crossed as if they are a point in electromagnetic space, highly confined incident modes on a thick and high-index guiding layer at high frequencies are required. This is however a multimode regime.

4.4 Guided transformation optics

In this section, we extend our results from constant rescalings (Eq. (4.50)) to inhomogeneous two-dimensional conformal transformations of Eq. (4.2). We illustrate our approach with the guided transformation-optical beam bend shown in Fig. 4.6. It implements an exponential map from electromagnetic coordinates (u, v, z') to physical coordinates (x, y, z)

$$\begin{cases} x &= \cos(\frac{v}{R})\, e^{\frac{u}{R}}, \\ y &= \sin(\frac{v}{R})\, e^{\frac{u}{R}}, \\ z &= z, \end{cases} \tag{4.63}$$

determined by a parameter R representing the outer radius of the beam bender in the guiding device. We have given the electromagnetic variables u, v, z' alternative labels to avoid notational confusion between $x^{i'}$ and x^i. Alternatively, this transformation could be inverted, such that each location in electromagnetic space (u, v, z') is described by physical coordinates (x, y, z)

$$\begin{cases} u &= R \ln\left(\sqrt{x^2 + y^2}\right), \\ v &= \mathrm{ArcTan}\left(\frac{y}{x}\right), \\ z' &= z, \end{cases} \tag{4.64}$$

and gives raise to an induced metric (B.12)

$$\gamma_{ij} = \frac{R^2}{x^2 + y^2}\, \delta_{ij}. \tag{4.65}$$

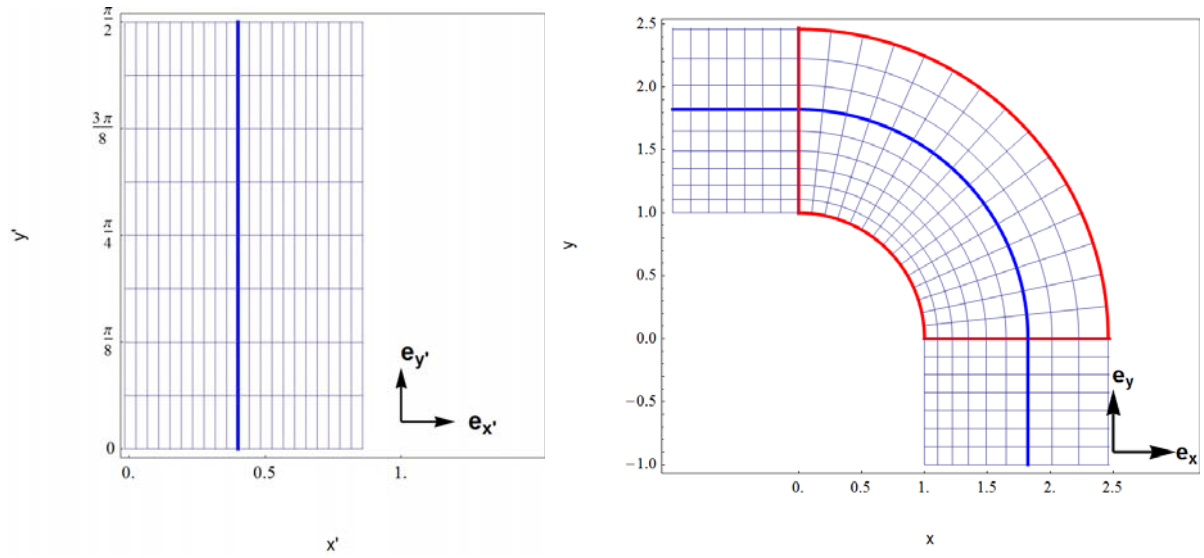

Figure 4.6: In-plane propagation of an incident plane guided mode on a finite-embedded conformal beam bend. The outer radius is equals the parameter R to achieve rescalings X which are larger than one.

Instead of discarding the logarithmic derivatives of the in-plane wave equations (4.52) which prevent separation of variables —this amounts to a ray approximation with scalar wave equations (A.3.3)—we consider how a plane wave inserted in the bender

$$H_x(x, y, z) = e^{i\tilde{\beta}\, y}\, Z_{H_x}(z)\, \mathbf{e}_x, \tag{4.66}$$

propagates under influence of a *linearized coordinate transformation* with respect to an arbitrary insertion point $\mathbf{P} = (x_0, y_0)$ in physical space. This will provide several intuitions about the conditions which are required to apply our guided transformation-optical approach.

Without any approximation, the magnetic field strength (Eq. (4.66)) has the following appearance in a full transformation-optical device

$$\begin{aligned}
\Phi_{H_x}(x, y) &= \Lambda^u_x\, \Phi(x', y'), \\
&= \gamma(x, y)\, \frac{x}{R}\, e^{i\tilde{\beta}\, \mathrm{ArcTan}\left(\frac{y}{x}\right)}, \\
\Phi_{H_y}(x, y) &= \Lambda^u_y\, \Phi(x', y'), \\
&= \gamma(x, y)\, \frac{y}{R}\, e^{i\tilde{\beta}\, \mathrm{ArcTan}\left(\frac{y}{x}\right)},
\end{aligned}$$

thanks to the covector transformation rule (B.7). As expected, orthogonal dependencies $Z_H(z)$ are not mentioned here because they are not affected by the coordinate transformation. The transformed solution identifies two length scales according to which the fields might deviate from those of a constant rescaling X

$$\Phi^X_{H_i(x,y)} = X\, e^{iX\, \tilde{\beta} x} \quad \text{for} \quad i \in \{x, y\}.$$

A first length scale is incorporated by the Jacobian which induces variations of the magnetic field strength amplitude

$$\mathbf{A}(x,y) = \begin{pmatrix} \gamma(x,y)\ \frac{x}{R} \\ \gamma(x,y)\ \frac{y}{R} \end{pmatrix}, \tag{4.67}$$

while a second contribution is due to the phase variations determined by coordinate line $u = Cst$ in electromagnetic space

$$\phi(x,y) = \tilde{\beta}\ \text{ArcTan}\left(\frac{y}{x}\right).$$

Then, the propagation vector $\boldsymbol{\beta} = \nabla\phi(x,y)$ provides a distance scale at which the phase changes significantly.

Because the plane modes in electromagnetic space do have homogeneous amplitudes and linear phases, the coordinate transformation should preserve these properties when expressing them in physical coordinates. We linearize the transformation at a point $\mathbf{P} = (x_0, y_0)$ in the following way

$$\begin{aligned} u(x,y) &= u(x_0,y_0) + \Lambda_x^u\big|_{\mathbf{P}}\ (x-x_0) + \Lambda_y^u\big|_{\mathbf{P}}(y-y_0), \\ v(x,y) &= v(x_0,y_0) + \Lambda_x^v\big|_{\mathbf{P}}\ (x-x_0) + \Lambda_y^v\big|_{\mathbf{P}}(y-y_0). \end{aligned}$$

The metric transformation rule (B.12) and Jacobian of the logarithmic map (4.67) readily provide the linearized metric $\gamma_{\mathbf{P}}(x,y)$ in physical space

$$\gamma_{\mathbf{P}}(x,y) = (\Lambda_x^u\big|_{(x_0,y_0)})^2 + (\Lambda_y^u\big|_{(x_0,y_0)})^2, \tag{4.68}$$

which is simply equal to the metric evaluated at $\mathbf{P}$

$$\gamma_{\mathbf{P}}(x,y) = \gamma(x_0,y_0).$$

If the Jacobian is only slightly spatially dependent so that a linearized transformation is a good approximation, the metric is approximately constant in a region surrounding any arbitrary point $\mathbf{P} = (x_0, y_0)$

$$\gamma_{\mathbf{P}}(x,y) \approx X^2,$$

for length scales which are inversely proportional to the largest component of the Jacobian or the magnitude of propagation vector $\boldsymbol{\beta}$. Then, thickness variations are also gradual and modest so that the boundary conditions of the unperturbed waveguide (Eq. (3.11)-(3.12)) also apply to the partially implemented waveguide. In those circumstances we define an relative thickness equivalence relation (4.61)

$$A = \frac{1}{\sqrt{\tilde{\epsilon}_2\omega_{eff}^2 - (\tilde{\beta}_{eff})^2}}\ \text{ArcTan}\left(\frac{\tilde{\epsilon}_2}{\tilde{\epsilon}_1}\ \frac{\sqrt{\gamma_{\mathbf{P}}(x_0,y_0)(\tilde{\beta}_{eff})^2 - \tilde{\epsilon}_1\omega_{eff}^2}}{\sqrt{\tilde{\epsilon}_2\omega_{eff}^2 - (\tilde{\beta}_{eff})^2}}\right), \tag{4.69}$$

in addition to the electromagnetic equivalence relation (Eq. (4.48)) derived before. *These are the two equivalence relations of our newly developed framework, guided transformation optics.*

Finally, we obtained several clues as to how our numerical simulations of a conformal beam bend will behave. The threshold on constant rescalings in Fig. 4.5 requires the radius of the beam bender r is smaller than the parameter R. However, to stay within the ray approximation at the level of the boundary conditions, we minimize the Jacobian (4.67) by staying close to the outer radius, i.e. $\gamma(x, y)$ is approximately equal to one. Increased beam width might deteriorate performance. Also, if the rescaling condition $X > 1$ is fulfilled, we do not expect the thickness of the guiding layer affects performance in a crucial way.

References

[1] R. Schinzinger and P. A. A. Laura, *Conformal Mapping: Methods and Applications*, Courier Dover Publications, 2012.

[2] R. Schermer and J. Cole, "Improved bend loss formula verified for optical fiber by simulation and experiment," *IEEE Journal of Quantum Electronics* **43**, 899–909, 2007.

[3] L. H. Gabrielli, D. Liu, S. G. Johnson, and M. Lipson, "On-chip transformation optics for multimode waveguide bends," *Nature Communications* **3**, 1217–1222, 2012.

[4] Y. Urzhumov and D. R. Smith, "Fluid flow control with transformation media," *Physical Review Letters* **107**, 074501–074504, 2011.

[5] S. Zhang, D. A. Genov, C. Sun, and X. Zhang, "Cloaking of matter waves," *Physical Review Letters* **100**, 123002–123005, 2008.

[6] A. J. Ward and J. Pendry, "Refraction and geometry in maxwell's equations," *Journal of Modern Optics* **43**, 773–793, 1996.

[7] C. W. Misner, K. S. Thorne, and J. A. Wheeler, *Gravitation*, W.H Freedman and Company, 1970.

[8] R. Bekenstein, J. Nemirovsky, I. Kaminer, and M. Segev, "Shape-preserving accelerating electromagnetic wave packets in curved space," *Physics Review X* **4**, 011038–011048, 2014.

[9] J. B. Pendry, A. Aubry, D. R. Smith, and S. A. Maier, "Transformation optics and subwavelength control of light," *Science* **337**, 549–552, 2012.

Chapter 5

A Beam Bend

We demonstrate the validity of guided transformation optics with *Comsol Multiphysics* finite-element simulations of a 30- and 45- degree beam bend in the frequency domain. Although a guided transformation-optical medium is only operational in slowly varying regimes (chapter 4), the bender performs excellently at both angles for various thicknesses of the guiding layer. To validate our results, we rely on three benchmarking techniques explained in chapter 3: Investigating the existence of radiation modes with the normal profile of magnetic and electric fields, looking for reflections in the VSWR and investigating mode conversion with maps of in-plane electric field distributions.

5.1

A Conformal Beam Bend

In this chapter, we demonstrate the performance of a guided transformation-optical beam bend (Fig. 5.1) whose properties are described by table 5.1. We mostly focus on 45-degree beam bends because large propagation distances allow investigating cumulative effects due to imperfections and approximations of the proposed equivalence relations. Technical details about the numerical techniques can be found in appendix C, while supplementary results, e.g., analysis of a 30-degree beam bend and a full transformation-optical concentrator of guided modes, are discussed within appendix D.

The simulation domain of a guided transformation-optical beam bend is intrinsically three-dimensional (Fig. 5.1). A fundamental TM plane guided mode is excited by a user-defined port at the leftmost side. Initially, the guided mode travels along an unperturbed waveguide with thickness $2\tilde{a}$ for one effective wavelength, until it reaches the guided transformation-optical medium. After a 30- or 45-degree bend, the guided mode is absorbed by a perfectly matched layer (PML).

We design the simulation domain, i.e., its boundary conditions (appendix C.2), in such a way that they are compatible with monochromatic plane wave propagation. Then, the numerical results can be directly compared to the analytical derivations of

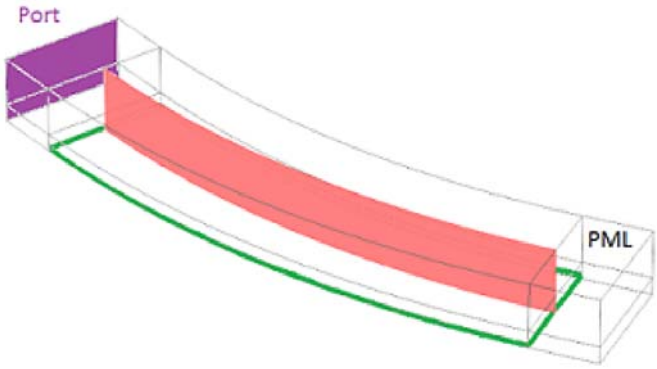

Figure 5.1: Simulation domain of a 30-degree beam bend without thickness variation. Along the orthogonal z-direction, there are three distinct layers. The wave-guiding layer of thickness $\tilde{a}$ is densely meshed (bottom, in green), an auxiliary vacuum layer of two decay lengths is used for intermediate meshing density (middle) and a top vacuum layer only requires a coarse mesh (top). An input port excites an eigenmode of unperturbed waveguide which is bent towards a perfectly matched layer (PML). We obtain our fields and VSWR from data points in the red plane, lying in the center of the beam.

chapter 4. Diffractive effects will not be considered here—although they have been investigated in the context of the concentrator (appendix D.2)—since they have no added value to verifying the guided transformation-optical parameters. Both traditional three-dimensional transformation optics and guided optics do not take diffraction into account when their equivalence relations are derived. Additionally, the description of obliquely incident guided modes in uniaxial materials on PMLs is highly nontrivial and requires an optimization of PMLs which falls outside the scope of this dissertation [1].

As explained in detail in section C.2, boundary conditions play a crucial role in translating physical guided wave propagation along an infinitely extended waveguide to a numerical simulation domain of finite extent. Because we solve for guided plane waves which propagate freely in two dimensions of the guiding layer, we need to truncate the domain in the guiding layer without confining the light in the direction orthogonal to the propagation. This is achieved by a Perfectly Magnetic Conductor (PMC) boundary condition on the radial boundaries of the domain.

A PMC boundary condition acts as a mirror to magnetic field components parallel to the boundary. Since Eq. (2.27) implies that the magnetic field of a TM mode only has a radial component, the initial plane guided modes indeed remain unaffected by the boundary. Similarly, we employ a Perfect Electric Boundary (PEC) condition in the symmetry plane $z = 0$, which takes advantage of the antisymmetry of the electric field to eliminate the lower half of the waveguide domain as explained in chapter 3 and appendix C.

Geometrical parameters	
Initial thickness $\tilde{a}$	0.2 μm
Max. relative thickness A_{max}	1.2448
Max. thickness $a_{\max}$	$0.249\mu m$
Outer radius R	$42\mu m = 33\ \lambda_{eff}$
Traveled distance d	$45°:\ 22\ \lambda_{eff}$
	$30°:\ 16\ \lambda_{eff}$
Material parameters	
$\tilde{\epsilon}_1$	1
$\tilde{\epsilon}_2$	$2.25 = (1.5)^2$
$\epsilon^{zz}_{\max}$	$2.868 = 1.275\ \tilde{\epsilon}_2$
$\epsilon^{zz}_{\min}$	$2.25 = \tilde{\epsilon}_2$
Initial guided mode	
ω_{eff}	0.838
β_{eff}	0.983
beam width w	$2.52\mu m = 24\ \tilde{a}$

Table 5.1: Simulation parameters of a 30- and 45-degree beam bend, implemented by guided transformation optics.

Before considering numerical results, we provide an overview of some relevant analytical predictions of chapter 4. The beam bender was designed by an exponential map (Eq. (4.64)), which leads to an uniaxial, radial permittivity profile

$$\epsilon^{ij} = \begin{pmatrix} \tilde{\epsilon}_2 & 0 & 0 \\ 0 & \tilde{\epsilon}_2 & 0 \\ 0 & 0 & \epsilon^{zz} = \frac{R^2}{x^2+y^2} \end{pmatrix}. \tag{5.1}$$

Fig. 5.2 provides an overview of both the electromagnetic and geometric equivalence relations of the beam bender. The anisotropy of the permittivity tensor increases for small radii r with respect to the outer boundary R. Light has to travel more slowly such that the plane wave fronts are preserved while turning. This behavior is exactly opposite to the permittivity profile of a uniform beam bend in Fig. 4.3. *Guided transformation optics thus compensates for bending losses as its electromagnetic space is a straight unperturbed waveguide.*

Additionally, a thickness variation (Eq. (4.69)) imposes that the phase velocity of the guided mode is globally defined and equal to that of a full transformation-optical

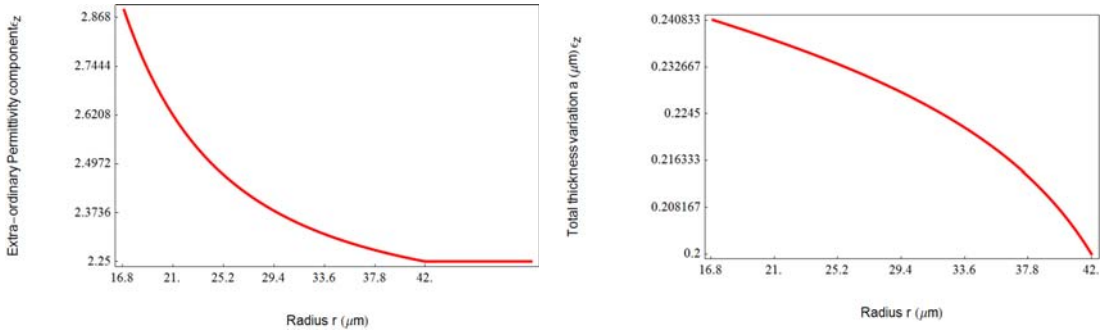

Figure 5.2: Guided transformation-optical parameters, the extraordinary permittivity ϵ^{zz} (left) and the absolute thickness variation a (right) with respect to the symmetry plane of the slab as a function of radius within the bend.

implementation

$$A = \frac{1}{\sqrt{\tilde{\epsilon}_2\omega_{eff}^2 - (\tilde{\beta}_{eff})^2}}\ \mathrm{ArcTan}\left(\frac{\tilde{\epsilon}_2}{\tilde{\epsilon}_1}\,\frac{\sqrt{\gamma(x,y)(\tilde{\beta}_{eff})^2 - \tilde{\epsilon}_1\omega_{eff}^2}}{\sqrt{\tilde{\epsilon}_2\omega_{eff}^2 - (\tilde{\beta}_{eff})^2}}\right). \tag{5.2}$$

To extract quantitative information about the coupling efficiency of the fundamental TM mode, we extend the analytical coupling efficiency of planar waveguides (3.64) to that of a beam bend of angle θ. The propagation vector $\boldsymbol{\beta}$ at the end of the bend is equal to

$$\boldsymbol{\beta} = \beta\left[\sin(\theta)\mathbf{e}_x - \cos(\theta)\mathbf{e}_y\right],$$

when the mode propagates along the negative y-axis as in Fig. 5.1. Therefore, the TM modal power coefficient H_0 and the TE modal power coefficient E_0 (Eq. (3.63)) depend on the bending angle

$$H_0 = \frac{1}{2}\,\frac{\int d\beta_\perp\, dz\, \left(\left[\sin(\theta)H_y + \cos(\theta)H_x\right] + \frac{\epsilon_0\omega\tilde{\epsilon}(z)}{\beta}E_z\right)\, H_x^{*(0)}(z)}{\int dz|H_x^{(0)}(z)|^2}, \tag{5.3}$$

$$E_0 = \frac{1}{2}\,\frac{\int d\beta_\perp\, dz\, \left(\left[\sin(\theta)E_y + \cos(\theta)E_x\right] + \frac{\epsilon_0\omega\tilde{\epsilon}(z)}{\beta}H_z\right)\, E_x^{*(0)}(z)}{\int dz|E_x^{(0)}(z)|^2}. \tag{5.4}$$

Integration is now performed in a direction $d\beta_\perp$ in the plane of the guide but orthogonal to the propagation vector.

Next to the basic simulation domain in Fig. 5.1, we introduce an extended simulation domain that contains both an additional piece of unperturbed waveguide at the exit of the bend and a specific kind of excitation port inside the domain (Fig. D.1). On the one hand, the additional piece of unperturbed waveguide allows estimating the throughput of an initial TM mode and sustains analytically known TM and TE eigenmode fields

Thickness	Scattering coefficient S_{11}
$0.21\mu m$	0.0595
$0.20\mu m$	0.0534
$0.17\mu m$	0.0303
$0.15\mu m$	0.0813

Table 5.2: Scattering coefficients on the input excitation port for a 30-degree beam bend for several initial thicknesses.

$H_i^{(0)}(z)$ and $E_i^{(0)}(z)$ which need to be inserted in Eq. (5.4). On the other hand, the domain-backed port automatically calculates the scattering coefficients between itself and other ports. In particular, the S_{11} coefficient estimates the amplitude of the reflected waves that reach the input port (table 5.2). These are mostly due to the initial waveguide/beam bender interface.

There are two reasons why we will not use Eq. (5.4) to estimate mode conversion inside the beam bend. First, the boundary conditions severely restrict the solutions solved for. In particular, the PEC condition at the symmetry plane prevents any sustained propagation of TE modes. Thus, TE modes appear as standing wave distortions in the simulation domain. This is illustrated for several thicknesses by Fig. D.4. Second, the waveguide/beam bender interface encourages energy transfer from TM to TE modes. It is therefore not possible to relate the effectiveness of our equivalence relations, i.e. reflectionless propagation within the bender, directly to the coupling efficiency at the exit.

Still, there is another efficient and qualitative means for determining whether TM modes are preserved during the bend. The covector transformation rule (B.7) implies that the radial electric field component should remain zero throughout the beam bend for a perfectly guided mode. Fig. 5.3 shows this is indeed the case for a full transformation-optical implementation. Thus, the ratio of the radial electric component with respect to the maximal electric norm—evaluated along the central arc in the plane of the slab $z = 0$ as shown in Fig. 5.1—provides a local measure of TM mode conversion.

Fig. 5.3 shows two important aspects of mode conversion in our guided transformation-optical beam bender. First, there exist small fluctuations of about 1% of the total electric norm. It is however not possible to pinpoint the exact cause of these fluctuations. They may arise from reflected radiation modes from the upper PEC boundary of the domain C.2 or from reflections within the guiding layer itself due to the combined effect of the thickness variation and the inhomogeneous permittivity. Either way, they are related to mode conversion. Second, Fig. 5.3 confirms the waveguide/beam bender interface

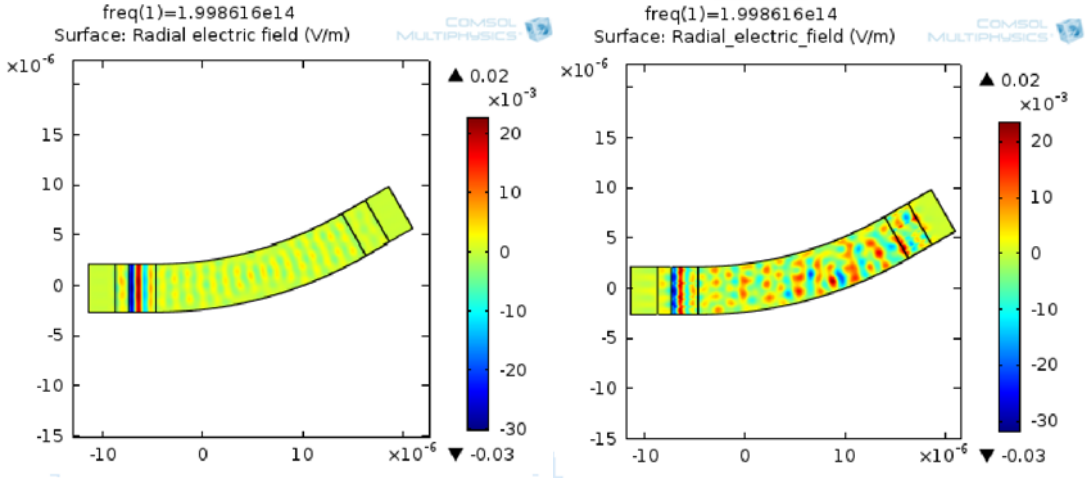

Figure 5.3: Relative radial electric field distribution in a full transformation-optical device (left) and a guided transformation-optical device (right) with specifications of table 5.1. The enhanced 'radial' components at the left side of the simulation domain are a result of the plotting function, which only maintains orthogonal fields to the propagation direction at the right side of the excitation port. The contribution of the initial guided mode to the TE mode is smaller than 0.1%.

generates TE polarized modes. A full transformation-optical implementation does not suffer from these conversions. This may be related to the fact that a full transformation-optical device imposes a global jump in permittivity without any variation in thickness. Then, both the evanescent tails and the oscillating fields inside the guiding layer are affected in a similar way.

In conclusion, we established two measures for reflections. Globally, the VSWR or the scattering coefficient of the domain-backed port C.3 provide quantitative estimates while, locally, we use the radial electric field distributions for qualitative results.

5.2 Evaluation of a Guided Beam Bend

5.2.1 Verification of the Thickness Equivalence Relation

To verify if the thickness variation (Eq. (5.2)) is a good transformation-optical parameter, we compare the performance of a full transformation-optical implementation—which affects permittivities in both the cover and the guiding layer but maintains a constant thickness—to our guided transformation-optical design—which only modifies the permittivity in the guiding layer, but uses a thickness variation. Fig. 5.4 illustrates how both implementations bend a guided mode over 45 degrees. An identical comparison

for a 30 degree bend Fig. D.2 is found in appendix D. Because the figures of this section span a full page, they are attached to the end of this chapter.

As shown in Fig. 5.4, the field distributions within the guiding layer are almost identical for full and guided transformation optics. If one increases the distance between the evaluation surface and the symmetry plane of the waveguide, however, both approaches increasingly differ. This is shown in Fig. 5.6. Within a traditional full transformation-optical device, the magnetic field strength distributions do not change fundamentally with orthogonal distance as this would imply a violation of separability. Only the amplitude decreases in an exponential way as the evaluation plane recedes from the symmetry plane of the guide.

In contrast, guided transformation optics respects separability in an approximate way for slowly varying thicknesses and amplitudes of the fields. Perturbations of separability are clearly visible as magnetic fields decay in an incoherent fashion when the distance with respect to the symmetry plane increases.

In addition to Fig. 5.4 which implies that the thickness variation is compatible with the beam bender design, Fig. 5.5 demonstrates that the thickness variation actually provides a necessary condition when a partial implementation of transformation optics is considered. The guided mode is only slightly affected by the medium and mostly travels in a straight trajectory until it encounters a TM or TE boundary conditions after which it suffers from reflections. The radial electric fields indeed show there is mode conversion from a TM to a TE polarization.

Still, the guided beam bend is very effective in a qualitative way and relies in a crucial way on the thickness variation. In the remainder of this section, we characterize the 30- and 45-degree beam bend to get a quantitative feel of the performance and reflections induced by the propagation. The measures which are thus obtained, should however be considered as an order of magnitude as they depend on mesh resolution which is intrinsically limited by our demand to use a direct solver which is capable to deal with advanced three-dimensional simulations.

5.2.2 Radial Magnetic and Electric Field Distributions

Fig. 5.7 and Fig. 5.8 compare the full transformation-optical magnetic and electric fields to those of guided transformation optics. Because of thickness variations, the orthogonal fields are not expected to be identical to those of full transformation optics as they induce spatially-varying extinction coefficients. Still, both fields should agree on exponentially decaying evanescent tails while the presence of radiation modes, i.e. standing waves between the upper and lower boundary of Fig. 5.1, should be avoided.

The magnetic field strength (Fig. 5.7) of the guided transformation-optical device does not satisfy the exponential decay law. This may be due to the particular numerical settings of this simulation, since several other simulations, for example Fig. D.5 for different initial thicknesses of the slab waveguide, do establish exponential decay.

Thickness	VSWR
$0.21\mu m$	0.0336
$0.20\mu m$	0.0533
$0.17\mu m$	0.0438
$0.15\mu m$	0.1269
45 degree	
Full TO	/
Guided TO	0.08333
30 degree	
Full TO	/
Guided TO	0.04084

Table 5.3: VSWR estimates of reflections due to the guided transformation-optical beam bend. Following the observations of Fig. 5.9 and Fig. D.8, fast-scale reflections are ignored as they appear also in the full transformation-optical device.

Fig. D.5 contains a numerical anomaly at the interface between the cover and guiding layer. The spikes may be caused by a limited mesh resolution, e.g., when mesh elements cross an abrupt material interface. However, in section C.4 we explain how we optimized the mesh to avoid such circumstances. Then, if the cause of the peaks is numerical, they should be linked to the limited mesh resolution, which cannot be reduced with a direct solver considering the computational capacity of our server.

The electric field (Fig. 5.8) of the guided transformation-optical device contains a low-amplitude standing wave which is consistent with the small nonzero in-plane electric field distributions discussed earlier (Fig. 5.3).

In conclusion, the magnetic and electric fields do deviate from the full transformation-optical device. The interface between the cover and substrate layer either induces non-exponential decay, as in Fig. D.5 or suffers from limited mesh resolution which creates spikes in the magnetic field strength amplitude. These observations are related to the incompatibility of boundary conditions with separable field solutions which are valid inside the guiding layer as discussed in section 4.3.2.

5.2.3 VSWR and Scattering Coefficients

The VSWR of the full transformation-optical device (Fig. 5.9) suggests only slow-scale variations are due to reflections induced by our guided transformation-optical bend. As in chapter 3, fast-scale fluctuations are related to a limited mesh resolution. Fol-

lowing Eq. (3.57), table 5.3 contains estimated reflection amplitudes for various initial thicknesses of the waveguide and for the 30-degree and 45-degree bend.

Generally, reflections are low, below 10% and decreasing, as the slab thickness increases. Indeed, if the thickness of the guiding layer increases, guided modes are increasingly confined so that the dielectric layer is increasingly effective in manipulating the mode. This is also confirmed by electric field distributions in Fig. D.6, which are more pronounced at lower slab thicknesses. However, as thickness increases above a certain threshold, higher-order modes become available such that fundamental TM mode propagation is adversely affected by mode coupling. To remain below the cut-off related to the odd TM mode, initial thicknesses should never exceed $0.21\mu m$ for the numerical parameters in Table 5.1. Additionally, Table 5.3 confirms bends of fixed radius and increasing angle induce more reflections.

References

[1] A. Oskooi and S. G. Johnson, "Distinguishing correct from incorrect pml proposals and a corrected unsplit pml for anisotropic, dispersive media," *Journal of Computational Physics* **230**, 2369–2377, 2011.

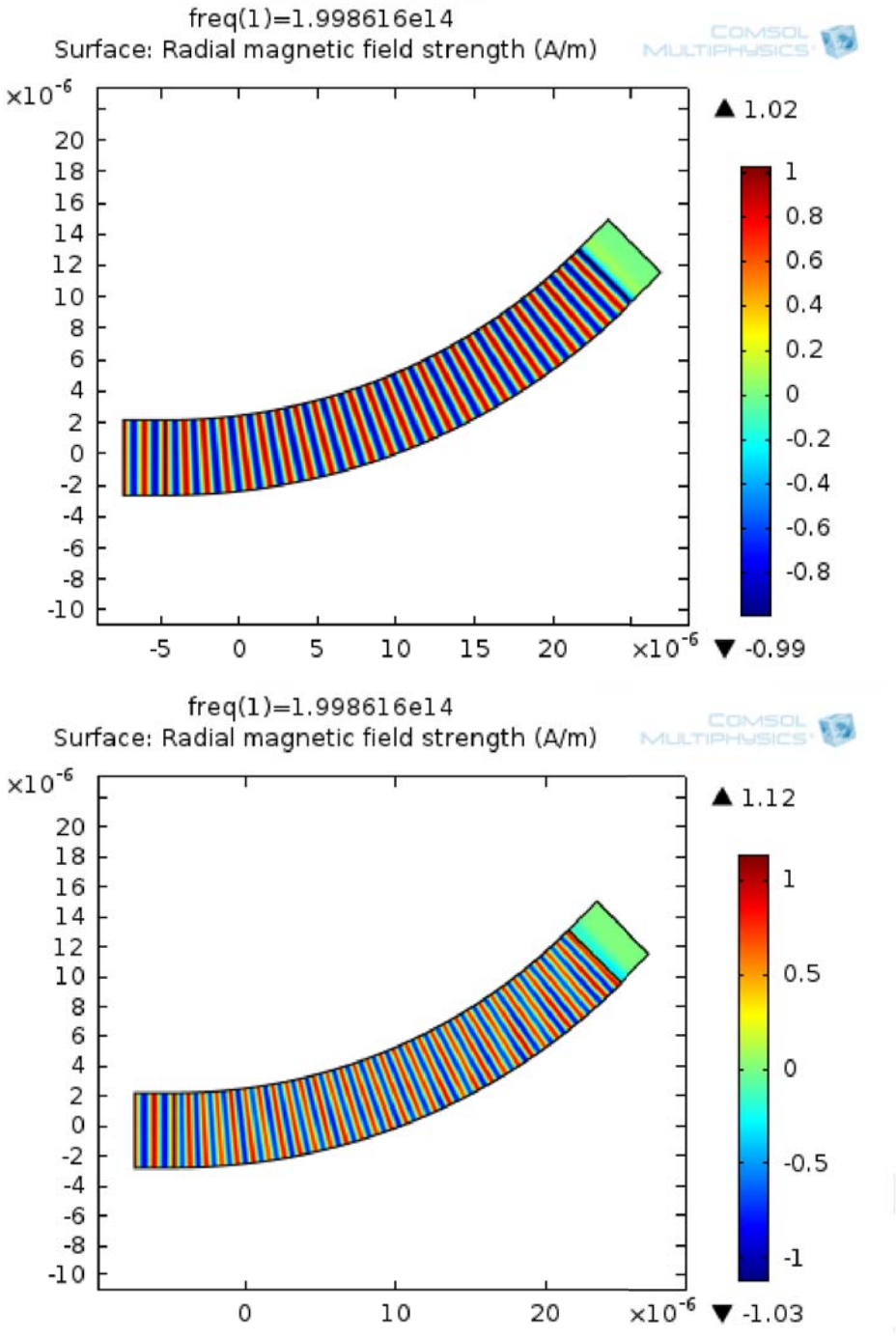

Figure 5.4: Verification of the thickness equivalence relation for a 45-degree beam bend. The in-plane propagation of an excited fundamental TM mode is compared for a full transformation-optical implementation (up) and a guided transformation-optical implementation with thickness variations in the guiding layer (down).

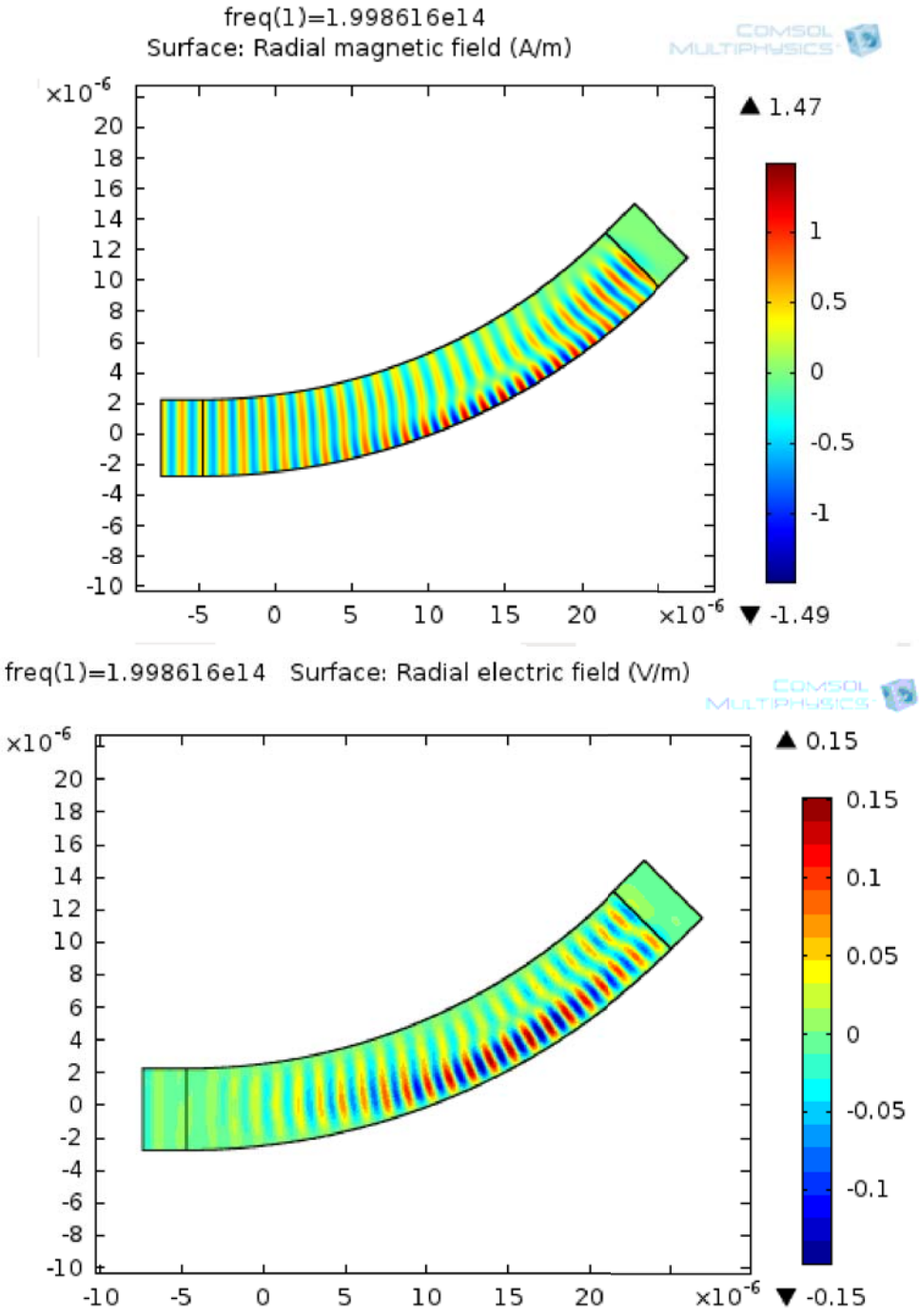

Figure 5.5: Radial magnetic fields (up) and radial electric fields (down) in the plane of the guiding layer with an inhomogeneous permittivity (5.1) but without a thickness variation.

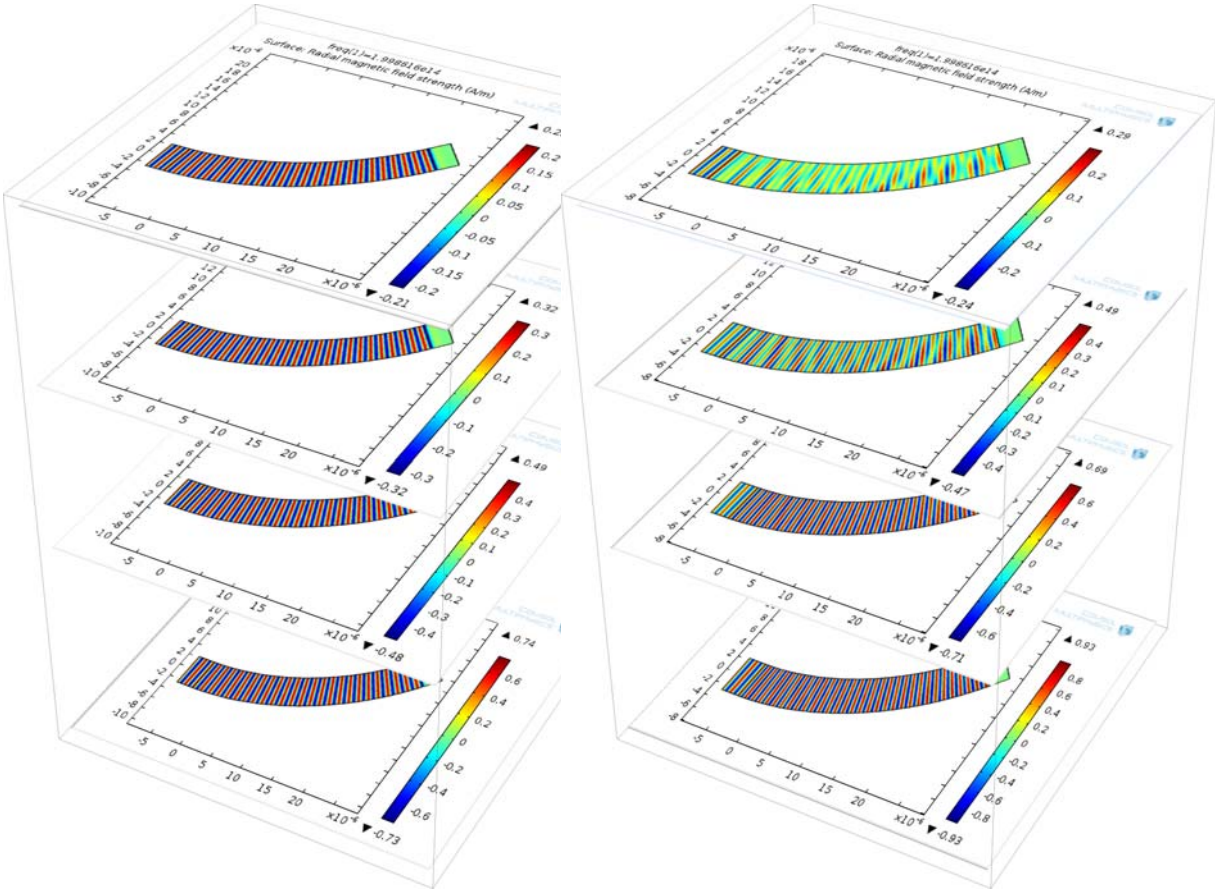

Figure 5.6: In-plane magnetic field strength distributions at distances $\tilde{a} = 0.2\mu m$, $2\tilde{a} = 0.4\mu m$, $3\tilde{a} = 0.6\mu m$ and $4\tilde{a} = 0.8\mu m$ from the plane of symmetry of the guide for a full transformation-optical implementation (left) and a guided transformation-optical implementation (right).

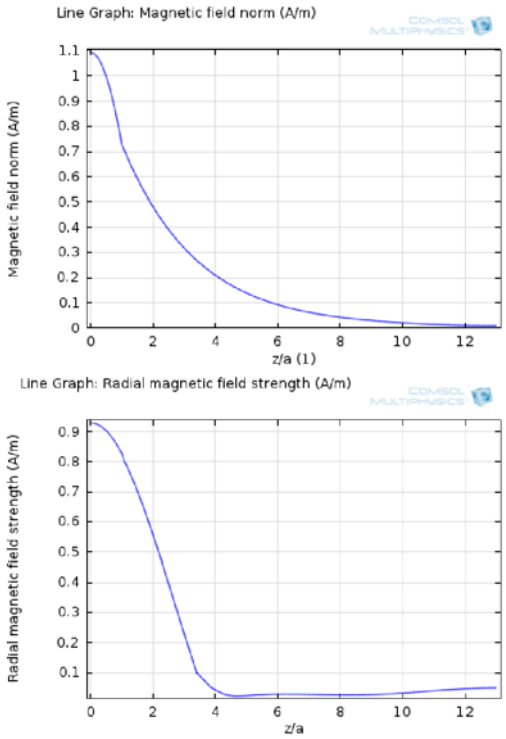

Figure 5.7: Orthogonal dependence of radial magnetic field strengths between a full transformation-optical implementation (up) and a guided transformation-optical implementation (down).

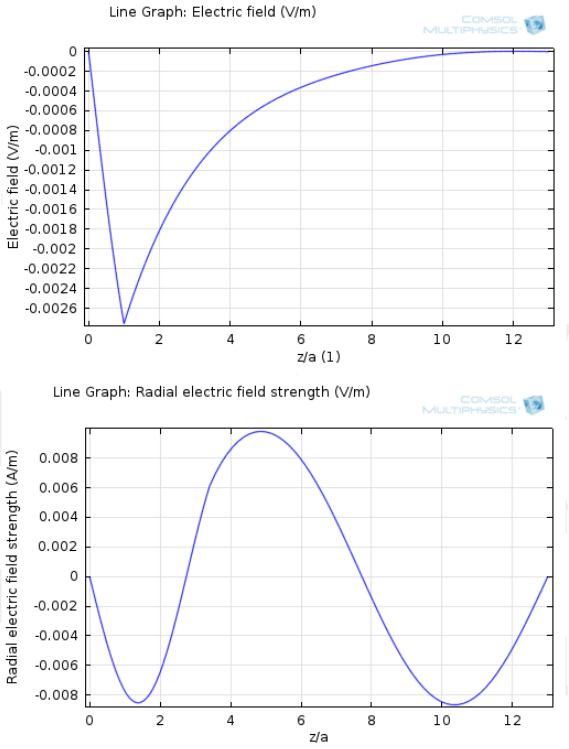

Figure 5.8: Orthogonal dependence of radial electric fields between a full transformation-optical implementation (up) and a guided transformation-optical implementation (down).

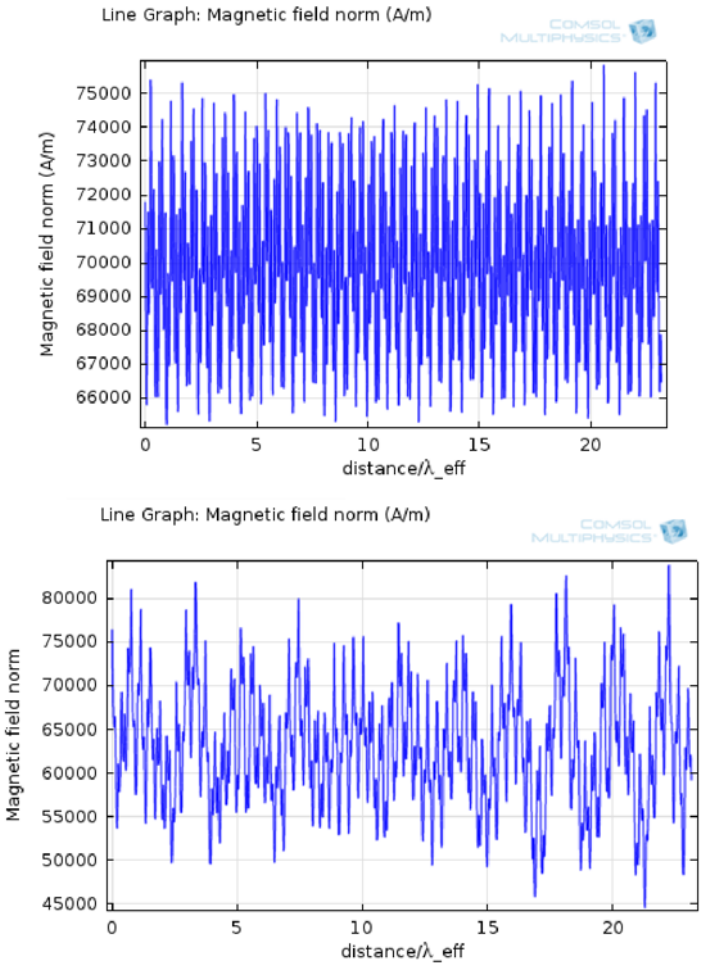

Figure 5.9: VSWR of a 45-degree beam bend for a full transformation-optical implementation (up) and a guided transformation-optical implementation (down). The (radial) magnetic field strength norm is evaluated long a circular arc which comprises the center of the beam and lies in the plane of the guiding layer (Fig. 5.1).

Chapter 6

Conclusion and Outlook

In this dissertation, we started from the observation that the traditional framework of transformation optics does not allow for the manipulation of confined electromagnetic waves along two-dimensional material sheets in a self-consistent way. Indeed, when applied to a nonmagnetic slab waveguide, transformation optics imposes nontrivial electromagnetic material parameters in the guiding layer of the waveguide as well as in the surrounding cover and substrate layers. Traditionally, transformation optics ignores the guiding/cover and guiding/substrate interfaces of the waveguide and alters material parameters without taking geometrical parameters, like the thickness of the waveguide, into account.

For this reason, we developed a new kind of transformation optics—guided transformation optics— which is compatible with guided waves confined to a nonmagnetic slab waveguide. To design the desired trajectories of a transverse magnetic mode supported by a guided transformation-optical device, we apply a two-dimensional conformal coordinate transformation, which only depends on the in-plane coordinates of the waveguide, to a traditional homogeneous waveguide. The straight trajectories of guided modes within the familiar waveguide are then deformed in such a way that they correspond to those required by the application.

To achieve the very same trajectories within our guided transformation-optical device as those of the coordinate-designed waveguide, we established *new equivalence relations, which relate the refractive index and the thickness of the guiding layer of the waveguide to the two-dimensional coordinate transformation*.

First, the equivalence relation that determines the refractive index was obtained in a novel way. Traditionally, three-dimensional transformation optics defines the material equivalence relations so that the macroscopic Maxwell equations, which describe all electromagnetic phenomena within our guided transformation-optical device, are identical to those of the coordinate-designed waveguide. However, in guided wave transformation optics, only the characteristics of guided mode propagation need to be conserved. Therefore, our framework only modifies the permittivity inside the slab in such a way that the wave equations inside the guided transformation-optical device are

identical to those of the deformed waveguide that was designed with the coordinate transformation.

Second, we introduced a geometric equivalence relation, which relates the thickness of the waveguide to the two-dimensional coordinate transformation and thus allows distinguishing the slab from the surrounding vacuum. The additional thickness variation matches the phase velocity of the guided mode within our device to that of the coordinate-designed waveguide. With the phase velocities matched, there is no further need to implement nontrivial electromagnetic responses in the surrounding vacuum. To validate our analytical equivalence relations, we investigated the performance of a 30° and 45° beam bender with finite-element simulations using the numerical software *Comsol Multiphysics*. The equivalence relations predict that the slab of a beam bender is nonmagnetic and slightly anisotropic, i.e., its material properties normal to the slab are different from those in the plane of the waveguide. The material parameters could be efficiently implemented by low-loss flatland hyperbolic metasurfaces or SiC inclusions. Therefore, our technique may indeed prove to be useful for developing transformation-optical systems in, e.g., photonic integrated circuits. Future work will also include the effects of a nontrivial substrate layer below the slab to achieve a design that naturally lends itself to such applications.

Our numerical finite-element simulations confirmed that the flatland metamaterial beam bender performs very well, both for the 30 and the 45 degree turns. In particular, we demonstrated that thickness variations are a crucial transformation-optical parameter without which the bending cannot be achieved.

Guided two-dimensional transformation optics paves the way towards guided mode manipulation with thin, flatland metamaterials. The analytical formalism that is developed in this dissertation offers a set of geometrical tools in the design of two-dimensional waveguide systems, which may be of great interest in the design of future photonic integrated circuits.

Moreover, because of the fact that wave equations and boundary conditions are a fundamental part of many disciplines in engineering and physics, like hydrodynamics, acoustics and quantum optics, we anticipate that the results of this dissertation might also be relevant to those fields.

Appendix A

Notations and Conventions

This appendix provides an overview of several notations and conventions regarding differential geometry, transformation optics and the Maxwell equations.

A.1 Coordinate Systems and Vectors

This dissertation makes use of two different notations to describe a point $\mathcal{P}$ in spacetime. When dealing with wave propagation in an optical device or metamaterial, it is convenient to use a euclidean notation $\mathcal{P} = (t, \mathbf{x})$ with time t and location $\mathbf{x}$

$$\mathbf{x} = x\ \mathbf{e}_x + y\ \mathbf{e}_y + z\ \mathbf{e}_z.$$

Directions are indicated by unit vectors $\mathbf{e}_i$ for $i \in \{x, y, z\}$.

When differential techniques are applied as in chapters 2 and 4, the relativistic notation $P = (x^0, x^1, x^2, x^3)$ is most appropriate and consists of a time coordinate $x^0 = ct$ and space coordinates $x^i = \{x, y, z\}$ for $i \in \{1, 2, 3\}$. As explained in appendix B, coordinates define coordinate bases $dx_0 = cdt$ and $dx_i = \left\{\mathbf{e}_x, \mathbf{e}_y, \mathbf{e}_z\right\}$ with respect to which vectors $\boldsymbol{\mathcal{V}}$ are expressed

$$\begin{aligned} \boldsymbol{\mathcal{V}} &= \sum_{\mu=0}^{\mu=3} V^\mu dx_\mu, \\ &= V^\mu dx_\mu. \end{aligned} \tag{A.1}$$

We use the Einstein summation convention to sum over contracted, i.e. repeated, upper and lower indices. Greek upper and lower indices indicate a summation over all spacetime coordinates, including the time component, while Roman indices imply spatial

Mathematical Object	Time- and space-dependent	Purely space-dependent
Scalar	$\mathcal{U}$	U
Vector	$\boldsymbol{\mathcal{V}}$	$\mathbf{V}$
	V^{μ}	V^{m}
Covector	$\boldsymbol{\mathcal{W}}$	$\mathbf{W}$
	W_{μ}	W_{m}
Tensor of rank $\begin{pmatrix} l \\ k \end{pmatrix}$	$\boldsymbol{\mathcal{T}}$	$\mathbf{T}$
	$T^{\mu_1\mu_2\ldots\mu_l}_{\quad\nu_1\nu_2\ldots\nu_k}$	$T^{m_1m_2\ldots m_l}_{\quad n_1n_2\ldots n_k}$

Table A.1: Conventions of tensorial notation. Time-dependent objects are denoted with a curly type set while purely spatially dependent objects are straight. The components distinguish themselves through Greek or Roman indices.

summations only

$$\begin{aligned}\mathbf{V} &= \sum_{m=1}^{m=3} V^m dx_m, \\ &= V^m dx_m.\end{aligned} \tag{A.2}$$

To distinguish vectors which depend on both space and time from those which are purely space-dependent, the former are expressed with a curly typeset, i.e. $\boldsymbol{\mathcal{P}}$, while the latter have a plain typeset, i.e. $\mathbf{P}$. Table A.1 provides an overview of different typesetting conventions. We refer to appendix B for the mathematical meaning of the differential-geometric objects.

A.1.1 Geometrical Objects

The applications of transformation optics throughout this dissertation are restricted to time-independent geometries. Therefore, we consider a spatial metric $\mathbf{g}$ with determinant g and components g_{ij} (appendix B). These are incorporated into a four-dimensional spacetime geometries $\mathcal{G}$ with orthogonal time and spatial components

$$\mathcal{G}_{\mu,\nu} = \begin{pmatrix} -g_{00} & 0 \\ 0 & \mathbf{g} \end{pmatrix},$$

with $g_{0i} = 0 = g_{i0}$ for $i \in \{1, \ldots, 3\}$. Our spatial metric $\mathbf{g}$ corresponds to the particular case for which $g_{00} = 1$. The familiar flat, euclidean space is obtained when the spatial metric reduces to an identity matrix

$$\mathbf{g}^E = \begin{pmatrix} 1 & 0 & 0 \\ 0 & 1 & 0 \\ 0 & 0 & 1 \end{pmatrix}.$$

The Kronecker delta δ_{ij} provides the component-based notation of this metric

$$\delta_{ij} = \begin{cases} 1 & i = j, \\ 0 & \text{otherwise.} \end{cases} \tag{A.3}$$

The inverse of the spatial metric g^{ij} is defined as

$$g^{ij} g_{jk} = \delta^i_k,$$

similar to the notion of an inverse matrix. It is frequently used to raise indices of tensorial objects, e.g., $V^i = g^{ik} V_k$, so that they can be used for contraction to a scalar s

$$s = V^i V_i.$$

Another important tensorial object is provided by the totally anti-symmetric symbol

$$[ijk] = \begin{cases} +1 & \text{if } [ijk] \text{ is an even permutation of } [123], \\ -1 & \text{if } [ijk] \text{ is an odd permutation of } [123], \\ 0 & \text{Otherwise,} \end{cases} \tag{A.4}$$

which provides a compact notation for the rotor of vectors $\mathbf{V}$ and $\mathbf{W}$

$$(\mathbf{V} \times \mathbf{W})^i = [ijk]\ V_j W_k. \tag{A.5}$$

In Riemannian geometries with a curved space instead of a flat space, this symbol is replaced by the Levi-Civita tensor ε^{ijk} (B.16).

A.1.2 Derivatives

We use the following shorthand notation for the partial derivative operator

$$\partial_\mu = \frac{\partial}{\partial x^\mu},$$

with $\mu \in \{0, \ldots, 3\}$. Because partial derivatives are not tensors, however, the notion of 'raised index' needs to be defined with care

$$\partial^\mu = g^{\mu\nu} \partial_\nu.$$

The order of appearance is important as the geometries may be spatially dependent.

The Jacobian $\Lambda^i_{i'}$ of a coordinate transformation X^i which expresses coordinates x^i in terms of coordinates $x^{i'}$,

$$\begin{cases} x^1 &= X^1(x^{i'}), \\ x^2 &= X^2(x^{i'}), \\ x^3 &= X^3(x^{i'}), \end{cases} \tag{A.6}$$

is key to the framework of transformation optics. It is defined as

$$\Lambda^i_{i'} = \frac{\partial x^i}{\partial x^{i'}}. \tag{A.7}$$

A.2 Conventions of Auxiliary Spaces in Transformation Optics

As explained in chapter 2, the transformation-optical framework predicts which electric and magnetic material parameters ϵ^{ij} and μ^{ij} impose the same light propagation as that within a curved design space. Indeed, the equivalence relations ((2.13)-(2.14)) impose identical Maxwell equations to the deformed space ((2.9)-(2.12)) and the device ((2.5)-(2.8)).

Literature provides two ways (Ref. [1] and [2]) to interpret the mechanism behind the transformation-optical design.

A.2.1 An active coordinate transformation with three auxiliary spaces

This dissertation describes the metamaterial design of transformation optics with the convention of Ref. [1]. As discussed in chapter 2, a coordinate transformation acts on a flat 'electromagnetic space' to design the 'deformed physical space' with desired light propagation. This nomenclature emphasizes the difference in appearance which is induced by the change of coordinates. The transformation is active.

To impose the material parameters, the Maxwell equations of 'physical space' are subsequently imposed to the space of the device. This equivalence is achieved by the aforementioned equivalence relations.

A.2.2 A passive coordinate transformation with two auxiliary spaces

In contrast, the convention of Ref. [2] emphasizes that, according to the principle of covariance, a change in coordinates does not alter the underlying physics of both spaces. In essence, the deformed space is equivalent to the undeformed space so that both are referred to as the 'electromagnetic space'. The coordinate transformation is considered to be passive.

The equivalence relations now define material parameters of the device. The actual environment, the flat euclidean space, which contains the metamaterial, is physically present in the lab. Therefore, this space is referred to as the 'physical space'.

Both conventions use identical words with different meanings. Hence, it is important to identify which convention applies to which literature.

A.3 The Maxwell Equations

A.3.1 Unit Conventions

In literature, the microscopic Maxwell equations are often expressed with respect to three different unit conventions: SI units, Heaviside units and Gaussian units.

The *SI convention* are mostly used throughout this dissertation. Using the material properties of the vacuum, the permittivity ϵ_0 and permeability μ_0, the electric $\boldsymbol{\mathcal{E}}$ and magnetic fields $\boldsymbol{\mathcal{B}}$ of different dimensions are related by the microscopic Maxwell equations

$$\nabla \cdot \boldsymbol{\mathcal{E}} = \frac{\rho_{\text{tot}}}{\epsilon_0}, \tag{A.8}$$

$$\nabla \cdot \boldsymbol{\mathcal{B}} = 0, \tag{A.9}$$

$$\nabla \times \boldsymbol{\mathcal{E}} = -\partial_t \boldsymbol{\mathcal{B}}, \tag{A.10}$$

$$\nabla \times \boldsymbol{\mathcal{B}} = \mu_0 \mathbf{j}_{\text{tot}} + \frac{1}{c^2} \partial_t \boldsymbol{\mathcal{E}}. \tag{A.11}$$

Heaviside units, are partially used in Appendix B because they provide an efficient way to deal with special and general relativistic systems. In this unit system, magnetic and electric fields have equal dimensions thanks to the speed of light in vacuum $c = \frac{1}{\sqrt{\epsilon_0 \mu_0}}$.

$$\nabla \cdot \boldsymbol{\mathcal{E}} = \rho_{\text{tot}}, \tag{A.12}$$

$$\nabla \cdot \boldsymbol{\mathcal{B}} = 0, \tag{A.13}$$

$$\nabla \times \boldsymbol{\mathcal{E}} = -\frac{1}{c} \partial_t \boldsymbol{\mathcal{B}}, \tag{A.14}$$

$$\nabla \times \boldsymbol{\mathcal{B}} = \frac{1}{c} \mathbf{j}_{\text{tot}} + \frac{1}{c} \partial_t \boldsymbol{\mathcal{E}}. \tag{A.15}$$

Finally, we do not consider the *Gaussian units* as the additional factors of 4π only serve to symplify integrations in spherical coordinates.

Because we consider monochromatic waves of fixed frequency ω, this dissertation works in the frequency domain with time-independent fields

$$\begin{aligned}
\boldsymbol{\mathcal{E}}(t, x, y, z) &= \mathbf{E}(x, y, z)\, e^{-i\omega t}, \\
\boldsymbol{\mathcal{H}}(t, x, y, z) &= \mathbf{H}(x, y, z)\, e^{-i\omega t}, \\
\boldsymbol{\mathcal{D}}(t, x, y, z) &= \mathbf{D}(x, y, z)\, e^{-i\omega t}, \\
\boldsymbol{\mathcal{B}}(t, x, y, z) &= \mathbf{B}(x, y, z)\, e^{-i\omega t}.
\end{aligned}$$

The macroscopic fields $\mathbf{D}$ and $\mathbf{H}$ appear when considering the macroscopic Maxwell equations.

A.3.2 Macroscopic Maxwell Equations

In the presence of a medium, the microscopic fields describe the local responses of all charges ρ_{tot} and $\mathbf{j}_{tot}$. We assume these responses are instantaneous, such that we work in the frequency domain. When the wavelength of the radiation is sufficiently long, the macroscopic Maxwell equations provide a more economical way to describe the medium (subsection 2.4.1)

$$\nabla \cdot \mathbf{D} = \rho_{\text{free}}, \tag{A.16}$$

$$\nabla \cdot \mathbf{B} = 0, \tag{A.17}$$

$$\nabla \times \mathbf{E} = i\omega\ \mathbf{B}, \tag{A.18}$$

$$\nabla \times \mathbf{H} = \mathbf{j}_{\text{free}} - i\omega\epsilon_0\mathbf{D}. \tag{A.19}$$

They introduce averaged fields and averaged electric and magnetic responses such that only free charges ρ_{free} and currents $\mathbf{j}_{free}$ due to metallic particles or defects appear as source terms of four macroscopic fields, the electric field $\boldsymbol{\mathcal{E}}$, the magnetic field $\boldsymbol{\mathcal{B}}$, the dielectric displacement $\boldsymbol{\mathcal{D}}$ and the magnetic field strength $\boldsymbol{\mathcal{H}}$.

Because the Maxwell equations only contain six independent equations, when assuming charge-current conservation, two of these fields are related by constitutive relations

$$D^i = \epsilon_0\epsilon^{ij}E_j, \tag{A.20}$$

$$B^i = \mu_0\mu^{ij}H_j. \tag{A.21}$$

In this dissertation, we frequently use an isotropic, dielectric constitutive relation

$$D^i = \epsilon_0\epsilon(z)\ \delta^{ij}E_j \quad B^i = \mu_0\ \delta^{ij}H_j,$$

with a permittivity profile corresponding to a slab waveguide (3.7).

Using Eq. (A.20) and Eq. (A.21), the macroscopic Maxwell equations of a nonmetallic medium—ρ_{free} and $\mathbf{j}_{free}$ equal to zero—have the following component notation

$$\partial_i\left(\epsilon_0\epsilon^{ij}E_j\right) = 0, \tag{A.22}$$

$$\partial_i\left(\mu_0\mu^{ij}H_j\right) = 0, \tag{A.23}$$

$$\sum_{jk}[ijk]\partial_j E_k = i\omega\ \mu_0\mu^{ir}H_r, \tag{A.24}$$

$$\sum_{jk}[ijk]\partial_j H_k = -i\omega\epsilon_0\epsilon^{ir}E_r. \tag{A.25}$$

The rotor is expressed by the Levi-Civita symbol according to Eq. (A.5).

A.3.3 Macroscopic Wave Equations

The remainder of this appendix derives the wave equation of the magnetic field strength for an arbitrary electromagnetic medium within its principal axes reference frame.

We assume the electric and magnetic responses are anisotropic, inhomogeneous and simultaneously diagonalized

$$\epsilon^{ij} = \begin{pmatrix} \epsilon^1 & 0 & 0 \\ 0 & \epsilon^2 & 0 \\ 0 & 0 & \epsilon^3 \end{pmatrix}, \tag{A.26}$$

$$\mu^{ij} = \begin{pmatrix} \mu^1 & 0 & 0 \\ 0 & \mu^2 & 0 \\ 0 & 0 & \mu^3 \end{pmatrix}. \tag{A.27}$$

From the perspective of transformation optics (Eq. (2.13) and Eq. (2.14)), the material parameters are only consistent with diagonal metrics.

The magnetic wave equation follows from the rotor of the law of Ampère (A.25) in combination with the law of Faraday (A.24) to simplify the results. Exceptionally, we will not apply the Einstein summation convention as it is confusing for flat euclidean spaces. The left hand side of (A.25) leads to

$$\nabla \times [\nabla \times \mathbf{H}] = \sum_m \partial_i \left(\partial_m H_m\right) - \partial_m^2 H_m,$$

a divergence term on the left and a Laplacian operator on the right. The right-hand side is simplified after substantial algebraic manipulations

$$\begin{aligned} -i\epsilon_0\omega \, \nabla \times \left(\epsilon^{ij} E_j\right) &= -i\epsilon_0\omega \sum_{jk} [ijk] \left(\epsilon^k \partial_j E_k + \partial_j \epsilon^k E_k\right), \\ &= \sum_{k\neq i} \frac{\epsilon^k \mu^i \omega^2}{c^2} H_i - i\omega\epsilon_0 \left(\sum_{jk} [ijk] \epsilon^k \partial_k E_j + \partial_j \left(\epsilon^k\right) E_k \right). \end{aligned}$$

The remaining electric fields are now simplified by using the law of Ampère (A.25), such that we arrive at the wave equations in a principal axes system for fully anisotropic materials for each $i \in \{1, \ldots, 3\}$

$$\begin{aligned} &\sum_m \partial_m^2 H_i - \sum_m \partial_i \partial_m H_m + \sum_{k\neq i} \frac{\epsilon^k \mu^i \omega^2}{c^2} H_i \\ &+ \sum_{jk} |[ijk]| \, \frac{\partial_j \epsilon^k}{\epsilon^k} \left[\partial_i H_j - \partial_j H_i\right] + \sum_{jk} |[ijk]| \, \epsilon^j \partial_j \left(\frac{1}{\epsilon^k} \left[\partial_j H_i - \partial_i H_j\right] \right). \end{aligned} \tag{A.28}$$

Isotropic Wave Equation and the Ray Approximation

In particular, we are interested in wave equations corresponding to isotropic and uniaxial materials. For an isotropic material $\epsilon = \epsilon^i$ and $\mu^i = \mu$ with $i \in \{1 \ldots 3\}$, the wave equation (A.28) reduces to

$$\left[\partial_x^2 + \partial_y^2\right] H_i + \partial_z^2 H_i + \frac{\epsilon\mu\omega^2}{c^2} H_i + \partial_i \left[\frac{\nabla\mu}{\mu} \cdot \mathbf{H} \right] + \left[\frac{\nabla\epsilon}{\epsilon} \times (\nabla \times \mathbf{H}) \right].$$

We recognize the refractive index $n = \sqrt{\epsilon\mu}$ in front of the frequency-dependent term and logarithmic terms $\frac{\nabla\mu}{\mu}$ and $\frac{\nabla\epsilon}{\epsilon}$, due to the inhomogeneous medium.

We are now able to understand the ray approximation in more detail. If the magnetic field contains a slowly varying amplitude $\mathbf{H}_0(x, y, z)$ and a quickly varying phase $\phi(x, y, z)$

$$\mathbf{H}(x, y, z) = \mathbf{H}_0(x, y, z)\, e^{i\phi(x,y,z)} \tag{A.29}$$

and propagation vector $\boldsymbol{\beta}$

$$\boldsymbol{\beta} = \nabla\phi(x, y, z), \tag{A.30}$$

$$\beta = n_{eff}\frac{\omega}{c}, \tag{A.31}$$

the full wave equation splits into a zeroth-order **A**, first-order **B** and second-order **C** contribution in $\frac{\omega}{c}$,

$$\begin{aligned}
&\mathbf{A} + \mathbf{B} + \mathbf{C} = 0,\\
&\mathbf{A} = \Delta\mathbf{H}_0 + \frac{\nabla\epsilon}{\epsilon} \times (\nabla \times \mathbf{H}_0) + \left(\frac{\nabla\mu}{\mu} \cdot \nabla\right)\mathbf{H}_0,\\
&\mathbf{B} = \left[\nabla \cdot \boldsymbol{\beta} - \left(\frac{\nabla\epsilon}{\epsilon} \cdot \boldsymbol{\beta}\right)\right]\mathbf{H}_0 + \boldsymbol{\beta}\left[\frac{\nabla\epsilon}{\epsilon} + \frac{\nabla\mu}{\mu}\right] \cdot \mathbf{H}_0\\
&\mathbf{C} = \left(\epsilon\mu - n_{eff}^2\right)\frac{\omega^2}{c^2}.
\end{aligned}$$

These results are similar to the derivation of Ref. [3] which derives the electric wave equation directly from the Maxwell equations of an isotropic, inhomogeneous medium. The zeroth order operator **A** only acts on the amplitudes, the first-order operator **B** acts once on the phase and once on the inhomogeneous amplitude while the second order operator **C** acts twice on phase.

In the limit of the ray approximation, when the wavelength becomes negligibly small and the phase oscillates rapidly, the wave equation reduces to the operator **C**. This equation is often referred to as the *eikonal equation*. Because the polarization of the field does not affect **C**—the fields do not couple—the ray approximation treats fields as if they are scalars. In this scalar approximation, the wave equation in physical space is equal to (4.29) and the propagation vector (A.30) determines the fields completely.

Uniaxial Material Parameters

In case of uniaxial constitutive relations

$$\epsilon^{ij} = \begin{pmatrix} \tilde{\epsilon} & 0 & 0 \\ 0 & \tilde{\epsilon} & 0 \\ 0 & 0 & \epsilon_z \end{pmatrix} \quad \mu^{ij} = \begin{pmatrix} \tilde{\mu} & 0 & 0 \\ 0 & \tilde{\mu} & 0 \\ 0 & 0 & \mu_z \end{pmatrix}, \tag{A.32}$$

wave equation (A.28) changes into two separate expressions, one for in-plane magnetic field strength components $i, j \in \{x, y\}$ and $j \neq i$

$$\left[\partial_x^2 + \partial_y^2\right] H_i + \frac{\epsilon_z}{\tilde{\epsilon}} \partial_z^2 H_i + \frac{\epsilon_z \tilde{\mu} \omega^2}{c^2} H_i + \frac{\partial_j \epsilon_z}{\epsilon_z} \left[\partial_i H_j - \partial_j H_i\right] = 0, \tag{A.33}$$

and one for the orthogonal component of the wave equation

$$\left[\partial_x^2 + \partial_y^2\right] H_z + \mu_z \partial_z^2 H_z + \frac{\tilde{\epsilon} \mu_z \omega^2}{c^2} H_z \tag{A.34}$$

$$+ \frac{\partial_x \tilde{\epsilon}}{\tilde{\epsilon}} \left[\partial_z H_x - \partial_x H_z\right] + \frac{\partial_y \tilde{\epsilon}}{\tilde{\epsilon}} \left[\partial_z H_y - \partial_y H_z\right] = 0. \tag{A.35}$$

We notice the extraordinary magnetic component only appears in the z-component wave equation which is completely decoupled from the other wave equations. Thus, if the fields have no orthogonal H_z component, as for TM modes in a slab waveguide, one might use an isotropic magnetic material with $\mu = \tilde{\mu}$. Additionally, if $\tilde{\mu}$ is equal to one, the material is nonmagnetic.

References

[1] U. Leonhardt and T. G. Philbin, "Transformation optics and the geometry of light," *Progress in Optics* **53**, 69–152, 2009.

[2] V. Ginis, *Transforming Electromagnetic Reality: On the Physics and Applications of Metamaterials*, VUB-Press, 2014.

[3] E. Wolf and M. Born, *Principles of Optics*, Pergamon press, 1965.

Appendix B

Differential Geometry

In this Appendix, we derive the Maxwell equations on a curved space. In doing so, we establish several differential-geometrical relations which are important when adapting the traditional transformation-optical framework for manipulating a realistic slab waveguide. We will relate the time-independent results of this dissertation to the relativistic formulation valid within a curved space-time.

B.1 Coordinate Bases and Transformations

Before we are able to understand how a coordinate transformation, and a Riemannian geometry, modify the Maxwell equations on a flat space, we investigate what coordinates, vectors and coordinate bases really represent in a curved geometry.* Each space-time point $\mathcal{P}$ is expressed with respect to a set of coordinates x^μ which define four independent directions corresponding to base components dx_μ. Technically, these base components are part of a coordinate base, constructed by partial differential operators $dx_\mu = \frac{\partial}{\partial x^\mu}$. Therefore, Fig. B.1 shows how these bases change

$$dx_\mu = \frac{\partial x^{\mu'}}{\partial x^\mu}\, dx_{\mu'} \tag{B.1}$$

when an inversible, differentiable coordinate transformation

$$x^\mu = X^\mu(x^{\mu'}), \tag{B.2}$$

swaps the coordinate system $x^{\mu'}$ for another coordinate system x^μ with $\mu, \mu' \in \{0, \ldots, 3\}$. Because of its reversibility, the Jacobian $\Lambda^{\mu'}_{\mu} = \frac{\partial x^{\mu'}}{\partial x^\mu}$ has a nonzero determinant $\Lambda = \det \frac{\partial x^{\mu'}}{\partial x^\mu}$. Thanks to the covariance of physical theories, each vector $\mathcal{V}$ at the point $\mathcal{P}$

$$\mathcal{V} = V^\mu e_\mu, \tag{B.3}$$

*For notational conventions, we refer to Appendix A

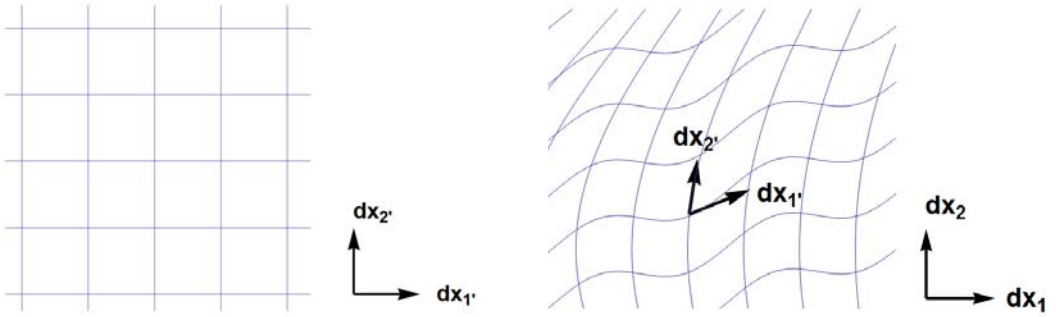

Figure B.1: The effects of a coordinate transformation on two coordinate basis covectors $dx_{1'}$ and $dx_{2'}$.

expressed with respect to a particular basis and coordinate system x^μ, should not fundamentally change because of this coordinate transformation. To achieve this, the vector components V^μ transform in the following way

$$V^\mu = \Lambda^\mu_{\mu'} V^{\mu'}, \tag{B.4}$$

$$dx_\mu = \Lambda^{\mu'}_{\mu} dx_\mu, \tag{B.5}$$

if $\Lambda^{\mu'}_{\nu}$ is the inverse of the Jacobian $\Lambda^\mu_{\mu'}$

$$\Lambda^\mu_{\mu'} \Lambda^{\mu'}_{\nu} = \delta^\mu_\nu.$$

The reader might verify the vector (B.3) indeed does not change due to a coordinate transformation because the Jacobians of Eq. (B.4) and (B.5) cancel exactly.

B.2 Vectors, Covectors and Tensorial Objects

In addition to vectors, there are several other tensorial objects which are relevant to transformation optics. Similar to vectors, these tensorial objects use the Jacobian $\Lambda^\mu_{\mu'}$ of an arbitrary coordinate transformation (B.2) to maintain a coordinate-independent meaning. We shortly describe these transformation properties for two different mathematical objects, covectors and tensors, and refer to [1] for a detailed treatment.

A covector $\mathcal{W}$ with components W_μ is dual to the notion of a vector and will play a crucial role throughout this dissertation. Its transformation rule is derived by contracting it with a vector V^μ to produce a scalar s

$$s = W_\mu V^\mu. \tag{B.6}$$

Because scalars do not depend on coordinate systems in any way, the covector transforms according to

$$W_\mu = \Lambda_\mu^{\mu'} W_{\mu'}. \tag{B.7}$$

as it needs to compensate the change of the vector components (B.4).

The most general tensorial object $\mathcal{T}$ of rank (l, k) has l upper and k lower indices. When such a tensor is contracted with l different covectors W_{ν_i} with $i \in \{1 \dots l\}$ and k arbitrary vector components V^{μ_j} with $j \in \{1 \dots k\}$

$$s = T^{\nu_1 \dots \nu_l}{}_{\mu_1 \dots \mu_k} V^{\mu 1} \dots V^{\mu_k} W_{\nu_1} \dots W_{\nu_l},$$

it also produces a scalar which remains invariation under coordinate transformations. Therefore, $T^{\nu_1 \dots \nu_l}{}_{\mu_1 \dots \mu_k}$ transforms in the following way

$$T^{\nu_1 \dots \nu_l}{}_{\mu_1 \dots \mu_k} = \Lambda_{\nu_1}^{\nu_1} \dots \Lambda_{\nu_l'}^{\nu_l} \Lambda_{\mu_1}^{\mu_1'} \dots \Lambda_{\mu_k}^{\mu_k'} T^{\nu_1' \dots \nu_l'}{}_{\mu_1' \dots \mu_k'}. \tag{B.8}$$

All upper indices transform as vector components while all lower indices transform as covector components. In particular, this dissertation makes use of two tensorial objects, the metric tensor $g_{\mu\nu}$ and the three-dimensional totally antisymmetric Levi-Civita tensor ε^{ijk}.

B.2.1 The Metric Tensor $g_{\mu\nu}$

As explained in chapter 2, the effect of transformation-optical metamaterials on light is identical to that of a Riemannian geometry with metric tensor g_{ij}. This metric tensor determines a distance between, or a norm of, two vectors dx^μ and dx^ν

$$ds^2 = g_{\mu\nu} dx^\mu dx^\nu. \tag{B.9}$$

Because the order of the vectors dx^μ and dx^ν does not affect the value of the distance ds^2, the metric is necessarily symmetric $g_{\mu\nu} = g_{\nu\mu}$. According to the tensor transformation rule, the metric changes in the following way

$$g_{\mu\nu} = \Lambda_\mu^{\mu'} \Lambda_\nu^{\nu'} g_{\mu'\nu'} \tag{B.10}$$

with initial coordinates $x^{\mu'}$ expressed as a function of the final coordinates x^μ. The determinant g is not a scalar

$$g = \Lambda^2 g', \tag{B.11}$$

as there is a factor $\Lambda = \det\Lambda_\mu^{\mu'}$ which depends on the coordinate transformation. In particular, if the initial space has a flat, spatial geometry $g_{ij} = \delta_{ij}$ —as is mostly the case for the electromagnetic space in transformation optics—the coordinate transformation induces the following spatial metric

$$g_{ij} = \Lambda_i^{i'} \Lambda_j^{j'} \delta_{i'j'}, \tag{B.12}$$

$$g = \Lambda^2. \tag{B.13}$$

Finally, the metric $g_{\mu\nu}$ has one other important property. Together with the inverse metric g^{ij} which determines distances between covectors dx_μ and dx_ν

$$\begin{aligned} ds^2 &= g^{\mu\nu} dx_\mu dx_\nu, \\ \delta^\mu_\rho &= g^{\mu\nu} g_{\nu\rho}, \end{aligned}$$

it has the capacity to raise and lower indices of vectors $\mathcal{V}$, covectors $\mathcal{W}$ and tensorial components as illustrated below

$$\begin{aligned} V_\mu &= g_{\mu\nu} V^\nu \qquad T^{\mu_1 \cdots\ \mu_{l-1}}_{\quad\ \nu_0 \nu_1 \ldots \nu_k} = g_{\nu_0 \mu_l} T^{\mu_1 \ldots \mu_l}_{\quad\ \nu_1 \ldots \nu_k}, \\ W^\mu &= g^{\mu\nu} W_\nu \qquad T^{\mu_1 \cdots\ \mu_{l+1}}_{\quad\ \nu_2 \ldots \nu_k} = g^{\mu_{l+1} \nu_1} T^{\mu_1 \cdots \mu_l}_{\quad\ \nu_1 \ldots \nu_k}. \end{aligned}$$

Therefore, a metric is capable of producing covectors out of vectors and vice versa.

B.2.2 The Levi-Civita Tensor ε^{ijk}

In a flat space, the cross product of two covectors $\mathbf{V}$ and $\mathbf{W}$

$$(\mathbf{V} \times \mathbf{W})^i = [ijk]\ V_j W_k, \tag{B.14}$$

is written in component form using a totally antisymmetric symbol with respect to a right-handed coordinate system

$$[ijk] = \begin{cases} +1 & \text{if } [ijk] \text{ is an even permutation of } [123], \\ -1 & \text{if } [ijk] \text{ is an odd permutation of } [123], \\ 0 & \text{Otherwise} \end{cases} \tag{B.15}$$

with $i, j, k \in \{1, 2, 3\}$. If the cross-product is generalized such that it still is a vector on a Riemannian geometry, the antisymmetric symbol $\tilde{\varepsilon}^{ijk} = [ijk]$ should be a 3-tensor. However, as a consequence of the relation between the determinant of a matrix and the totally antisymmetric symbol, $[i'j'k']$ transforms according to [2]

$$\begin{aligned} \tilde{\varepsilon}^{ijk} &= \Lambda^i_{i'} \Lambda^j_{j'} \Lambda^k_{k'}\ [i'j'k'], \\ &= \pm \det\Lambda\ [ijk], \\ &\neq [ijk], \end{aligned}$$

with Jacobian $\Lambda = \det \frac{x^\mu}{x^{\mu'}}$. The plus sign corresponds to a transformation which preserves the handedness of the coordinate system while the minus sign is associated to a transformation which reverses the handedness of the coordinate system. Though there is an anomalous factor $\det\Lambda$ which prevents $[ijk]$ from being a 3-tensor, Eq. (B.13) shows how to correct it. We use the determinant of the metric to omit the Jacobian factor and define the Levi-Civita tensor ε^{ijk} as follows

$$\varepsilon^{ijk} = \frac{\pm 1}{\sqrt{g}}\ [ijk]. \tag{B.16}$$

In this way, the generalized cross product of two covectors on a three-dimensional spatial Riemannian geometry is equal to

$$\mathcal{V} \times \mathcal{W} = \varepsilon^{ijk} V_j W_k. \tag{B.17}$$

and agrees with Eq. (B.17) in the case of a flat space, $g = 1$. When all indices of the Levi-Civita tensor are lower case, i.e. the tensor is 'inversed', the metric factor appears in the nominator instead

$$\varepsilon_{ijk} = \pm \sqrt{g}\,[ijk]\,. \tag{B.18}$$

As a consequence, the Levi-Civita tensors with upper indices and lower indices (Eq. (B.16)) contract independent from the geometry

$$\begin{aligned} \epsilon ijk \epsilon_{klm} &= \sum_{j\,k\,l\,m} [ijk][klm], \\ &= \delta^i_l \delta^j_m - \delta^i_m \delta^j_l. \end{aligned} \tag{B.19}$$

B.3 Covariant Maxwell Equations on a Spatial Geometry

We now use the Principle of Equivalence to derive the Maxwell equations on a spatial, three-dimensional Riemannian geometry with metric g_{ij}. Next to covariance, this Principle states each point **P** in space has a particular coordinate system $x^{i'}$ with respect to which the geometry becomes locally flat $g_{i',j'} = \delta_{i'j'}$. In the presence of an isotropic dielectric $\tilde{\epsilon}$, the macroscopic Maxwell equations are equal to

$$\partial_{i'} \left(\tilde{\epsilon} E^{i'} \right) = 0, \tag{B.20}$$

$$\partial_{i'} H^{i'} = 0, \tag{B.21}$$

$$[i'j'k']\, \partial_{j'} E_{k'} = -\mu_0\, \partial_t \left(H^{i'} \right), \tag{B.22}$$

$$[i'j'k']\, \partial_{j'} H_{k'} = \epsilon_0\, \partial_t \left(\tilde{\epsilon} E^{i'} \right). \tag{B.23}$$

This component notation guarantees the Gauss laws ((B.20)-(B.21)) are scalar equations, due to the Einstein summation convention, while the expression of the cross-product in terms of components (Eq. (B.14)) is applied to the left hand sides of the laws of Faraday (B.22) and Ampère (B.23). Only when the differential operators, i.e. the divergence and rotor operators on a flat space

$$\nabla \cdot \mathbf{V} = \partial_i V^i, \tag{B.24}$$

$$[\nabla \times \mathbf{W}]^i = [ijk]\, \partial_j W_k, \tag{B.25}$$

are generalized to a Riemannian geometry, we obtain spatially covariant Maxwell equations ((B.39)-(B.42)).

B.3.1 The Covariant Derivative

Intuitively, Fig. B.1 implies the derivative of a vector $\mathbf{V} = V^i dx_i$, i.e., the infinitesimal change in the vector as it is moved along a coordinate line, contains two contributions

$$\partial_j \mathbf{V} = \left(\partial_j V^i\right) dx_i + V^i \left(\partial_j \left[dx_i\right]\right), \tag{B.26}$$

one due to the change of vector components V^i and one due to the base component dx_i. To simplify this expression, we define a connection Γ^i_{jk}, a set of 27 coefficients which expand the derivative of dx_i in a linear way with respect to the complete coordinate basis dx_k

$$\partial_j \left[dx_i\right] = \Gamma^k_{ji} dx_k. \tag{B.27}$$

After relabeling some dummy indices, Eq. (B.26) and (B.27) define the covariant derivative $\nabla_j V^i$ of a vector

$$\partial_j \mathbf{V} = \left(\partial_j V^i + \Gamma^i_{jk} V^k\right) dx_i, \tag{B.28}$$

$$\nabla_j V^i = \partial_j V^i + \Gamma^i_{jk} V^k, \tag{B.29}$$

which is indeed a 2-tensor because of the definition of the Christoffel symbols (B.27).

The derivative of a covector $\mathbf{W}$ then immediately follows from the Leibniz rule of differentiation applied to Eq. (B.6)

$$\nabla_j W_i = \partial_j W_i - \Gamma^k_{ji} W_k. \tag{B.30}$$

Notice that the covariant derivative yields another 2-rank tensor, with two lower indices and a minus sign as compared to Eq. (B.29).

B.3.2 Geometrical Assumptions

The divergence and rotor on a Riemannian geometry g_{ij} now follow from two additional geometrical assumptions [1]. Firstly, we assume the connection (B.27) is torsionless, i.e. symmetric in the lower indices Γ_{ij}. Secondly, the covariant derivative is metric compatible

$$\nabla g_{ij} = 0. \tag{B.31}$$

Both assumptions are very restrictive and relate the connection coefficients in a unique way to the metric components

$$\Gamma^i_{jk} = \frac{1}{2} g^{ir} \left[\partial_j g_{rk} + \partial_k g_{jr} - \partial_r g_{jk}\right]. \tag{B.32}$$

Since this particular connection Γ^i_{jk} is very important to General Relativity, they have several names among which Christoffel symbols and Levi-Civiita symbols occur most

often. We will use the symmetry $\Gamma^i_{jk} = \Gamma^i_{kj}$ in Section B.4 to simplify the derivation of the wave equations on a Riemannian geometry considerably.

The aforementioned assumptions influence the nature of the Riemannian geometry in an important way. Generally, the curvature of a space is characterized by the Riemannian 4-tensor $R^i{}_{jkl}$. In a flat space, any vector V^i that is parallel transported around a small closed loop, has exactly the same 'orientation' when it arrives at the starting point. Curvature, however, twists the space and induces a change δV^i between the initial and the final vector

$$\delta V^i = R^i{}_{jkl} V^j,$$

if it is moved along a quadrilateral curve with sides along the k and l direction. Mathematically, this change is expressed by the commutator of covariant derivatives

$$\left[\nabla_k \nabla_l - \nabla_l \nabla_k\right] V^i = R^i{}_{jkl} V^j, \tag{B.33}$$

which defines the Riemannian tensor

$$R^i{}_{jkl} = \partial_k \Gamma^j_{il} - \partial_l \Gamma^j_{ik} + \Gamma^i_{kr}\Gamma^r_{lj} - \Gamma^i_{lr}\Gamma^r_{kj}. \tag{B.34}$$

As expected, it is antisymmetric with respect to the indices k and l since the loop is transversed in the opposite direction if these are exchanged.

The Rieman tensor produces two important lower-dimensional tensors. The Ricci tensor R_{kl} is obtained when contracting one pair of indices

$$R_{jl} = R^i{}_{jil}. \tag{B.35}$$

Therefore it changes the commutator (B.33) into

$$R_{jl} V^l = \left[\nabla_j \nabla_l - \nabla_l \nabla_j\right] V^l. \tag{B.36}$$

This relation will play an important role in chapter 4 when deriving the wave equation in a Riemannian geometry. From the Ricci tensor, it is possible to derive the second important 'tensorial' object. This is simply the scalar curvature R

$$R = R^i{}_i.$$

Because the curvature is described by tensorial objects, clearly these vanish in any space which is connected by an invertible, differentiable coordinate transformation to a flat space. Therefore, in this dissertation, we assume

$$\begin{aligned} R^i{}_{jkl} &= 0, \\ R_{ij} &= 0, \\ R &= 0, \end{aligned}$$

such that covariant derivatives commute.

B.3.3 Differential Operators

Because the covariant derivative is a tensorial object, the divergence (B.24) and rotor (B.25) are immediately generalized to a Riemannian geometry g_{ij} when the partial derivatives are replaced by covariant derivatives and the antisymmetric symbol is expressed by the Levi-Civita tensor B.16

$$\nabla \cdot \mathbf{V} = \nabla_i V^i,$$
$$[\nabla \times \mathbf{W}]^i = \varepsilon^{ijk} \nabla_j W_k.$$

Using the symmetry of the lower indices in the Christoffel connection (B.32), these equations are elegantly expressed with respect to partial derivatives

$$\nabla \cdot \mathbf{V} = \frac{1}{\sqrt{g}}\, \partial_i \left(\sqrt{g} g^{ij} V_j \right), \tag{B.37}$$

$$\nabla \times \mathbf{W} = \pm \frac{[ijk]}{\sqrt{g}} \partial_j W_k. \tag{B.38}$$

When using Eq. (B.37) and Eq. (B.38) it is extremely important never to swap the partial derivatives with metric components. Metric compatibility is only guaranteed by the full covariant derivative (Eq. (B.29) and Eq. (B.30)).

B.3.4 Spatially Covariant Maxwell Equations

Using the generalized definitions of the divergence (B.37) and rotor (B.38), the Maxwell equations ((B.20)-(B.23)) in righthanded locally flat coordinates $x^{i'}$ may now be expressed with respect to arbitrary righthanded coordinates x^i with nontrivial metric g_{ij}

$$\partial_i \left(\sqrt{g}\, \tilde{\epsilon} g^{ij} E_j \right) = 0, \tag{B.39}$$

$$\partial_i \left(\sqrt{g}\, g^{ij} H_j \right) = 0, \tag{B.40}$$

$$[ijk]\, \partial_j E_k = -\mu_0\, \partial_t \left(\sqrt{g} g^{ir} H_r \right), \tag{B.41}$$

$$[ijk]\, \partial_j H_k = \epsilon_0\, \partial_t \left(\sqrt{g} \tilde{\epsilon} g^{ir} E_r \right). \tag{B.42}$$

These equations implicitly assume the metric determinant is time-independent such that it can be exchanged with the time derivative in the laws of Faraday and Ampère. Both sets of Maxwell equations, those in a flat geometry with an isotropic dielectric $\tilde{\epsilon}$ ((B.20)-(B.23)) and those in a Riemannian geometry ((B.39)-(B.42)), are respectively related to the electromagnetic space and the physical space of the transformation optical framework (Chapter 2) [2].

Although we obtained the correct Maxwell equations on a Riemannian geometry, there are some ambiguities which are only resolved by a fully covariant relativistic treatment.

In writing down the Maxwell equations ((B.20)-(B.23)), we implicitely assumed the physical observables

$$D^i = \tilde{\epsilon} E^i,$$
$$B^i = \mu_0 H^i,$$

are vectors with upper indices as they appear on equal footing with the electric current density $\mathbf{j}$. This has important consequences for the expression of the equivalence relations as these require an accurate description of the vectorial or covectorial nature of the fields in flat space. Therefore, we have derived an alternative explanation to that of literature to confirm this picture.

The relativistic, covariant Maxwell equations are expressed by one anti-symmetric two-form [3]

$$\mathcal{F} = F_{\mu\nu} dx^\mu dx^\nu, \tag{B.43}$$

in the following way

$$\nabla_\nu F^{\mu\nu} = J^\mu, \tag{B.44}$$
$$\partial_{[\rho} F_{\mu\nu]} = 0, \tag{B.45}$$

using a microscopic 4-vector current $J^\mu = (\rho, \mathbf{j})$ containing all charges and currents with respect to a particular coordinate system. The second equation (B.45)—known as the Bianchi identity—uses the totally antisymmetric symbol $[\rho\mu\nu]$ which has a similar definition as Eq. (B.15). Therefore, the symmetry of the Christoffel symbols allows writing it with partial derivatives instead of covariant ones.

We now apply the partial derivative formulation of the divergence (B.37) to the first equation (B.44), and distinguish between space- and temporal values of μ

$$\partial_\nu \left(\sqrt{g}\, F^{0\nu} \right) = \sqrt{g}\, \rho,$$
$$\partial_\nu \left(\sqrt{g}\, F^{m\nu} \right) = \sqrt{g}\, j^m.$$

If we assume the presence of a dielectric, with bound charges $\rho_P = -\nabla \cdot \mathbf{P}$ and currents $\mathbf{j}_P = \partial_t \mathbf{P}$ with $P^m = \chi F^{0m}$, the covariant Maxwell equations in a curved space are equal to

$$\partial_n \left(\sqrt{g}\, [1 + \chi]\, F^{0n} \right) = 0, \tag{B.46}$$
$$\partial_n \left(\sqrt{g}\, F^{mn} \right) = \partial_t \left([1 + \chi]\, j^m \right). \tag{B.47}$$

The first Eq. (B.46) does not contain a temporal index $\nu = 0$ because $F^{\mu\nu}$ is antisymmetric. Similarly, the second Eq. (B.47) requires m is different from zero and from n. Then, Eq. (B.46) and (B.47) respectively reduce to the macroscopic Gauss law (B.39) and the law of Ampère (B.42) if we define

$$D^n = \sqrt{g}\, \tilde{\epsilon}\, F^{0n}, \tag{B.48}$$
$$B^n = \frac{\sqrt{g}}{2}\, \varepsilon^{nlm} F_{lm}, \tag{B.49}$$

using the Levi-Civita tensor ε^{nlm} (B.16) and permittivity $\tilde{\epsilon} = 1 + \chi$. The macroscopic fields **D** and **B** indeed have upper indices. However, because of the transformation rule of the metric (B.11), an additional factor det Λ appears with respect to a purely (spatial) vectorial transformation. Thus, these fields transform as pseudo-vectors, or more generally, tensor densities of weight +1. Similarly, the Bianchi identity (B.45) identifies an electric field E_n and magnetic field strength H_n

$$E_n = F_{n0}, \tag{B.50}$$

$$H_n = \frac{\varepsilon_{nlm}}{2} F^{im}. \tag{B.51}$$

These fields transform as spatial covectors. Therefore, the component notation in ((B.20)-(B.23)) is uniquely defined by the vectorial character of the current density and the relativistic Maxwell equations. Throughout this dissertation, the curved geometry acts on the magnetic fields strength (B.51) as if it is a covector.

B.4 Wave Equations on a Riemannian Geometry

In this Section, we derive the wave equations related to the laws of Faraday (B.41) and Ampère (B.42) on a Riemannian geometry in terms of partial derivatives. Since the covariant derivative acts differently on scalars, vectors (B.4) and covectors (B.7), the resulting wave equations have different signatures related to the tensorial nature of the object on which they act. The covector wave equation is in particular important as it provides the Helmholtz equation in physical space of the TM mode with magnetic field strength **H**.

B.4.1 Covector Wave Equation

As in Subsection 4.2.1, we obtain the wave-equation of a covector magnetic field **H** when acting on the law of Ampère with a generalized rotor (B.38)

$$\epsilon_{ijk} \nabla^j \left(\epsilon^{klm} \nabla_l H_m \right) - \frac{\tilde{\epsilon}(z)\omega^2}{c^2} H_i = 0. \tag{B.52}$$

We now focus on the geometrical dependence of the first term. Instead of exploiting the metric compatibility (B.31) as in Subsection 4.2.1, we explicitely introduce the covariant derivatives into the rotor operators. The inner covariant derivative of Eq. (B.52)

$$\left(\epsilon^{klm} \nabla_l H_m \right) = \sum_{l\,m} \frac{[klm]}{\sqrt{g}} \partial_l H_m,$$

simplifies to a partial derivative because the symmetric Christoffel symbol Γ^k_{lr} (B.32) contracts with the totally antisymmetric symbol $[klm]$. More importantly, the outer

covariant derivative does not simplify because it acts on a vector

$$V^k = \sum_{lm} \frac{[klm]}{\sqrt{g}} \partial_l H_m$$

in the following way (B.29)

$$\sum_{j\,k\,l\,m} [ijk]\ \sqrt{g} g^{jr} \left[\partial_r V^k + \Gamma^k_{rs} V^s \right],$$

$$\sum_{j\,k\,l\,m\,s} [ijk][slm]\ \sqrt{g} g^{jr} \left[\delta^s_k\, \partial_r \left(\frac{1}{\sqrt{g}} \partial_l H_m \right) + \frac{1}{\sqrt{g}}\, \Gamma^k_{rs}\, \partial_l H_m \right]. \tag{B.53}$$

Using the contraction property of totally antisymmetric symbols (B.19), we obtain a general expression for the rotor dependent terms of the wave equation (B.52)

$$\sqrt{g} g^{jr} \partial_r \left(\frac{1}{\sqrt{g}} \partial_j H_i \right) - \sqrt{g} g^{jr} \partial_r \left(\frac{1}{\sqrt{g}} \partial_i H_j \right)$$

$$- \sum_{j\,k\,s\,l\,m} g^{jr}\, [ijk]\, [slm]\, \Gamma^k_{rs}\, \partial_l H_m + \frac{\tilde{\epsilon}(z)\omega^2}{c^2} H_i = 0, \tag{B.54}$$

which consists of a laplacian term (upper left), a term related to the divergence (upper right) and a term due to the nontrivial geometry of physical space (lower left) together with the frequency-dependent term of Eq. (B.52).

B.4.2 Other Wave Equations

All other wave equations are derived in a similar way. If the electromagnetic field components are approximately described by a scalar function $\phi(x^i)$—an assumption which is valid in the ray approximation—the wave equation simply contains a laplacian operator Δ

$$\Delta\phi(x^i) + \frac{\tilde{\epsilon}(z)\omega^2}{c^2} \phi(x^i) = 0,$$

$$\Delta\phi(x^i) = \nabla_j \nabla^j \phi(x^i).$$

Because $\phi(x^i)$ does not connect to any coordinate base component dx^i, its covariant derivative ∇_i is equal to a partial derivative ∂_i. The gradient vector is obtained when the index is raised

$$\nabla^j \phi(x^i) = g^{ir} \partial_r \phi(x^i),$$

such that the wave equation is equal to

$$\frac{1}{\sqrt{g}} \partial_j \left(\sqrt{g} g^{jr} \partial_r \phi(x^i) \right) + \frac{\tilde{\epsilon}(z)\omega^2}{c^2} \phi(x^i) = 0. \tag{B.55}$$

The vector wave equation is derived in a similar way to the covector wave equation. The covariant wave equation

$$\epsilon^{ijk}\nabla_j\left(\epsilon_{klm}\nabla^l H^m\right) - \frac{\tilde{\epsilon}(z)\omega^2}{c^2}H^i = 0, \tag{B.56}$$

differs from the covector equation (B.52) in that all upper indices become lower indices and vice versa. This has important consequences for the inner rotor

$$\epsilon_{klm}\nabla^l H^m = \epsilon_{klm}g^{lr}\left[\partial_r H^m + \Gamma^m_{rs}H^s\right],$$

which does not reduce to a simple partial derivative because the Christoffel coefficients have no symmetry in the upper-indices. Therefore, the general wave equation in a Riemannian geometry contains an additional dependence on the Christoffel symbol as compared to the covector wave equation (B.54)

$$\frac{1}{\sqrt{g}}\partial_k\left[\sqrt{g}g^{ir}\partial_r H^k\right] - \frac{1}{\sqrt{g}}\partial_k\left[\sqrt{g}g^{kr}\partial_r H^i\right] \tag{B.57}$$

$$\frac{1}{\sqrt{g}}\partial_k\left[\sqrt{g}g^{ir}\Gamma^k_{rs}H^s\right] - \frac{1}{\sqrt{g}}\partial_k\left[\sqrt{g}g^{kr}\Gamma^i_{rs}H^s\right]. \tag{B.58}$$

The covariant formulation (B.52) provides an important check on the covector (B.54) and the vector wave equations (B.58). Due to metric compatibility, the covector magnetic field strength H_i

$$H_i = g_{is}H^s, \tag{B.59}$$

in Eq. B.52 may be replaced by a vector H^s since metric components are easily put outside of the differential operators. Therefore, the vector equation on H^s emerges from the covector equation on H_i. Our partial derivative formulations of the covector (B.54) and vector (B.58) wave equations indeed reduce to one another when substituting H_i by Eq. (B.59). It is however not allowed to put the metric components out of the partial derivatives, such that calculations are rather long.

References

[1] S. M. Caroll, *An Introduction to General Relativity, Space-time and Geometry*, Addison-Wesly, 2004.

[2] U. Leonhardt and T. G. Philbin, "Transformation optics and the geometry of light," *Progress in Optics* **53**(08), 69–152, 2009.

[3] C. W. Misner, K. S. Thorne, and J. A. Wheeler, *Gravitation*, W.H Freedman and Company, 1970.

Appendix C

Comsol Multiphysics

To corraborate the analytical predictions of this dissertation, we relied on two numerical softwares, *Wolfram Mathematica 7* and *Comsol Multiphysics 4v*. This appendix provides an overview of the relevant simulational and numerical techniques. Because *Mathematica* is mainly a postprocessing tool, we focus on finite-element simulations in the frequency domain as implemented by the Radio-Frequency (RF) module of *Comsol*.

C.1 The Finite-Element Method

Continuous partial differential equations, i.e., the electromagnetic wave equation with initial conditions and boundary conditions, posses an infinite number of degrees of freedom. Therefore, to solve these equation in a numerical way, the infinite number of degrees of freedom should be reduced to a finite number of variables which a computer can handle [1]. This is done by discretization of the simulation domain which contains the subject or configuration of study together with appropriate boundary conditions.

To discretize and solve the Maxwell equations in a one-dimensional simulation domain with N subdivisions, the solver needs to determine $3N$ field components, e.g., three independent components of the electric fields which in turn determine the magnetic fields through the law of Faraday. Additionally, spatial information is obtained by N coordinate values associated to positions of different subdivisions. From now on, such subdivisions are called mesh vertices. If now, we extend the simulation to d dimensions, a homogeneous subdivision of the simulation domain requires N^d elements and discretization of partial becomes increasingly nontrivial. Our simulation domains are three-dimensional which requires efficient discretization, i.e. differential meshing, to guarantee efficient computing. Differential meshes are inhomogeneous subdivisions of the simulation domain which anticipate regions of intense fields or small geometrical features require more mesh elements to guarantee a stable numerical solution (subsection C.4).

A discretized wave equation may be solved in two ways. Finite-difference methods translate the initial continuous differential equations into difference equations at each node/vertex. In this way, all partial derivatives are replaced by differences between fields evaluated at neighboring nodes.

In this master dissertation we apply the finite-element method in the frequency domain. The finite-element method uses an integral formulation of the partial differential equation. It defines volume elements, e.g., tetrahedral or quadrilateral elements which are bound by vertices, such that the material properties and fields are approximately constant within such a volume element. Then, it integrates the equations within such a homogeneous element to obtain local, discretized Maxwell equations which depend on the content of the mesh unit. Next to efficient meshing, the finite-element approach demands the mesh is sufficiently fine such that the integral formulation is indeed valid.

After discretization, a large but finite number of variables, e.g., fields at vertices, need to be solved. There are two types of solvers: a direct solver and an indirect solver. Indirect solvers impose an initial solution to the discretized domain and reduce a merit function in an iterative way [1]. We initially relied on this kind of solver as they require less computational power. Therefore, they are capable to deal with large sets of vertices and mesh elements which is convenient as our waveguide problem consists of various length scales at which variations occur (subsection C.4). The success of indirect solvers depends however on the quality of the initial guess and does not provide a guarantee to a solution. We noticed that crucial simulations did not converge or only reached solutions after long computation times.

Direct solvers use discretized physical equations to construct a stiffness matrix which is inverted in a direct way to access the solutions. This type of solvers is fast but requires more computational power and RAM memory. Hence, they are not capable of solving large meshes above 200.000 elements. However, because they certainly provide a solution, we switched to direct solvers, and the PARDISO solver in particular, for the beam bender simulations. This required substantial optimization of meshes, favoring a quadrilateral mesh instead of a tetrahedral mesh (subsection C.4).

The remainder of this appendix considers how the numerical simulations deal with boundary conditions, the infinite extent of the waveguide and meshing optimization. Additionally, we mention a custom-made technique to excite and study diffractive guided modes which are a collection of several eigenfunctions to the Helmholtz equation (chapter 3).

C.2 Infinitely Extended Domains

The slab waveguide (Fig. 3.1) and the waveguide bend (Fig. C.1) are infinitely-extended systems. Therefore, numerical simulation domains should capture the physics of their

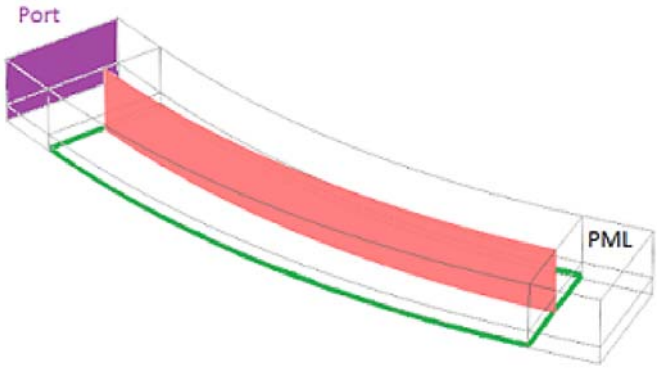

Figure C.1: Simulation domain of a 30-degree beam bend without thickness variation. Along the orthogonal z-direction, there are three distinct layers. The waveguiding layer of thickness $\tilde{a}$ is densely meshed (bottom, in green), an auxiliary vacuum layer of two decay lengths is used for intermediate meshing density (middle) and a top vacuum layer has a coarser mesh (top). An input port excites an eigenmode on an unperturbed waveguide which is bent towards a perfectly matched layer (PML). We obtain our fields and VSWR from data points in the red plane, lying in the center of the beam.

infinite extent despite truncation of the simulation domain. This requires appropriate boundary conditions or 'reflectionless' absorbing layers (PML) which are consistent with the problem at hand.

C.2.1 Boundary Conditions

In this dissertation, boundary conditions are not only useful to truncate the domain but also provide a selection mechanism for the guided modes we are looking for. We will use perfect magnetic conductor (PMC) and the perfect electric conductor (PEC) boundary conditions which are readily derived from extended laws of Faraday and Ampère A.3.2

$$\nabla \times \mathbf{E} = -\mathbf{j}_M - \partial_t \mathbf{B}, \tag{C.1}$$

$$\nabla \times \mathbf{H} = \mathbf{j}_E + \partial_t \mathbf{D}, \tag{C.2}$$

and include a magnetic current $\mathbf{j}_M$. Although scientists are convinced there does not exist a fundamental type of magnetic charge, it is frequently used in computational electromagnetism as they introduce duality into the Maxwell equations which allows modeling magnetic fields in a similar way as electric fields. In the context of metamaterials 2.4.1 such magnetic currents arise as a reinterpretation of antisymmetric electric currents. Fig. C.2 illustrates this for a fishnet structure whose parallel planes have opposite surface current densities.

The PMC and PEC conditions are respectively derived from the boundary condition on an interface between our simulation domain and a perfect magnetical or electric

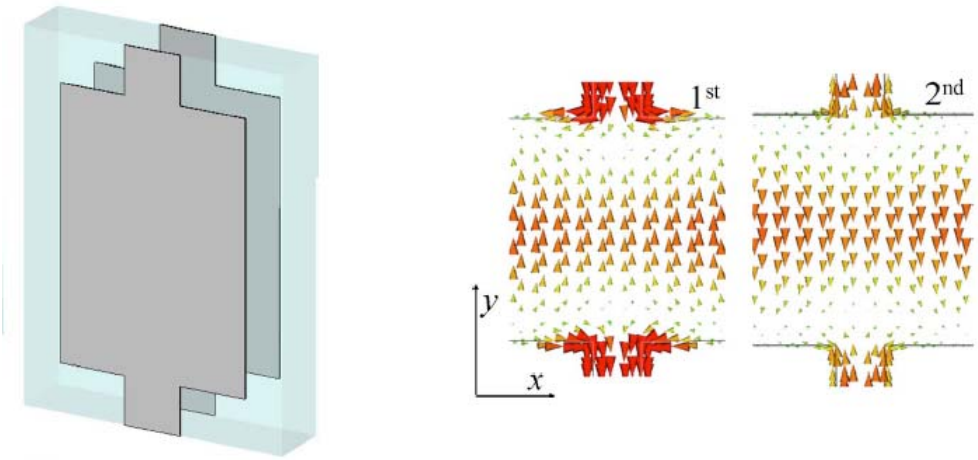

Figure C.2: A Fishnet metamaterial unit (left) consisting of two metallic planes at opposite sides of a dielectric which sustain current densities of opposite sign (right). Picture obtained from Reference [2].

conductor. Then, the tangential components of the left hand sides of (C.1) and (C.2) which contribute to the surface current should vanish. Thus, when the interface has a normal vector **n**, we obtain the following boundary condition

$$\mathbf{n} \times \mathbf{H} = 0 \quad \text{and} \quad \mathbf{n} \times \mathbf{E} = 0.$$

The profile of the TM fundamental mode (4.41) is compatible with those boundary conditions in two ways. From Eq. (2.27) in chapter 2 we learn the magnetic field strength obtains a radial component within the beam bend. Therefore, if we apply a TM condition to the inner and outer radial boundary of the bend, solutions which agree with the fundamental mode profile are favored at the expense of other modes or sustained fields. Equivalently, for a straight waveguide, a PMC condition is applied to the side planes which contain the propagation direction.

Importantly, these boundary conditions also induce reflections as soon as the tangential magnetic field component to the boundary is not zero. When implementing the beam bend without a thickness variation, these reflections are clearly visible (Fig. 5.4). Additionally, the PMC condition allows arbitrary magnetic fields orthogonal to the boundary. This is an effective way to simulate infinitely extended plane waves as the amplitude does not vary orthogonal to the boundary even when looking at fields close to it.

Secondly, the electromagnetic field component along the propagation direction of a fundamental even TM mode is antisymmetric. Since $z = 0$ is the symmetry plane of the waveguide, this implies all electric fields are orthogonal at that plane. Therefore a PEC condition is applied without loss of generality. The boundary condition then guarantees all electric fields are orthogonal to the plane such that the symmetry of the guiding problem allows eliminating the lower half of the slab waveguide. Therefore,

all our simulations and results are expressed with respect to half the thickness of the waveguide $d = 2a$.

Although the in-plane PEC condition is extremely useful to reduce the simulation domain and the number of mesh elements in favor of numerical instability and computing time, the PEC does change the physical problem the simulation solves for. If the complete domain is considered without this boundary condition, odd magnetic modes are also sustained by the guide. When imposing the PEC, this mode is eliminated as its electric field is symmetric with respect to the symmetry plane and is nonzero at the PEC plane. This does not affect the results of this dissertation because we work below the cut-off frequency of the odd mode.

Finally, we also use a PEC condition on the upper boundary $z = L$ of the waveguide. This is not compatible with the evanescent tails of the TM mode which will reflect from the boundary. Still, if L is sufficiently large, i.e. 5 decay lengths, the fields are heavily attenuated below the numerical noise floor of the solver such that they are effectively 'zero' at the upper boundary. Although *Comsol* is equipped with advanced absorbing boundary conditions, e.g. the scattering boundary conditions and perfectly matched layers (PML), these have trouble dealing with purely evanescent tails and cannot be used to remedy the situation.

C.2.2 Perfectly Matched Layers

Ideally, if a truncated simulation domain should pretend to extend to infinity, one might design a boundary layer which absorbs all incoming radiation without inducing reflections. Then, the boundary acts as if the waves have simply propagated through it towards infinity. It is generally very difficult to design such Perfectly Matched Layers (PML's). PML's are defined as boundary layers which achieve perfect reflectionless absorption if their thickness is increased together with the resolution of the mesh. Many implementations claim to be a 'PML' while they are simply good absorbers [3].

Computational problems such as efficient mesh generation and PML design lie at the origin of transformation optics. *Comsol Multiphysics* implements their PML by the following wavelength dependent coordinate transformation

$$t' = \left(\frac{t}{\Delta_W}\right)^n (1 - i)\, \lambda\, F, \tag{C.3}$$

where they define an order n, a scale factor F and a geometric width Δ_W to relate the coordinate of the simulation domain t' to the coordinate of an infinitely stretched medium t. We might interpret the coordinates t as a part of the electromagnetic space which represents the infinite space of the original physical problem.

Eq. (C.3) is sensitively dependent on 'the' wavelength λ of the simulation, is quite sensitive. If we use the effective wavelength instead of the wavelength in vacuum associated to the initial frequency, this leads to reflections. Additionally, in the context

of diffraction (Section 3.4), we noticed the PML has difficulties dealing with oblique incidence of various wavelengths.

Because the PML layer is linked to a transformation-optical interpretation, we slightly modified it to be compatible with the profile of a slab waveguide in our simulation domain. If this waveguide should appear in electromagnetic space with infinite extent, Eq. (2.13) suggests the transformation should contain the refractive index profile $n(z)$ of the waveguide,

$$n(z) = \begin{cases} \sqrt{\tilde{\epsilon}_1} & z > |a|, \\ \sqrt{\tilde{\epsilon}_2} & z < |a|. \end{cases} \tag{C.4}$$

To achieve this, we multiply the scale factor F with the refractive index profile of the guide and verify if the PML absorbs an incident guided mode perfectly (Fig. 3.9).

Because we are interested in minimizing reflections, we briefly consider how the PML is interpreted in terms of the effective transformation-optical material parameters which implement the PML in the simulation domain. According to Equivalence relations (2.13) and (2.14), the transformation should indeed extend the physical coordinates into the complex plane to obtain absorptive complex material parameters [3].

Generally, PML's are designed by the following coordinate transformation

$$\begin{cases} x &= \left(\kappa_x + \frac{i}{\omega}\sigma_x\right)x', \\ y &= \left(\kappa_y + \frac{i}{\omega}\sigma_y\right)y', \\ z &= \left(\kappa_z + \frac{i}{\omega}\sigma_z\right)z', \end{cases} \tag{C.5}$$

where σ_x is the conductivity of the PML and κ attenuates evanescent waves. The conductivity, i.e. absorption of radiative waves, is turned on gradually to avoid reflections. At finite mesh resolution or small thickness Δ_W of the PML layer, reflections still persist and have two contributions. Firstly, the back side of the PML contains a PEC boundary condition which reflects incident waves which are not sufficiently attenuated by the boundary layer. Reflections are observed if they emerge from the PML with sufficient intensity after one round trip. Secondly, electromagnetic waves experience reflections as they cross the interface towards the PML layer. Although transformation-optics achieves impedance-matching which prohibits such transition reflections, as we demonstrated in chapter 2 for the invisibility cloak, the finite mesh resolution discretizes the conductivity profile and distorts impedance-matching in such a way that reflections do occur.

C.3 Mode Excitation

C.3.1 Excitation Ports

Comsol contains a default electromagnetic port which uses and eigenmode calculation to determine propagating solutions of the Maxwell equations if one field, either electric or magnetic, and a propagation vector are specified.

These ports exist in two varieties. The default implementation, which we use in all simulation domains except the extended domain in Fig. D.1, acts as a boundary condition to incoming waves. Incoming waves are only absorbed if their field profiles match that of the excited port. Otherwise, they are reflected.

Recently, *Comsol* released an alternative implementation, a domain-backed assembly port, which may be used inside the simulation domain. Instead of absorbing or reflecting the incident waves, it calculates scattering parameters S_{ij} between itself i and other ports j in the geometry. Therefore, if one port is used inside the simulation domain, as in Fig. D.1, the scattering coefficient S_{11} takes reflections into account from the reminder of the domain. In particular, the S_11 dominantly measures the relfections induced by the waveguide/beam bender interface which is closest to the port.

C.3.2 Generation of non-eigenmodal field excitation

In Section 3.4, we mentioned diffracting guided waves are a (plane-wave) superposition of eigenmodes with distinct propagation vectors. Therefore, the electromagnetic port is not equipped for exciting general confined waves.

When there are no background fields, i.e. $\mathbf{D} = 0$, a conducting sheet with electric current $\mathbf{j}_E$ might produce different magnetic fields across its surface

$$\nabla \times \mathbf{H} = \mathbf{j}_M, \tag{C.6}$$

due to the boundary condition in a non-dielectric medium. Therefore, desired initial magnetic profiles specify the currents which excite them. In particular, we inserted the truncated plane wave (3.69) and the Gauss-Hermite profile (3.70) which led to the results of Chapter 3.

C.4 Meshing Considerations

When dividing a simulation domain into many volume elements, each element should be sufficiently small such that variations in material parameters, in geometrical structures—such as the interfaces of a thin guiding layer—and variations in amplitude or phase

during propagation are negligible over each separate mesh element. To account for variations in phase and amplitude, the Nyquist sampling theorem imposes that any band-limited signal, e.g., a guided mode with upper frequency ω, should be computed or measured in at least $N = \frac{1}{2\omega}$ different sampling points to reconstruct the wave in an unambiguous way. As a rule of thumb, the theorem suggests to take at least two, but preferably five, mesh elements within one wavelength.

We identify four contributions to variations of electromagnetic fields and material parameters in the simulation domain. Three of them are related to the profile of the guided mode (4.41) because it has an in-plane propagation vector β, related to an effective wavelength of about $1.2\mu m$, an oscillating contribution within the guiding layer due to k_2 (3.30) and an extinction coefficient which imposes the decay length $\frac{1}{2k_1}$ in vacuum. The fourth contribution consists of the dimension a of the thin dielectric layer in the guide. This layer is at least two times smaller than all other length scales and dominates mesh resolution constraints.

Our meshing procedure conforms to the separation of in-plane dependence from orthogonal dependence in a slab waveguide (Fig. C.3). Firstly, material interfaces parallel to the symmetry plane $z = 0$ are meshed. In this way we prevent mesh elements from crossing the discontinuity in material parameters such that they indeed remain constant within one mesh element. Secondly, we sweep the in-plane mesh in the orthogonal direction. This second step involves differential meshes to ensure Nyquist's theorem is satisfied. We use 10 elements within the guiding layer of thickness a, 8 elements to sample the initial decay length from the slab-vacuum interface and 30 elements to mesh the orthogonal coordinate of the remaining vacuum. The in-plane mesh is created in such a way that the mesh elements follow the circular propagation of the guided waves. Then, the mesh resolution is in principle determined by the order of magnitude of the effective propagation constant. However, we notice mesh sizes need to exceed those predicted by Nyquist considerably, both in the orthogonal and in-plane direction.

Finally, when performing simulations with inhomogeneous thickness variations between two distinct media, meshing sequences should pay care never to cross such an interface. Therefore, we first meshed the two-dimensional inhomogeneous interface between the guiding and cover layer before sweeping the mesh in the orthogonal direction. Additionally, we defined the medium parameters separately for each cover/guiding layer such that these follow the mesh closely. Though this approach takes all possible measures to avoid different material parameters within one mesh element, the radial magnetic (Fig. D.5) and electric field solutions at an interface (Fig. D.4) still contain suspicious spikes. These may be explained by interpolation errors, which are always present at finite resolution. To be sure, mesh size should be decreased. In practice, this is not possible if one insists on using the direct solver.

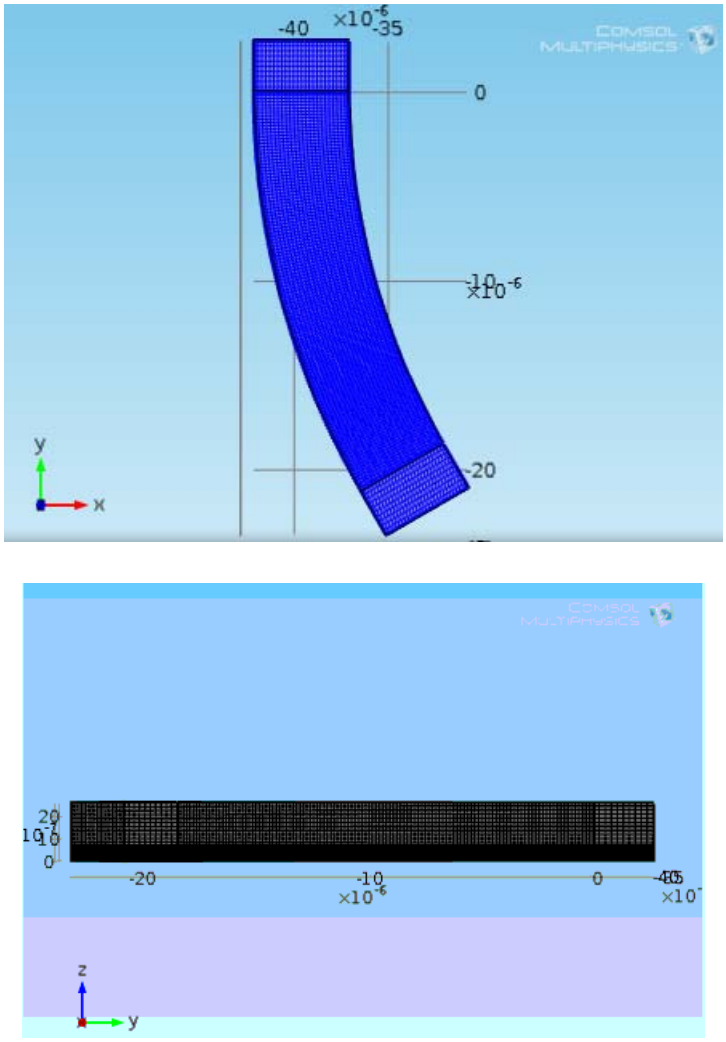

Figure C.3: Two views on a meshed beam bend: A top-view which shows the in-plane mesh consisting of quadrilateral elements following circular arcs (top) and a side-view showing the differential meshing in the orthogonal direction determined by the slab thickness and extinction coefficients (bottom).

References

[1] S. Moaveni, *Finite Element Analysis: Theory and Application with ANSYS*, Pearson Education India, 2003.

[2] M. Kafesaki, I. T. N. Katsarakis, T. Koschny, C. Soukoulis, and E. Economou, "Left-handed metamaterials: The fishnet structure and its variations," *Physical Review B* **75**, 235114–235120, 2007.

[3] A. Oskooi, and S. G. Johnson, "Distinguishing correct from incorrect pml proposals and a corrected unsplit pml for anisotropic, dispersive media," *Journal of Computational Physics* **230**, 2369–2377, 2011.

Appendix D

Supplementary Material

This Appendix contains supplementary material to motivate the claims of chapter 5, which were based on the performance of a 45-degree bend.

D.1

A Thirty-Degree Beam Bend

Instead of the basic simulation domain inFig. 5.1, the 30-degree beam bend consists of an extended simulation domain Fig. D.1 with an additional unperturbed waveguide at the exit and a domain-backed port. The following figures are interpreted in a similar way as the results of the 45-degree bend.

D.1.1 Equivalence Relations

As for the 45 degree bend, Fig. D.2 compares the in-plane radial magnetic fields of the full transformation-optical implementation with our guided transformation-optical implementation. Qualitatively, both field distributions agree better than for a 45 degree bend as expected since the propagation length within the bender is decreased (Table 3.1). Unsurprisingly, Fig. D.3 additionally shows the thickness variation remains a crucial transformation-optical parameter to establish the desired propagation within the plane.

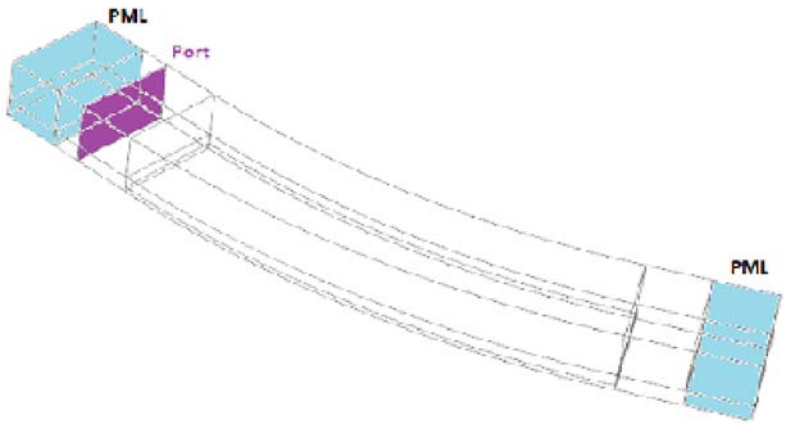

Figure D.1: An extended simulation domain of a 30-degree beam bend without thickness variation to investigate how light couples into and out of the beam bend to an unperturbed waveguide (Table 5.1). A domain-backed input port now excites modes in one direction and allows determining the scattering coefficients because of the waveguide/beam bender interface.

D.1.2 Variations in Guiding Layer Thickness

To estimate how the beam bender performance depends on the initial thickness $\tilde{a}$ of the slab, we performed several simulations for $\tilde{a} = 0.21\mu m$, $\tilde{a} = 0.20\mu m$, $\tilde{a} = 0.17\mu m$ and $\tilde{a} = 0.15\mu m$.

In this section, we use four additional figures to illustrate the in-plane and orthogonal dependence of the radial magnetic and electric field strengths in the guided transformation-optical beam bender. Fig. D.4 and Fig. D.5 show the electric and magnetic fields at $0.1\mu m$ height with respect to the symmetry plane of the slab for several initial thicknesses of the waveguide. Because the radial magnetic field strength does not diminish with propagation distance, we prove the guided wave is efficiently turned over 30 degrees. Still, there might be some reflections or other contributions which convert the initial TM mode to a TE mode. The observed radial electric field strengths are small, approximately 1% of the total electric field norm, which implies the beam bender turns the guided mode in an efficient way.

The final two figures verify the orthogonal dependence with respect to the waveguide. As explained in the main text, the peaks at the interface between the cover and the guiding layer are probably caused by numerical errors due to finite mesh resolution. The electric field oscillations are low, i.e. comparable to those of the full transformation-optical implementation. These might point to radiative modes which are reflected by the upper PEC boundary.

D.1.3 Estimations of Reflections

The VSWR of a 30-degree bend yield the same qualitative results as the 45-bend discussed in the main text. Table 5.3 estimates the additional reflections due to the beam bend to 4% which is comparable to reflections induced by glass with orthogonally incident light.

D.2 A Concentrator

Next to the beam bender, the guided concentrator Fig. D.9 was another application pursued by this master dissertation. It came as a surprise that the concentrator is also implemented by the exponential map (4.64). In literature, finite-embedment transformation-optical devices mostly consist of a three-dimensional transformation-optical device which is surrounded by vacuum (subsection 2.2.2). The trajectories within the device are thought to be continuous extensions of the straight trajectories in the surrounding vacuum. Our concentrator demonstrates it is possible to connect to any set of geodesics in physical space as long as the boundary of the transformation-optical medium is chosen in a considered way. In this particular case, one might couple to circular trajectories or to radial trajectories as shown in (Fig. 2.4).

The realization of a guided transformation-optical concentrator was delayed by two numerical difficulties. Firstly, diffraction counters the concentrating effect of the device. When the propagation length within the concentrator is increased—to ensure gradual thickness variations and slowly concentrating beams—diffraction effects dominate and the gaussian beams do not concentrate. Secondly, if one decreases the propagation length within the device, mesh resolutions have to increase to resolve fine thickness variations. It is then necessary to use an indirect, iterative solver. However, for an indirect solver we did not reach convergence as we expect the initial guess deviates strongly from the desired solution.

The concentrator simulations did contribute to determining the phase velocity matching 4.58 with three key simulational results Fig. D.9. To achieve homogeneous materials in the bounding PML layers of the simulation domain, the thickness variation and the permittivity profile were only applied to a wedge-shaped region in the center of the domain. This shape was terminated by steep edges, using a step-function. This arbitrary wedge shape is clearly visible in Fig. D.10 when phase velocity matching is satisfied. The first observation of phase velocity matching in a guided transformation-optical device, was established by a map of the gaussian field profiles between a full transformation-optical simulation and another simulation with thickness variation (5.2).

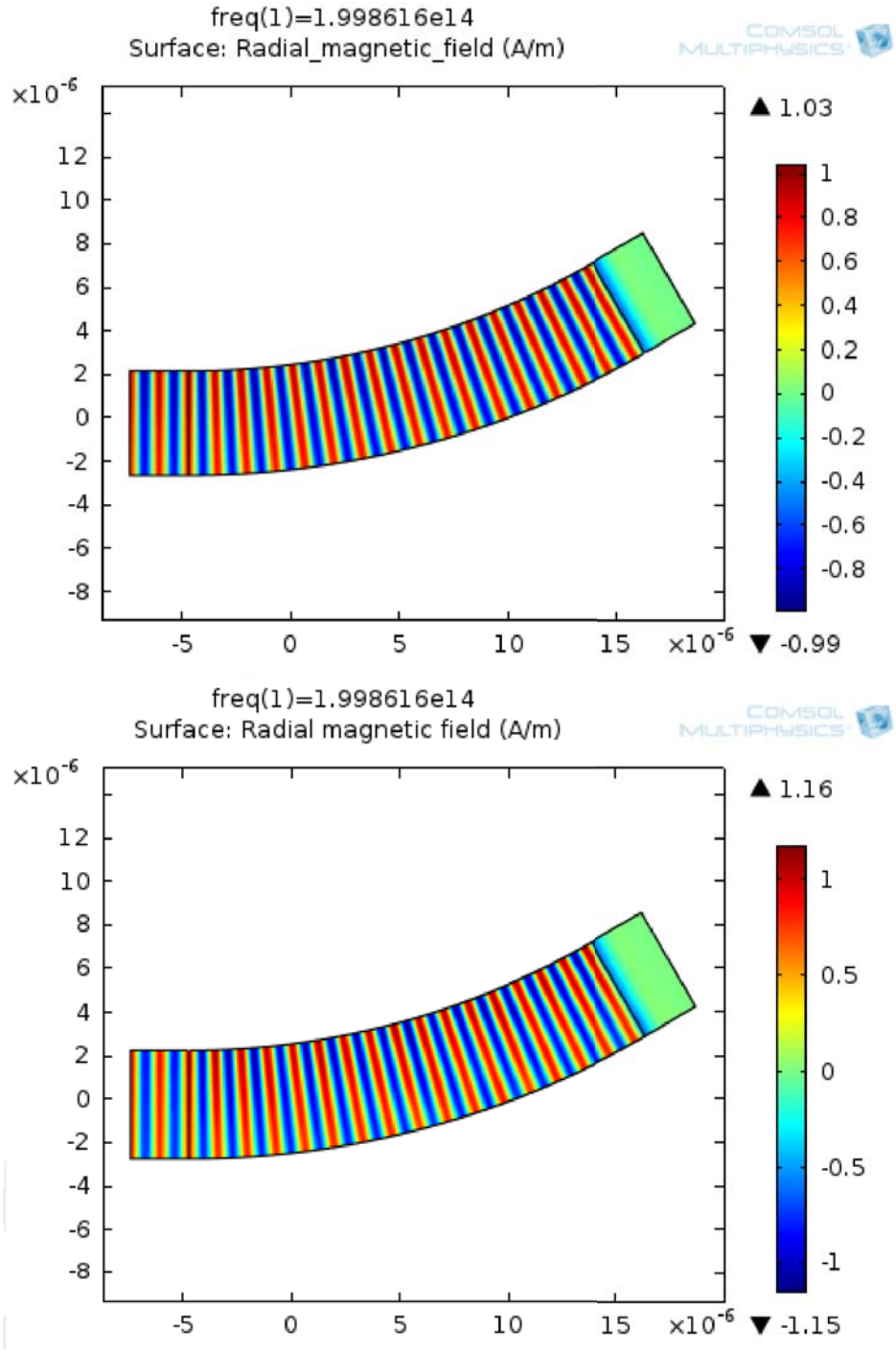

Figure D.2: Verification of the thickness equivalence relation for a 30-degree beam bend. The in-plane propagation of an excited fundamental TM mode is compared for a full transformation-optical implementation (up) and a guided transformation-optical implementation with thickness variations in the guiding layer (low).

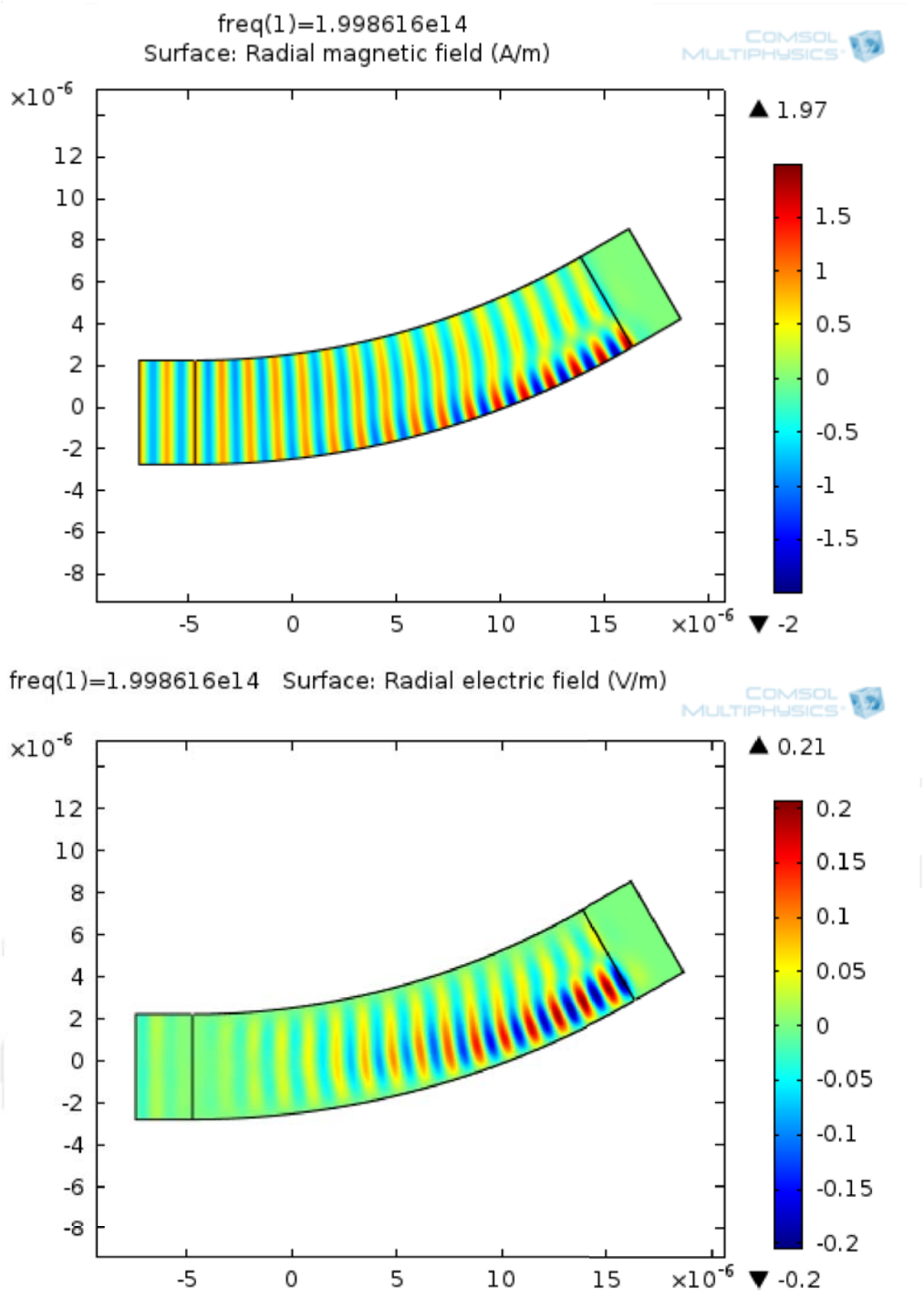

Figure D.3: Radial magnetic fields (up) and radial electric fields (down) in the plane of the guiding layer with an inhomogeneous permittivity (5.1) but without a thickness variation.

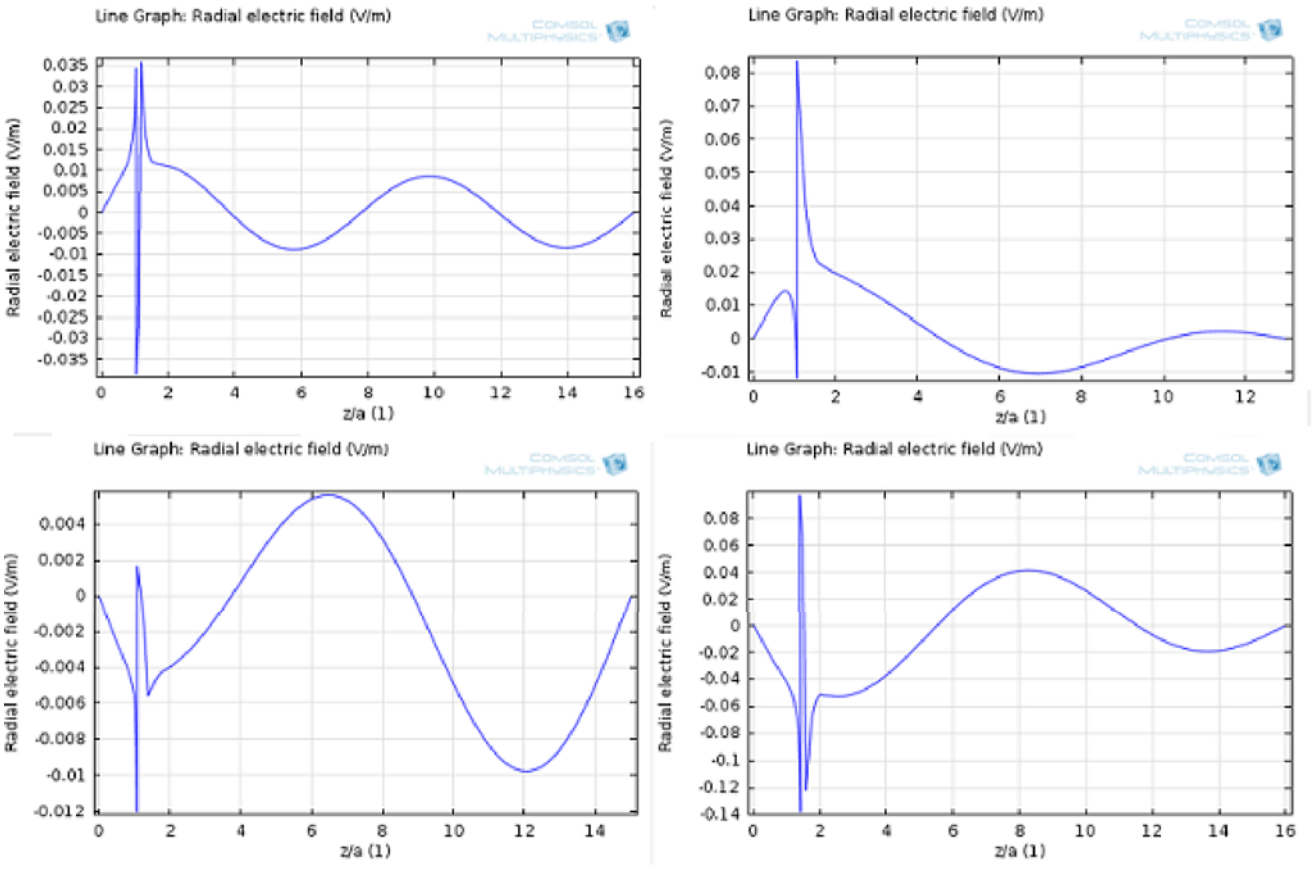

Figure D.4: Radial electric fields along the normal vector of waveguide relative to the maximal electric norm in the propagation plane of the guided transformation-optical beam bender for different thicknesses a: $0.21\mu m$ (upper left), $0.2\mu m$ (upper right), $0.17\mu m$ (lower left), $0.15\mu m$ (lower right)

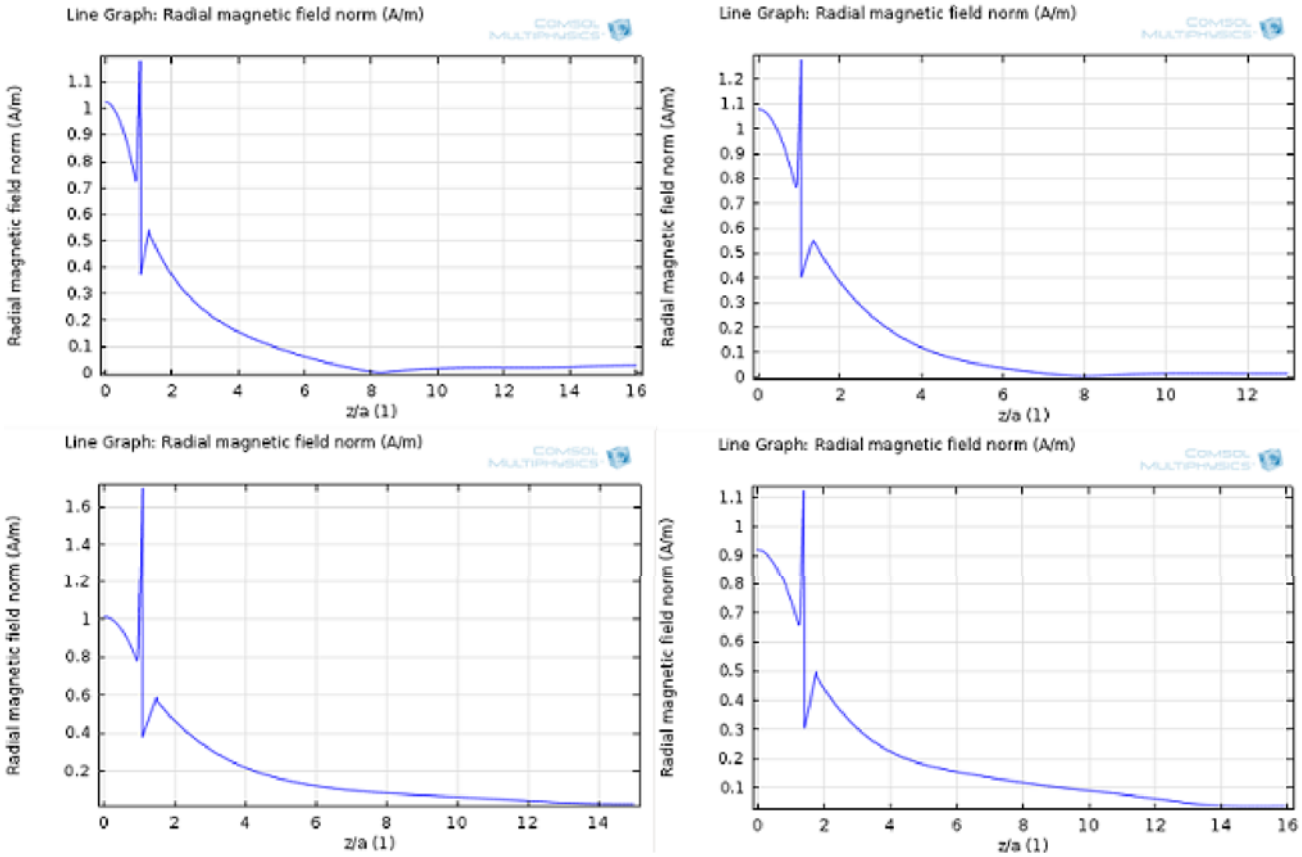

Figure D.5: Radial magnetic strengths along the normal vector of the waveguide relative to the maximal magnetic strength norm in the propagation plane of the guided transformation-optical beam bender for different thicknesses a: $0.21\mu m$ (upper left), $0.2\mu m$ (upper right), $0.17\mu m$ (lower left), $0.15\mu m$ (lower right)

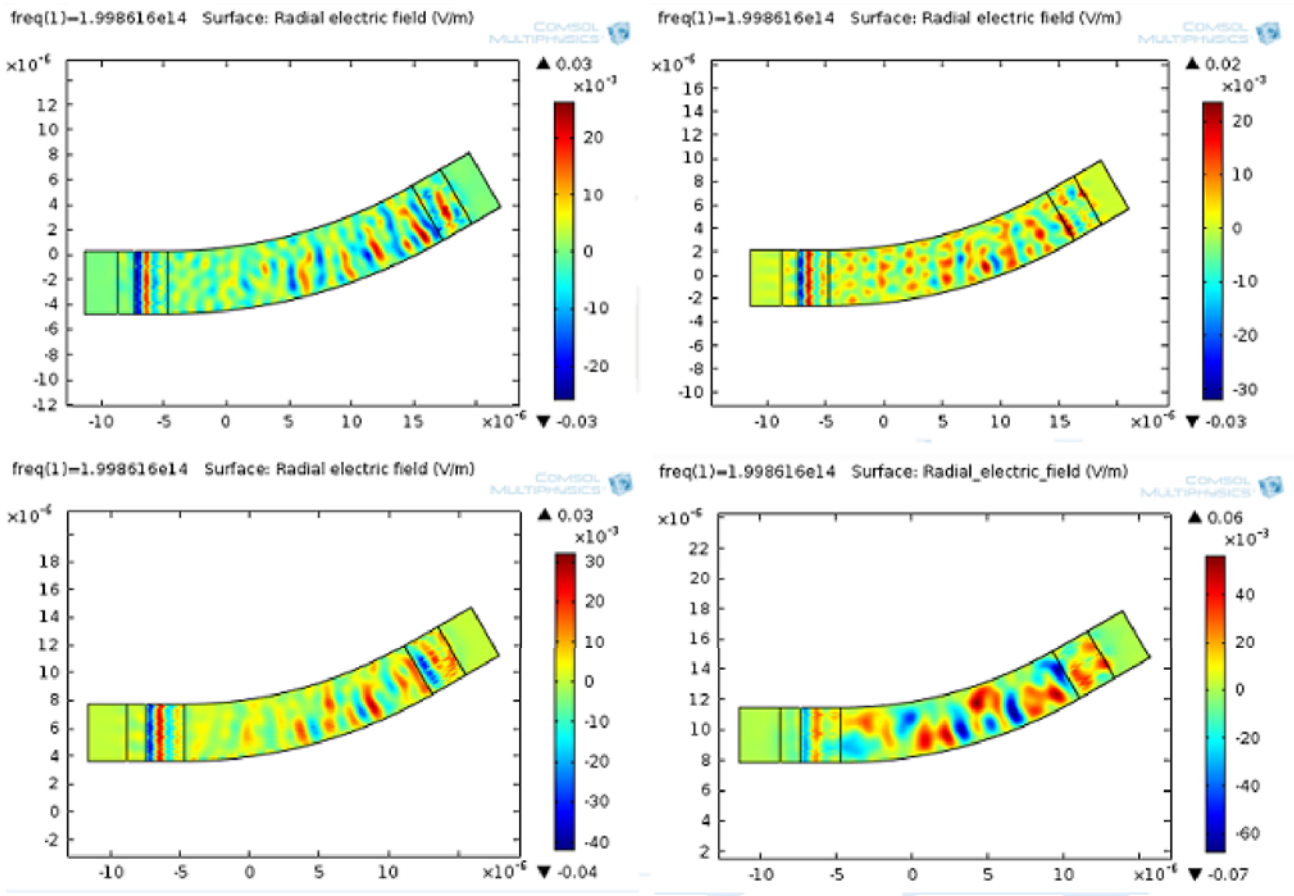

Figure D.6: In-plane radial electric fields relative to the maximal electric field norm of guided transformation-optical beam benders for different thicknesses a: $0.21\mu m$ (upper left), $0.2\mu m$ (upper right), $0.17\mu m$ (lower left), $0.15\mu m$ (lower right)

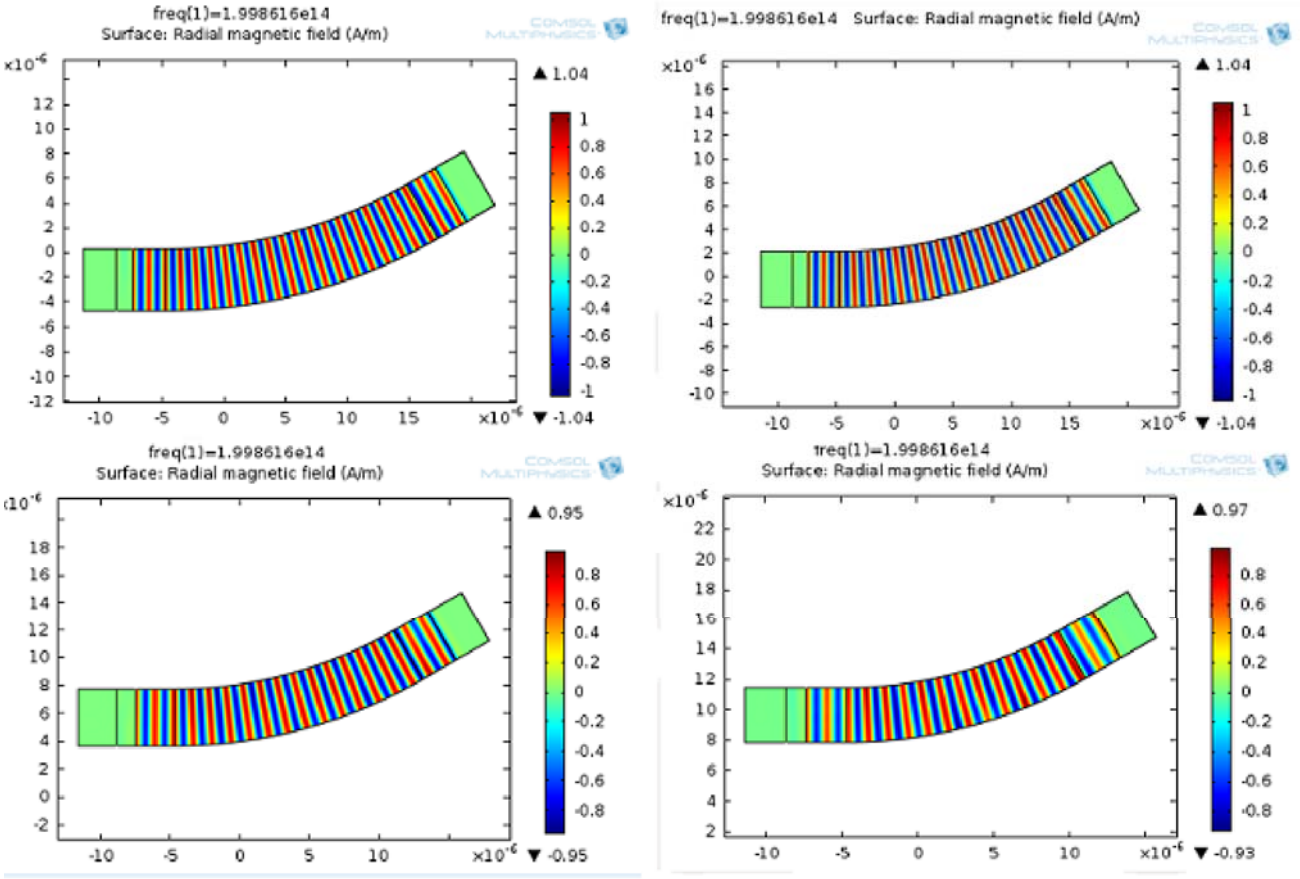

Figure D.7: In-plane radial magnetic field strengths relative to the maximal magnetic field strength norm of guided transformation-optical beam benders for different thicknesses a: $0.21\mu m$ (upper left), $0.2\mu m$ (upper right), $0.17\mu m$ (lower left), $0.15\mu m$ (lower right)

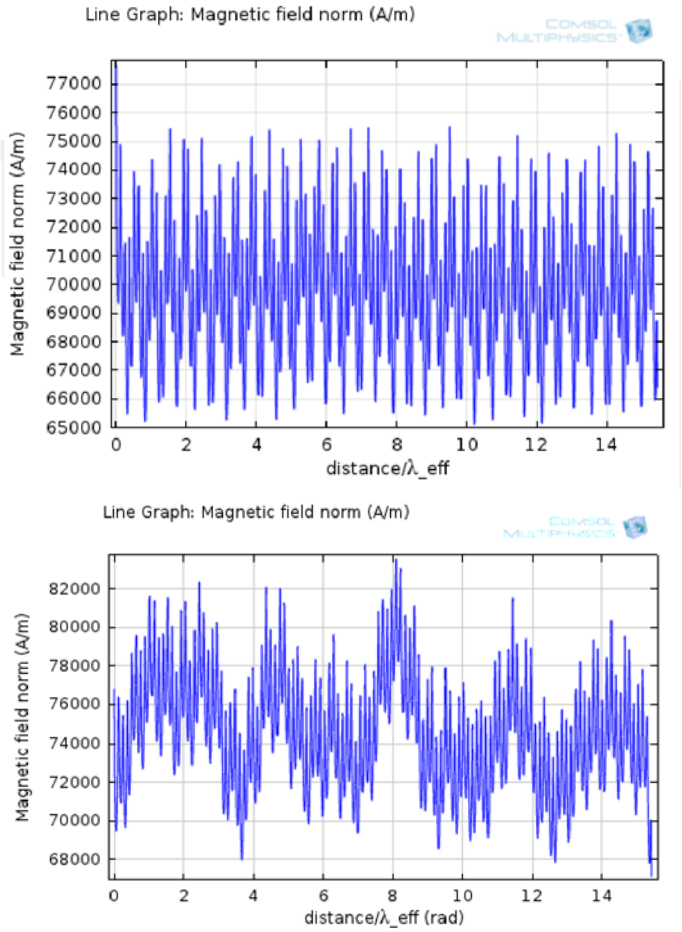

Figure D.8: VSWR data for a 30-degree beam bend for a full transformation-optical implementation (up) and a guided transformation-optical implementation (down).

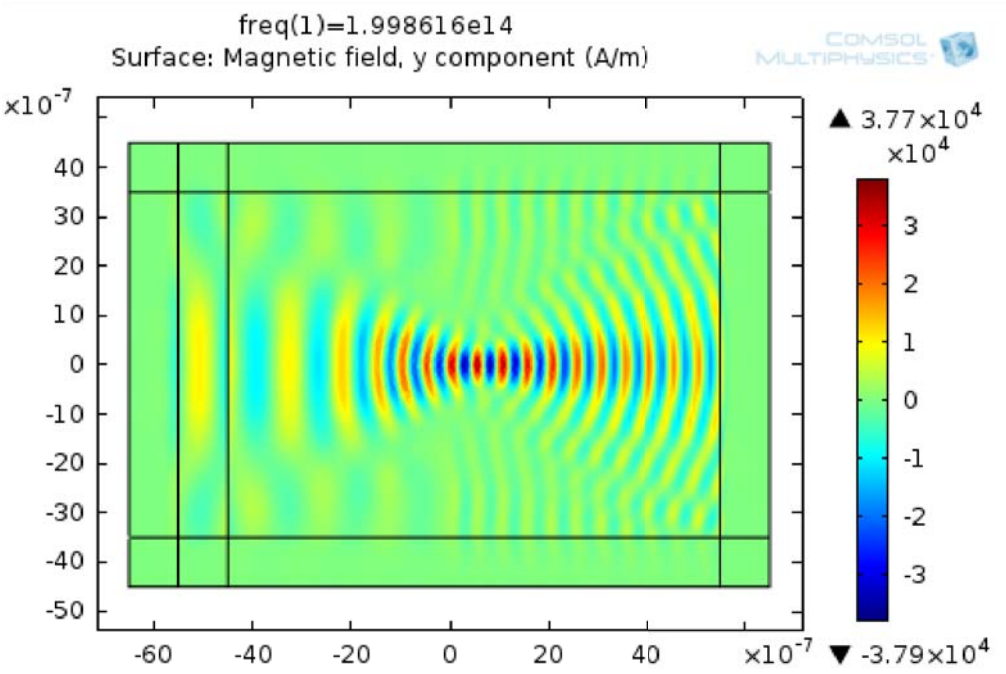

Figure D.9: Finite-difference simulation in the frequency domain of a full transformation-optical conformal concentrator acting on a diffractive gaussian beam with $3\mu m$ beam waist.

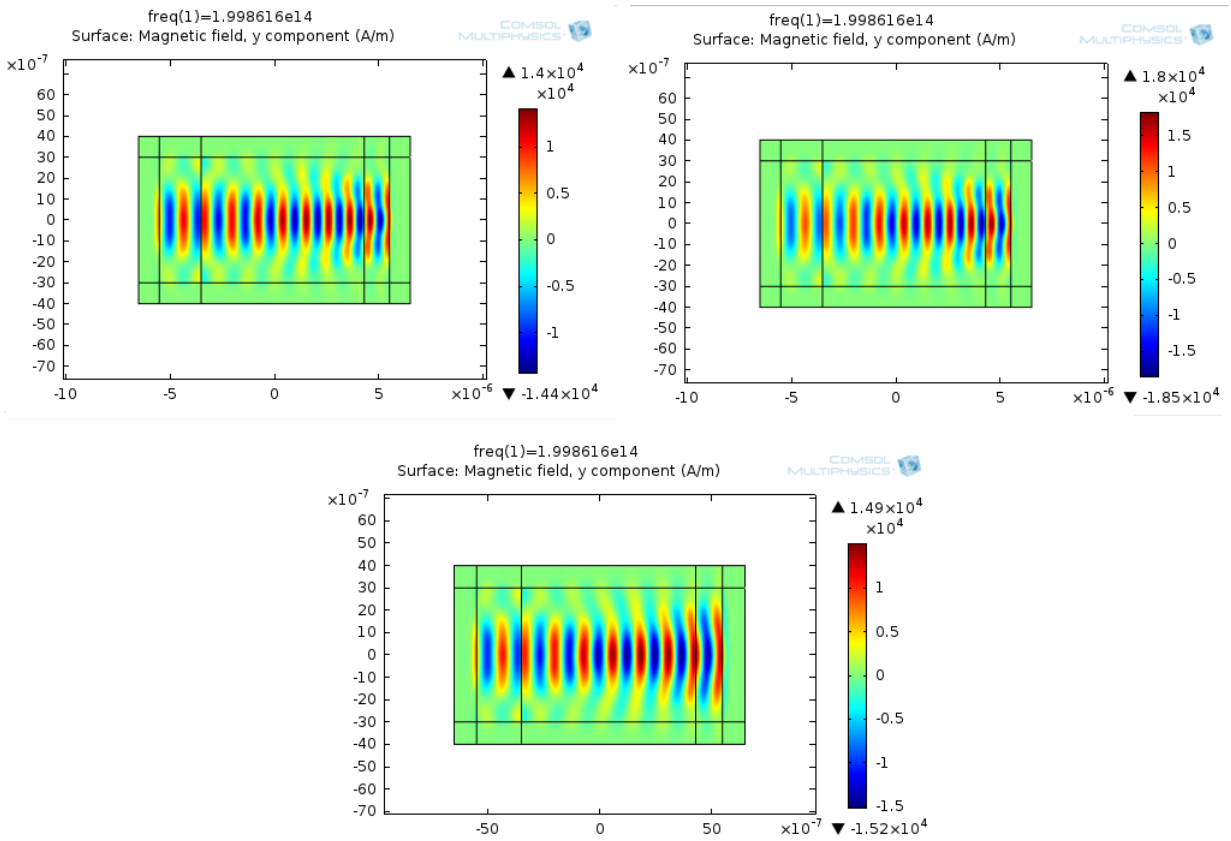

Figure D.10: Comparison of three simulations based upon the design of a conformal concentrator. The guiding layer has a particular thickness profile which is resolved by a full transformation-optical implementation (upper left) and a partial implementation with thickness variation (4.69) (upper right). If no thickness variation is imposed, the gaussian beam propagates unaffected (lower).